Static and dynamic properties of confined magnetic nanostructures

Dissertation
zur Erlangung des Doktorgrades
des Department Physik
der Universität Hamburg

vorgelegt von
Ole Albrecht
aus
Aurich

Hamburg
2010

Gutachter der Dissertation: Prof. Dr. K. Nielsch
Prof. Dr. D. Heitmann

Gutachter der Disputation: Prof. Dr. K. Nielsch
Priv. Doz. Dr. G. Meier

Datum der Disputation: 26.3.2010

Vorsitzender des Prüfungsausschusses: Dr. K. Petermann

Vorsitzender des Promotionsausschusses: Prof. Dr. J. Bartels

Dekan der MIN-Fakultät: Prof. Dr. H. Graener

Abstract

This dissertation deals with experimental investigations of magnetic micro- and nanostructures taken as model systems for data storage or biomedical applications. The reduced dimensionality in this kind of structures has a major influence on the magnetic properties and gives rise to novel effects unknown in bulk material. These effects, such as magnetization reversal modes and superparamagnetism and how shape and size affect them, are investigated by SQUID and MOKE magnetometry. Nanomagnets of various shapes and sizes are presented, each of which require the use of a specific preparative approach.

First of all, bimetallic (NiPt) nanoparticles of spherical and cubic shapes ($r \approx 3$ nm) are investigated, synthesized by a wet organometallic route. These particles reveal an appearance of superparamagnetism. This behavior is typical for magnetic particles in this range of size. We find a relationship between a characteristic temperature dependence of the magnetization and the Ni content of the particles. Further measurements allow for the determination of a general anisotropy constant for each sample.

In a second approach, we investigate the magnetic properties of patterned thin magnetic films deposited by thermal evaporation on prepatterned templates. These have been realized by using e-beam lithography and a glancing angle deposition technique. The different reversal modes and the influence of the geometric shape on the magnetic properties are the focal point of this section.

In the third approach, magnetic nanotubes are produced by a combination of the glancing angle (GLAD) and atomic layer (ALD) deposition techniques. The first technique allows for the growth of Si columns on a substrate. This template is subsequently covered with magnetic material by atomic layer deposition. The angular dependent magnetic measurements reveal a transition between different reversal modes which has been theoretically predicted for magnetic nanotubes.

Zusammenfassung

In dieser Arbeit werden die magnetischen Eigenschaften von Mikro- und Nanostrukturen untersucht, welche als Modellsystem für Anwendungen in Speichermedien und medizinischen Anwendungen benutzt werden können. Die reduzierten Dimensionen der Nanostrukturen beeinflussen maßgeblich die magnetischen Eigenschaften und sind so verantwortlich für neue magnetischen Effekte, die in Vollmaterialien nicht bekannt sind. Diese magnetischen Eigenschaften werden mit Hilfe der SQUID- (Superconducting Quantum Interference Device) und der MOKE- (Magneto Optical Kerr Effect) Magnetometrie untersucht.

Verschiedene Ansätze für die Herstellung derartiger Strukturen werden vorgestellt. Als erstes werden bimetallische (NiPt) Nanopartikel mit einer Kugel- oder Würfelform präsentiert, die in einem nass-chemischen Syntheseverfahren hergestellt wurden. Diese Partikel zeigen in temperaturabhängigen Messungen ein superparamagnetisches Verhalten, welches durch ein charakterischtisches Maximum identifiziert wird. Dieses Verhalten ist bezeichnend für magnetische Partikel in der Größenordnung von einigen Nanometern. Weitere Messungen erlauben die Bestimmung einer generalisierten Anisotropiekonstanten der jeweiligen Proben.

Die magnetischen Eigenschaften von strukturierten dünnen magnetischen Filmen werden als zweites untersucht. Diese enstehen durch thermischen Verdampfen von magnetischem Material auf vorstrukturierten Templaten. Sie werden mittels Elektronenstrahl-Lithographie oder durch die Methode der Glancing Angle Deposition hergestellt. Die verschieden Moden der Magnetisierungsumkehr in ferromagnetischen Ringstrukturen und der Einfluss der Probengeometrie werden an diesen Strukturen untersucht.

Als drittes werden magnetische Nanoröhrchen untersucht, welche mittels einer Kombination der Glancing Angle (GLAD) und Atomlagen (ALD) Deposition hergestellt werden. Die GLAD-Technik erlaubt die Abscheidung von Zylindern aus Silizium auf einem Substrat. Die ALD-Technik ermöglicht die atomlagengenaue Abscheidung von magnetischem Material auf den Silizium-Zylindern, um so magnetische Röhrchen herzustellen. Durch winkelabhängige Messungen wird ein Übergang zwischen verschiedenen Moden der Magnetisierungsumkehr bewiesen, welcher theoretisch vorhergesagt worden ist.

Contents

1 Introduction **1**

2 Theoretical principles **5**
- 2.1 Energy contributions in magnetic materials 5
- 2.2 Development of domains 7
- 2.3 Magnetism in confined structures 8
- 2.4 Single-domain particles 15
- 2.5 Temperature effects in confined structures 17

3 Experimental setup **19**
- 3.1 SQUID magnetometer 19
- 3.2 DC magnetometry 22
- 3.3 AC magnetometry 26
- 3.4 MOKE magnetometer 29

4 Magnetic nanoparticles **31**
- 4.1 $\mathrm{Ni_xPt_{1-x}}$ nanoparticles 31
- 4.2 NiPt/CdSe nanoparticles 43

5 Magnetic properties of patterned thin films **49**
- 5.1 Submicron ferromagnetic rings 49
- 5.2 Arranged magnetic dots 61

6 Magnetic nanotubes **69**
- 6.1 Preparation 70
- 6.2 Magnetic measurements 75
- 6.3 Models of magnetization reversal in nanotubes 82
- 6.4 Transverse to vortex reversal transition 84

7 Summary **89**

A $\mathrm{Ni_xPt_{1-x}}$ **105**

B Simulation OOMMF **109**

C Magnetic nanotubes **113**

D Process parameters **115**

E Publications **117**

Chapter 1

Introduction

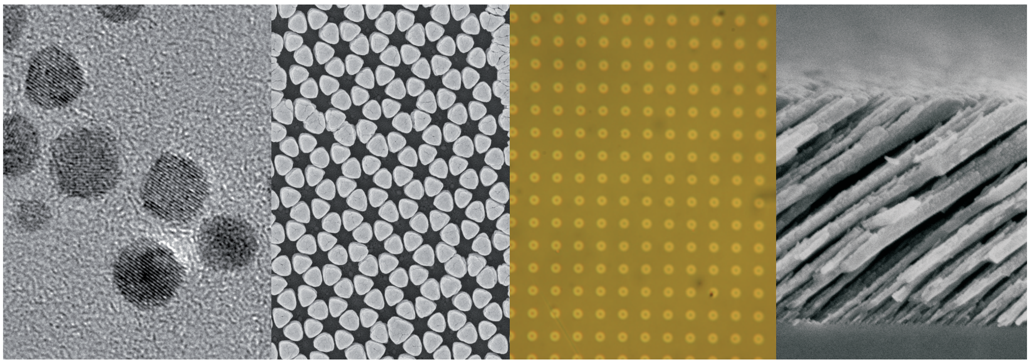

Magnetic solids have been in focus of research for several decades due to a wide range of applications in technological devices. New effects arise by a confinement in one ore more directions in space. Unlike in the case of bulk materials, the properties of these nano-sized solids are mainly determined by the shape and the size. The geometric confinement leads to an altered ratio between the volume and the surface, which introduces new anisotropic components and thereby results in dramatically affected magnetic properties. These are demonstrated by the magnetic configurations at the saturated state, during a magnetization reversal and new characteristic temperature dependencies. Nanomagnets can be classified in three different size classes: 0D for objects $<$ 10 nm, 1D $<$ 100 nm and 2D $<$ 1000 nm. Each class, synthesized in a specific way, exhibits characteristic magnetic properties due to the different types of confinement.

In the first class, we investigate bimetallic magnetic nanoparticles. The synthesis of these kind of particles was described the fist time by Sun et al. [1]. The iron-platinum (FePt) particles, embedded in an organic matrix, are produced by a wet organometallic synthesis route. Besides this material system, cobalt was used to synthesize CoPt particles in the same way, which is well described in literature [2, 3]. Only few publications [4, 5] are dealing with particles made out of the third magnetic transition metal nickel. The aim of this work is to close this gap and investigate the static and dynamic magnetic properties of these particles. The influence of the composition, size and the shape of the particles on the magnetic properties are in focus.

A second approach described in this work is the structuring of ferromagnetic thin films. It evokes new magnetic phenomena related to an increase of the coercive field. Two possible ways are investigated, namely the creation of submicron rings and arrays of nano dots.

The ferromagnetic rings are produced by a deposition of a magnetic material onto a surface which is prestructured by e-beam lithography. The focus of research described in literature on such structures has been set primarily upon the dynamic properties determined by FMR (ferromagnetic resonance) experiments so far. The static properties were mainly investigated by using methods such as MOKE magnetometry (magneto optical Kerr effect) and by simulations. Novel domain configurations appear in these structures, which are an onion state characterized by a head-to-head or tail-to-tail configuration, the stray-field free vortex state or a combination of both, respectively. A detailed investigation on the static magnetization properties and the involved domain configurations is one focus of this work.

The second type of a patterned magnetic films is achieved by the deposition of magnetic material on prestructured templates. This patterning is achieved by the use of glancing angle deposition. The GLAD technique is a physical vapour deposition, which is based on self-shadowing effects.

An increase of the thickness of a ferromagnetic ring leads to a new structure, a tubular one. It can be apprehended as a rolled-up thin film. The magnetic properties, especially the magnetization reversal modes, are dominated by the tubular shape and the thickness of the magnetic layer. The magnetic properties of nanotubes produced in porous alumina templates and their magnetic properties have been well described in literature for two prominent configurations, namely an applied field parallel and perpendicular to the long axis of the tube. This work deals with a different synthesis route to yield such structures and present detailed results of the magnetization in the two configurations of an applied field parallel or perpendicular to the tube axis.

For the investigation of the dynamic and static magnetic properties of the samples, a SQUID magnetometer (superconducting quantum interference device) is used. In particular, a MOKE magnetometer (magneto optical Kerr effect) is used for the research on the prestructured thin films.

Chapter 2

Theoretical principles

The aim of this chapter is to give an overview on the influence of the size confinement of magnetic materials on their magnetic properties. For a detailed introduction to ferromagnetism the reader is referred to the following textbooks [6, 7, 8, 9].

2.1 Energy contributions in magnetic materials

Several energy terms contribute to the magnetic properties of ferromagnetic materials. The main contributions to the total energy are the following energy terms: exchange, Zeeman, magnetostatic and the anisotropy energy:

$$E_{\text{tot}} = E_{\text{exchange}} + E_{\text{Zeeman}} + E_{\text{magnetostatic}} + E_{\text{anisotropy}} + \cdots \ . \tag{2.1}$$

Exchange energy

The ferromagnetic ordering in solids can be described by the Heisenberg model. Each spin $\vec{S}$ results in a magnetic moment $\vec{\mu} = -g\mu_{\text{B}}\vec{S}$, with the g-factor and μ_{B} the Bohr magneton.

The energy of a spin system can be expressed by:

$$E = -2\sum_{i \neq j} J_{ij}\vec{S}_{\text{i}} \cdot \vec{S}_{\text{j}} \ . \tag{2.2}$$

If the spins i and j are parallel to each other, the scalar product is positive and has its highest value. With a positive exchange constant J (for ferromagnetic samples) this state has an energy minimum and it is the preferred configuration. This model is isotropic and depends only on the distance between i and j. The exchange energy is short-ranged and promotes a parallel configuration of the spins. The observed anisotropic magnetic behavior can only be explained by additional anisotropic energy terms, which are described below.

Magnetostatic energy

Each single magnetic moment has a stray field and this leads to a demagnetization field $\vec{H}_\mathrm{d}$, which is opposed to the magnetization and therefore causes a magnetostatic energy. This dipolar interaction decreases with distance as r^{-3}, thus it remains significant on a long-range unlike the exchange energy

$$E_\mathrm{magnetostatic} = -\frac{1}{2}\int_{samp.} \vec{H}_\mathrm{d} \cdot \vec{M} dV \ . \tag{2.3}$$

Zeeman energy

This energy term is defined by the interaction of a magnetized sample with an applied external magnetic field. If this is a uniform field, only the average magnetization of the sample is taken into account

$$E_\mathrm{Zeeman} = -\mu_0 \int \vec{H}_\mathrm{ext.} \cdot \vec{M} dV \ . \tag{2.4}$$

Anisotropy energy

In bulk materials, the anisotropy energy is dominated by the magnetocrystalline energy, which is needed to change the direction of the magnetization without a movement of the particles or of the relative orientations of the spins. The crystal structure is the reason for the appearance of preferred orientations of the magnetization, which are labeled as the easy axes. In these directions the saturation magnetization is obtained at low externally applied fields compared to the hard axes, for which higher fields are needed. The energy difference between both directions is defined as anisotropy energy.

The origin of this anisotropy contribution is the spin-orbit coupling. This coupling changes the shape of the atomic orbital, it is no longer spherical.

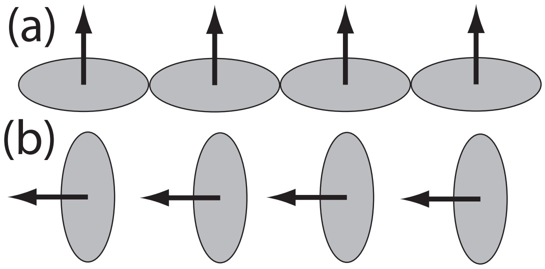

Figure 2.1: Formation of the magnetocrystalline anisotropy due the spin-orbit coupling (Fig. similar to [9]), (a) describes the case of an easy axis and (b) of a hard axis.

As shown in Fig. 2.1 both states are characterized by the amount of overlap of the atomic orbitals. The easy axis has a larger overlap.

This bulk anisotropy contribution can be covered by an additionally non-intrinsic anisotropy, which is caused by a changed ratio between the volume and surface modification, as in thin magnetic films. The surface spins of the magnetic layer have no neighboring spins at one side of the interface. This restriction provoke a change of the exchange constant, compared to the value obtained for bulk materials. The preferred spin configuration dependents on the involved magnetic materials and their properties. This anisotropy term and the influence of the shape is described below in Sec. 2.3.

2.2 Development of domains

The minimization of the total energy may lead to the formation of domains in magnetic materials. Magnetic domains are small regions in ferromagnetic materials, characterized by a parallel alignment of the containing magnetic moments. They are mainly caused by the magnetostatic energy. A single domain ferromagnet with macroscopic dimension causes a demagnetization field $\vec{H}_{\mathrm{d}}$ (see Fig. 2.2). This field can be reduced by a development of a multi-domain configuration including closure domains. But the appearance of domains increases the exchange and anisotropy energies. So the domain configuration of a ferromagnetic material is determined by the minimization of all energy contributions.

The term ”domain wall” describes the barrier between two neighboring domains. In bulk materials it mainly appears as a Bloch wall (Fig. 2.3), in

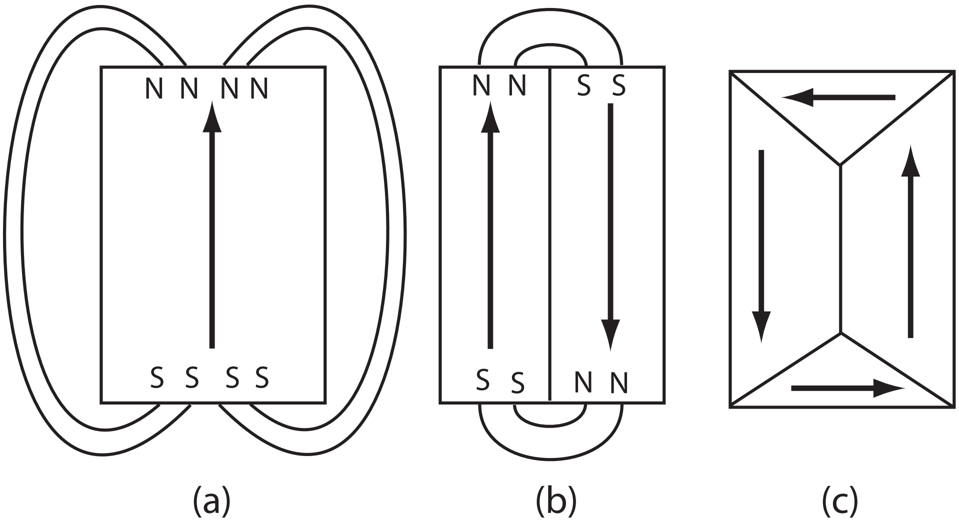

Figure 2.2: Energy minimization evokes the domain configuration of the magnetic sample. A single magnetic moment (a) is responsible for an increased magnetostatic energy. This energy is reduced be a multidomain configuration (b). A stray field free state is reached by the introduction of closure domains (c).

which the magnetization rotates about an angle of 180° perpendicular to the connection axis between the domains.

In thin magnetic films, the transition between domain walls occurs via a Néel wall (Fig. 2.4). The magnetic moments rotate in the plane of the thin film. A detailed introduction to the appearance of magnetic domains is given in [10]. For confined structures presented in the following chapters new and for each type of confinement typical domain wall types appear.

2.3 Magnetism in confined structures

Due to a confinement of the magnetic material in the range of nanometers new contributions to the total energy of a magnetic sample arise and lead to new magnetic properties. The most simple confinement type is a thin magnetic film. In the case of Permalloy ($Ni_{80}Fe_{20}$), a material with a low

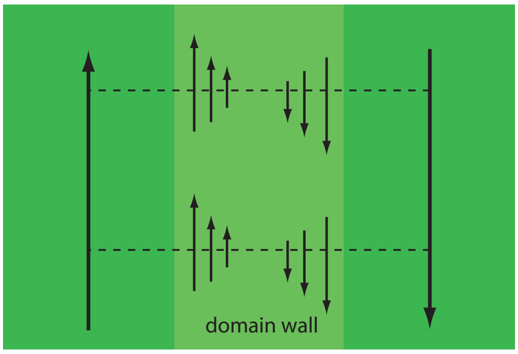

Figure 2.3: The Bloch wall is the favored type of transition between domains in bulk materials. The magnetization changes between domains by a rotation of the spins (inside a domain wall) perpendicular to the connection axis (dashed lines).

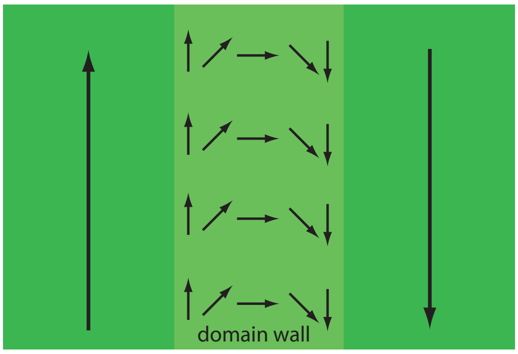

Figure 2.4: The Néel wall is the favored type of transition between domains in thin films. The magnetization changes by a rotation of the spins in the plane of the film.

magnetocrystalline anisotropy (270 J/m^3 [11]), this lateral confinement leads to an easy axis parallel to the plane of the magnetic film. The hard axis is perpendicular to the film plane. In this and the following described structures the magnetic properties are mainly dominated by shape and size.

2.3.1 Lateral structures

By additional structuring of the film more complex structures can be fabricated. These kind of structures are described in the following subsections.

Dots/Antidots

Dot-like magnetic structures exhibit new magnetic effects displayed by new domain configurations. They are strongly affected by the lateral size and thickness of the magnetic layer. After saturation in a high field, two possible reversal modes have been reported in literature in this kind of structures [12]. For thicker layers and larger lateral sizes the vortex mode, with vanishing external flux, is favorable whereas for small and thin ones, a single-domain configuration, in which no domain wall appears, is preferred. The cylindrical symmetry of these structures inhibits an additional configuration anisotropy, unlike in rectangular structures. If the distance of a single structure to others in an array is equivalent or larger than the size, then the properties of the elements are mostly not affected by the neighboring structures [13].

The inverted structures to this, namely antidots, exhibit different magnetic properties. These structures are characterized by the magnetic lattice between the non-magnetic dots which introduce an additional anisotropy term, the configuration anisotropy. The main focus in literature is on square and hexagonal lattice configurations [14, 15, 16, 17]. Measurements on these kind of structures clearly reveal the influence of the geometrical arrangement on the magnetic properties. Beside the measurements using MOKE [18], MFM or other techniques [19] the static properties are often characterized by micromagnetic calculations [20] to investigate the involved domain structures.

Submicron rings

In ferromagnetic submicron rings novel domain configurations appear and determine the magnetization reversal between both saturated states. A detailed description of these phenomena can be found [21, 22, 23, 24, 25, 26, 27]. The reversal is mainly influenced by the width of a single ring, the film thickness and by the lack of a magnetic core, in contrast to magnetic dots.

As displayed in Fig. 2.5, different domain configurations can appear during a magnetization isotherm loop. (b) and (e) are labeled as (reverse) onion states. These states, with a head-to-head domain configuration, are reached after a saturation in a sufficiently high magnetic field and a subsequent reduction of the applied field. After a further reduction of the magnetic field, the vortex state (c) is reached. It features a head-to-tail domain configuration without an external flux. In wide rings a third state appears, the vortex core (d), characterized by a small vortex core inside one side of the ring. This state is not favorable in narrow rings. The promoted domain configuration at each field strength depends on the minimization of the total energy. The exchange energy favors a uniform magnetization and the magnetostatic energy a flux-closure vortex state. This energy minimization is also responsible for the promoted head-to-head domain wall in the onion state [28].

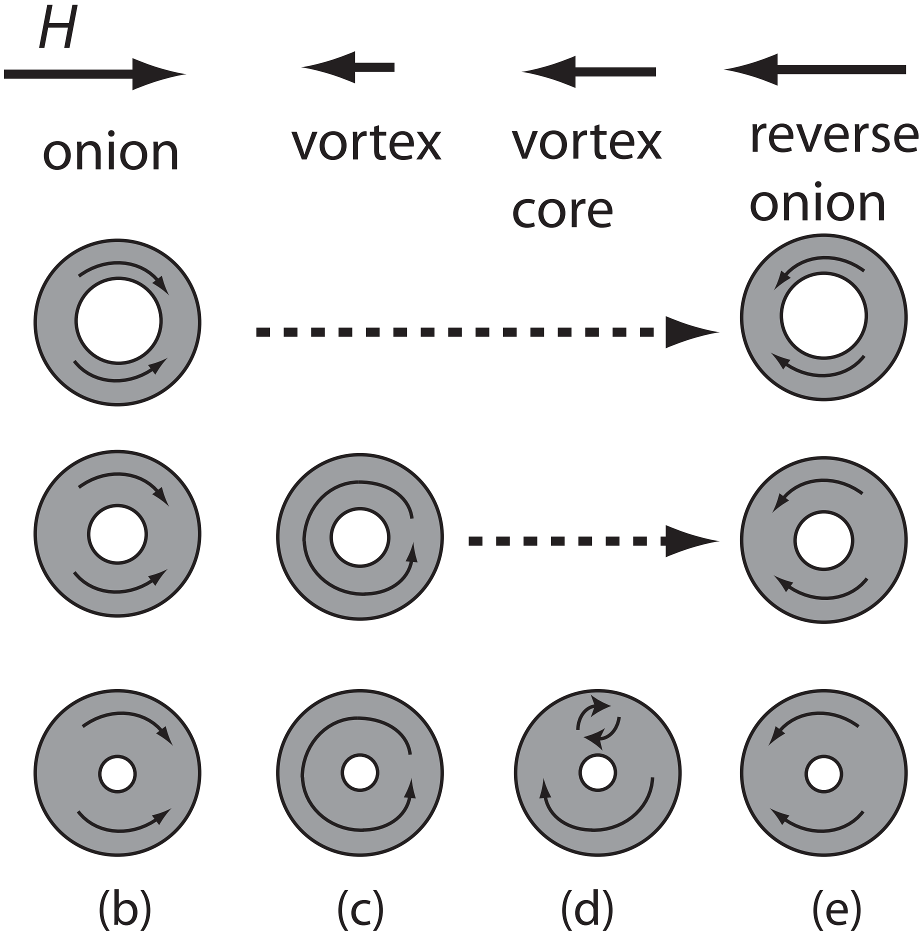

Figure 2.5: Possible reversal modes in ferromagnetic submicron rings. The involved reversal mode depends mainly on the ring width ([23]). The onion state features a head-to-head domain wall and the vortex state a stray field free head-to-tail domain wall. The vortex-core state is a modified global vortex with a small vortex configuration at one side of the ring. The state (a), characterized by a complete parallel alignment of all spins, is not displayed.

Two different configurations are described in literature [28, 29, 27] for a 180° head-to-head domain wall, namely a vortex and a transverse wall, in the onion state. Which domain wall prevails is influenced by the width and thickness of the ring. A phase diagram in [26] describes a theoretically and experimentally determined transition between both models. Figure 2.6, depicts both domain wall types using a thin magnetic stripe as simplified model structure.

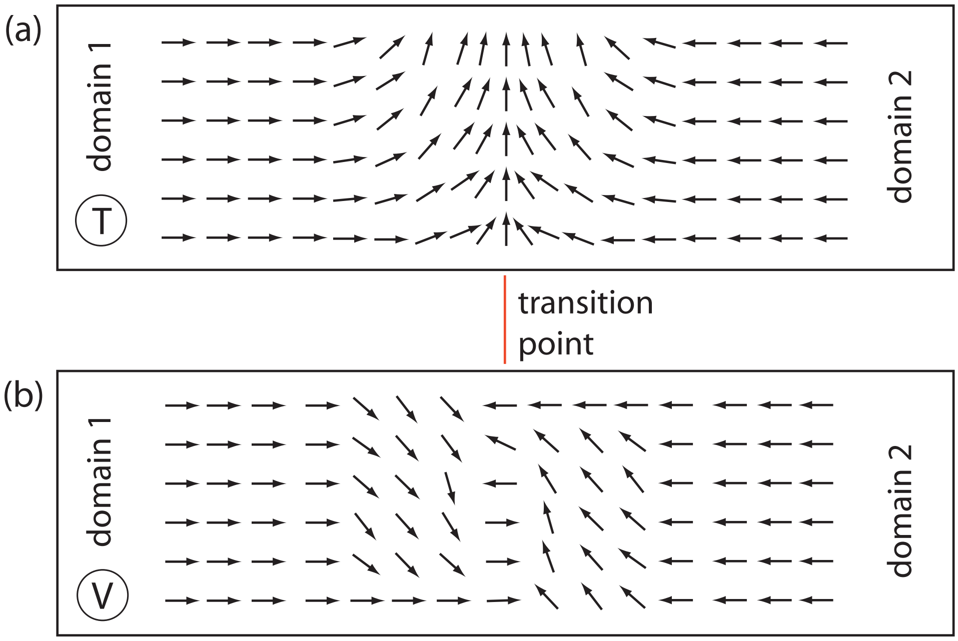

Figure 2.6: Simplified model of two possible head-to-head domain walls in a thin rectangular geometric structure. The upper figure depicts a transverse domain wall und the lower a vortex domain wall. This model is applicable to describe the head-to-head domain configuration in submicron rings.

Nanotubes

By dramatically increasing of the layer thickness of the previous presented rings we achieve a new type of structure, a magnetic tube. This structure can also be apprehend as a rolled up magnetic film. The tubular shape and thereby the shape anisotropy dominate the magnetic configuration and thus the magnetization reversal.

As shown in Fig. 2.7, three different reversal modes are possible in ferromagnetic nanotubes [30, 31]. The left scenario (a) corresponds to a coherent (simultaneous) rotation of all spins (local magnetic moments). In the center one (b), the spins rotate stepwise via nucleation and propagation of a vortex domain wall. In the right scenario (c), the reversal propagates as a transverse domain wall.

The present reversal mode in magnetic nanotubes depends on several parameters such as magnetic layer thickness, length, radius and the angle between the applied field and the long axis of the tube. In general, a vortex state is preferred in thin tubes [32]. The coherent mode is only favorable for short magnetic tubes, when the length of the tubes is in the same range of the wall size [30, 31] or in tubes with a very thick magnetic layer. In the regime of small aspect ratios, the influence of the shape anisotropy almost vanishes. The influence of the shape anisotropy in magnetic tubes can be covered by a magnetic material with a high magnetocrystalline energy.

The magnetic properties of ensemble structures are influenced by the dipole-dipole interaction of the single objects. This long range effect tends to align the spins in an antiferromagnetic configurations. This effect reduces the coercivity of ensemble to lower values, compared to a single object. Detailed investigation on this effect, especially for ferromagnetic nanotubes, are given in [31, 33].

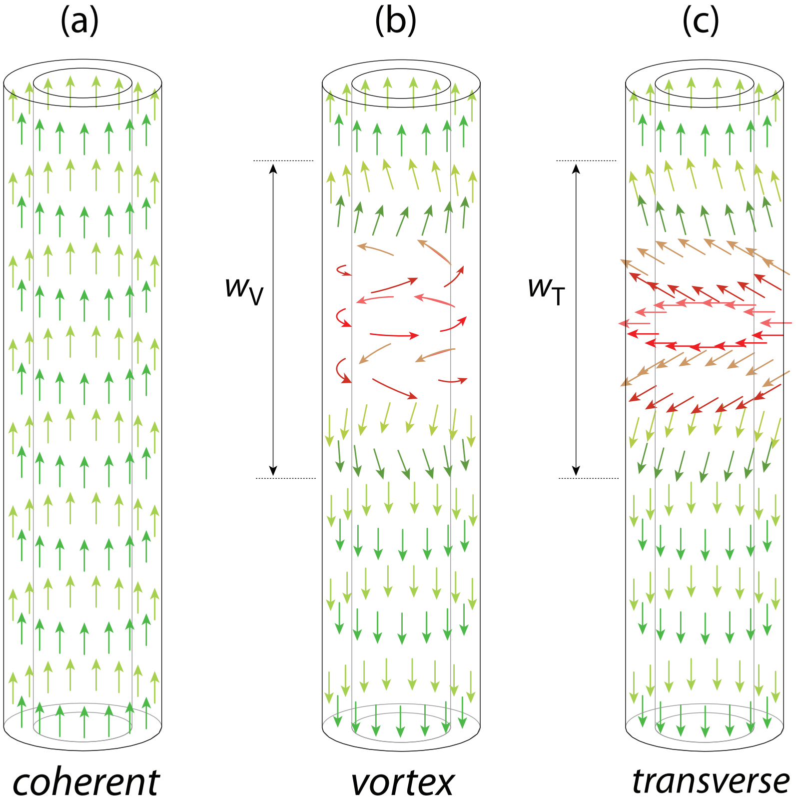

Figure 2.7: Possible magnetization reversal modes in magnetic nanotubes. The orientations of the local magnetic moments are displayed by the arrows. (a) coherent mode reversal, (b) vortex mode reversal, with a domain wall of thickness w_{v}. (c) transverse mode reversal, with a domain wall of thickness w_{t}.

2.4 Single-domain particles

Below a certain size, magnetic particles feature a single domain configuration. The minimization of the total energy forbids the development of a domain wall. A single-domain particle reveals a high magnetostatic energy E_{ms}, but without a contribution from the domain wall energy E_{dw}. A multi-domain particle exhibits an opposite behavior. The magnetostatic energy is reduced and the domain wall energy is increased, as displayed in Fig. 2.8.

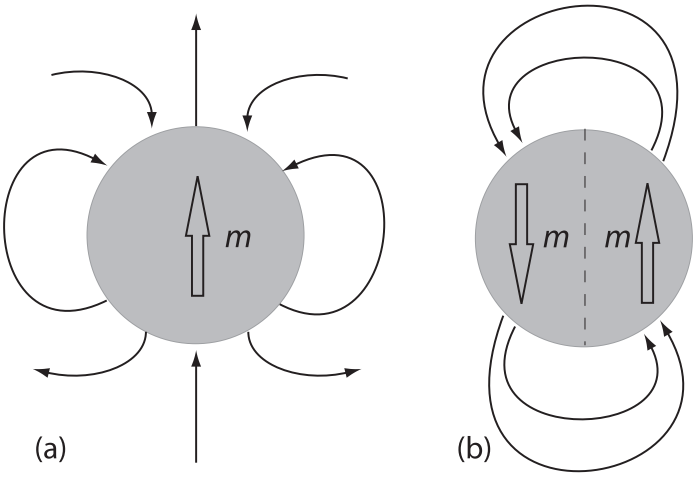

Figure 2.8: Competition between a (a) single- and (b) multi-domain state as a consequence of the involved magnetostatic and domain wall energy.

The critical radius, r_{c}, that determines the transition between single-domain and multi-domain states can be estimated by the dependence of the energy terms involved on the radius. The domain wall energy is proportional to r^2 and the magnetostatic energy proportional to r^3. As shown in Fig. 2.9, the intersection between both curves determines the critical radius.

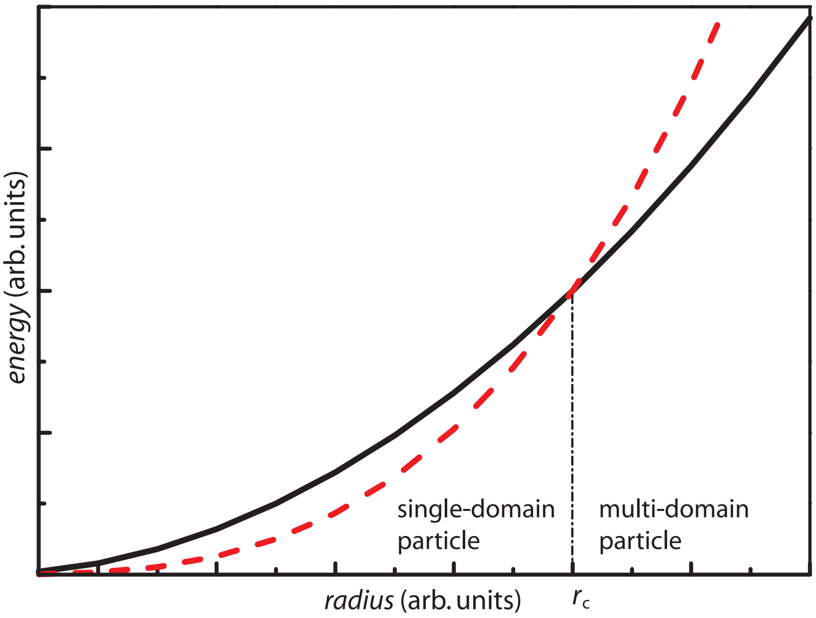

Figure 2.9: Sum of magnetostatic and domain wall energies as a function of the particle radius. The point r_{c} defines the transition between single- to multi-domain configuration.

2.4.1 Magnetization reversal mechanism for single-domain particles

In single-domain particles the magnetization reversal process is determined by the exceedingly large energy that is be necessary to create a domain wall. This reversal can be described by the Stoner-Wohlfarth model. It was originally deduced for the presence of shape anisotropy by Stoner and Wohlfarth [34]. This anisotropy contribution can be easily replaced by an uniaxial crystal anisotropy constant ([6], p.105). Equation 2.5 describes the magnetization reversal of single-domain particles in dependence of the angle θ between the applied field and the easy axis. For the case of an applied field parallel to the easy axis the calculations reveal a square magnetization isotherm and for an applied field perpendicular to the easy axis a non-hysteretic isotherm:

$$E = K_1 V \sin^2\theta - \vec{\mu}\vec{H}\cos\theta. \tag{2.5}$$

The main assumption of this model is the presence of small single-domain particles with a coherent rotation of all the spins and negligible interparticle interaction.

2.5 Temperature effects in confined structures

The term superparamagnetism describes the behavior of single-domain ferromagnetic particles below a certain size, with a vanishing coercive field. The reduction of the coercivity occurs due to the minimization of the anisotropy energy as a consequence of a smaller particle volume. This energy can be described by the product of a generalized anisotropy constant K and the particle volume V. The decrease reduces the anisotropy energy KV to the range of the thermal energy $k_\mathrm{B}T$. Due to this energy the moments can change their orientation.

For a constant particle size the appearance of a blocking temperature T_b is characteristic for superparamagnetic particles. Below this temperature, in the blocked state, they behave as hysteretic ferromagnetic particles. Above it, in the unblocked state, the hysteretic behavior vanishes. In the unblocked superparamagnetic state the moments are freely rotatable and unordered. They behave like paramagnets but with an increased magnetic moment and a saturation magnetization reached at lower fields. The prefix ”super” suggests this behavior. With the assumption of a vanishing anisotropy energy, the effect of superparamagnetism can be explained by the Langevin theory for paramagnets. Using this, the magnetization is given by:

$$\vec{M}(H,T) = N\vec{\mu}_{\mathrm{p}}(T)L(\alpha) \qquad \text{with} \tag{2.6}$$

$$L(\alpha) = \coth\alpha - \frac{1}{\alpha} \qquad \alpha = \frac{\vec{\mu}_{\mathrm{p}}(T)\vec{H}}{k_{\mathrm{B}}T} \tag{2.7}$$

N denotes the particle number per unit volume and

$$\vec{\mu}_p(T) = \vec{\mu}_p(T=0)(1-\frac{T}{T_{\mathrm{C}}})^{1/2} \tag{2.8}$$

The relaxation time τ is defined by

$$\frac{1}{\tau} = f_0 \exp\left(-\alpha\right) \qquad \text{with} \qquad \alpha = \frac{K_1 V}{k_B T}. \tag{2.9}$$

The frequency f_0 is named attempt frequency and has only a small dependency on the magnetic field $\vec{H}$ and on T. Compared to the change of the exponent in Eq. 2.9 it can be handled as a constant value. An estimation of the value yields a typical range of $f_0 \approx 10^{10}\ s^{-1}$ ([6], p.94). The strong influence of the particle size to the relaxation time is displayed in the Eq. 2.9, in which the particle size belongs to the exponent. The following example illustrates this dependence: For cubic iron at room temperature, which is magnetized along the [110] direction, it follows with a radius of the particle of 4.4 nm a relaxation time of $6 \cdot 10^5$ s. If the particle size is reduced to 3.6 nm, the time is decreased to a value of 0.07 s. This effect shifts τ into the range of the experimental measurement time t_{exp}. The ratio between the relaxation and measurement time determines the stability of the magnetization. If $\tau \gg t_{\mathrm{exp}}$ the magnetization does not change during the measurement. This is an essential requirement for magnetic data storage devices. Superparamagnetism corresponds to the case $\tau \leq t_{\mathrm{exp}}$.

Chapter 3

Experimental setup

3.1 SQUID magnetometer

The SQUID-magnetometer *MPMS-2/XL^{TM}, QuantumDesign* is a state-of-the-art device for the investigation of the magnetic properties of materials. It combines an inductive technique with a SQUID based detection system. The inductive principle is also used in conventional magnetometers such as vibrating sample magnetometers and other ones. The integrative method takes the whole sample volume into account to determine the magnetization. A flux change is caused by a movement of the sample through the pickup coils, the response of a sample to an applied magnetic field induces a voltage in the pickup coils. This voltage is proportional to the magnetization of the sample. The SQUID magnetometer uses an improvement of this method. The pickup coils are made of a superconducting niobium wire and are wound as a second-order gradiometer (Fig. 3.1 (a)). This design reduces the background noise and the impact of stray fields. The ends of the pickup coils are coupled to a SQUID device (Fig. 3.1 (b)). It consists of a ring of superconducting material with a discontinuation at one side of the ring. This break is made out of a thin insulating barrier. With this setup the flux change is digitized and it is possible to count the change of flux in units of $\phi_0 = \frac{h}{2e}$. A detailed description of the system used is given in [35].

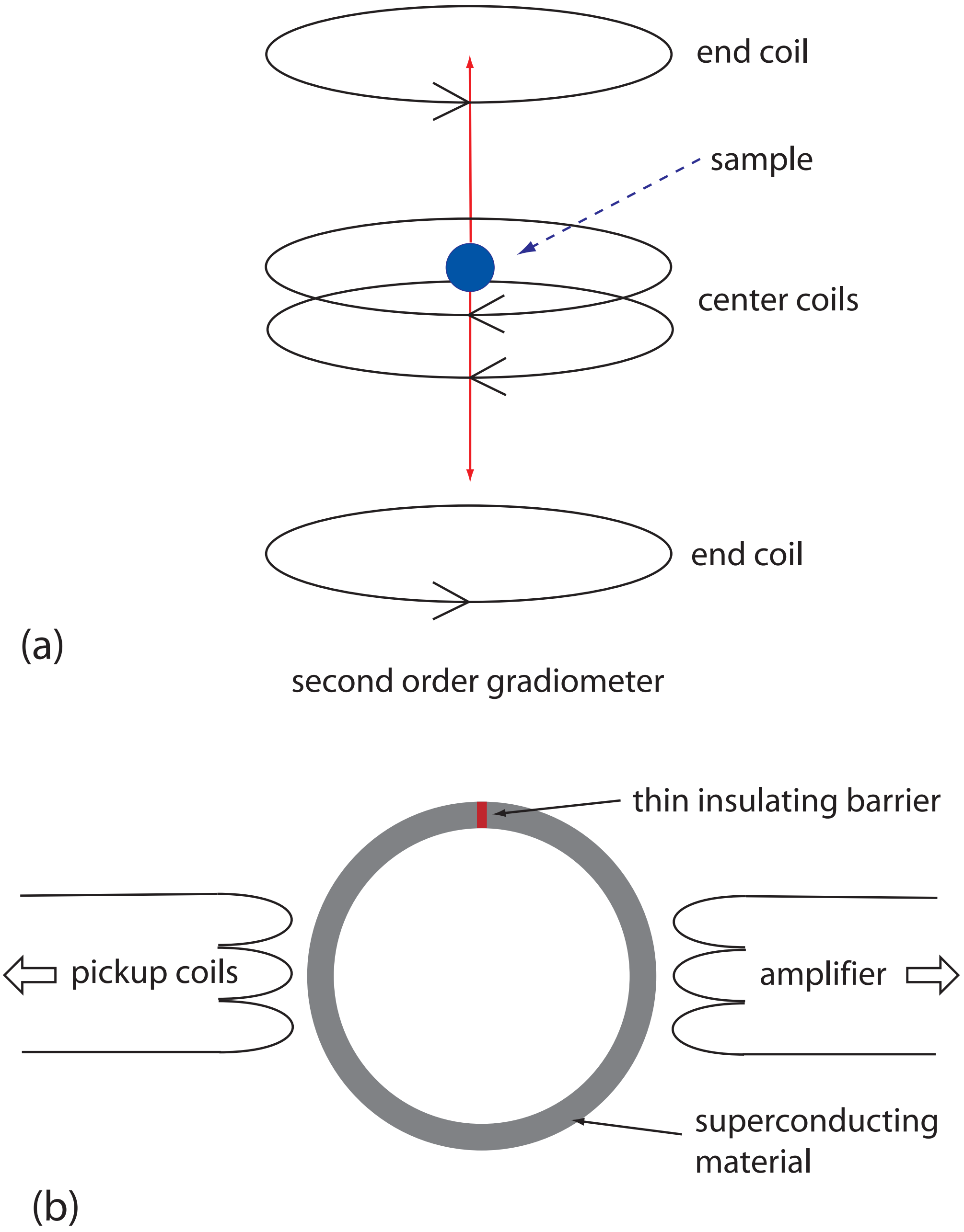

Figure 3.1: (a)Pickup coils wound as a gradiometer of second order. This coil design inhibits the influence of environmental noise. The sample is moved by a stepper motor. This movement causes a change of flux inside the coils. (b) Schematic drawing of a RF-SQUID ring. A RF-SQUID ring is characterized by an insulating barrier inside the ring. It allows the digitization of the flux-change recorded by the pickup coils.

All parts containing superconducting material, such as the pickup coils, the SQUID ring and additionally the magnetic field coils have to be cooled by liquid ^{4}He to reach the critical temperature[1] of the material. All these parts, except the SQUID-ring, are combined in a sample probe, displayed in Fig. 3.2. The SQUID ring is installed below it, a schematic drawing is shown in Fig. 3.1 (b).

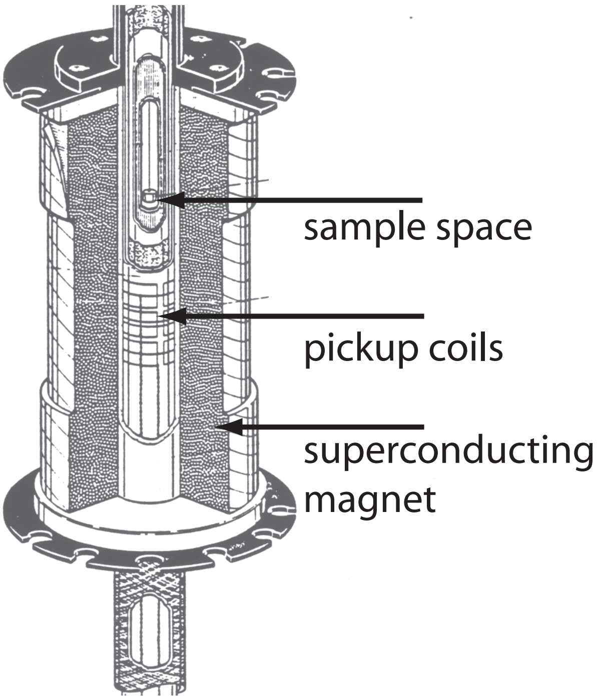

Figure 3.2: Drawing of the sample probe: This unit contains the sample space, the pickup coils and the magnetic field coils [36].

The temperature can be varied from 2 K up to 350 (400) K and the applied magnetic field up to 10 (50) kOe[2].

---

[1] $T_c = 9.2$ K

[2] The values inside the brackets specify the device parameters of the MPMS-XL.

3.2 DC magnetometry

DC magnetometry allows for the determination of the equilibrium magnetization of the sample. During the measurement a constant magnetic field is applied to the sample which is moved relative to the pickup coils by a stepper motor. The induced signal can be fitted by a response function of first order to determine the magnetic dipole moment (see Fig. 3.3). The calibration of the induced signal was performed with a palladium reference sample [37]. This sample provides a known temperature dependent susceptibility.

$$h(x) = \frac{1}{V_{1.\ \mathrm{coil}}} - \frac{2}{V_{\mathrm{center\ coil}}} + \frac{1}{V_{3.\ \mathrm{coil}}} \tag{3.1}$$

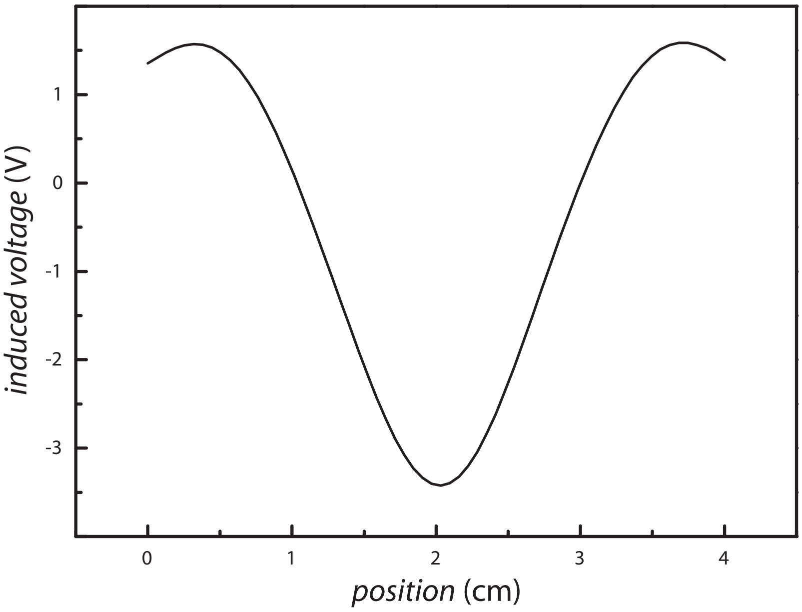

Figure 3.3: DC measurement of the palladium reference sample with a scan range of 4 cm.

3.2.1 Field- and temperature-dependent magnetization

Using the DC mode, the applied field and the temperature can be used as measurement parameter.

$M(T)$: The determination of the temperature-dependent magnetization can be realized by three different procedures:

- Zero Field Cooling (ZFC): Cooling of the sample in zero magnetic field and subsequent measurement with an applied field during the heating of the sample.
- Field Cooling (FC): Measurement of the magnetization in an applied field during cooling of the sample.
- Remanence (rem): Determination of the remanent magnetization during heating in a zero field of a previously saturated sample.

The different magnetization behaviors of ferromagnetic nanoparticles determined by the FC and ZFC procedure give information about the magnetization reversal mechanism at low temperatures, as displayed in Fig. 3.4. If the sample is cooled down in a zero field, all spins are randomly distributed and frozen in this state. At the beginning of the measurement (lowest temperature) the applied field is not sufficiently high to align the spins. With an increasing of the temperature, the spins are aligned parallel to the applied field and the magnetization is increased. When the maximum magnetization is reached, both procedures (FC and ZFC) are equal. This temperature point describes a transition between the irreversible and reversible magnetization. It is identified as the blocking temperature T_b explained by the superparamagnetic effect described in Sec. 2.5. The transition is shifted to lower temperatures with an increase of the magnetic field due to a compensation of the anisotropic interaction. The blocking temperature can be precisely determined if $\vec{H} \to 0$.

The relation between all three procedures is given by:

$$M_\mathrm{rem}(T) = M_\mathrm{FC}(T) - M_\mathrm{ZFC}(T) \tag{3.2}$$

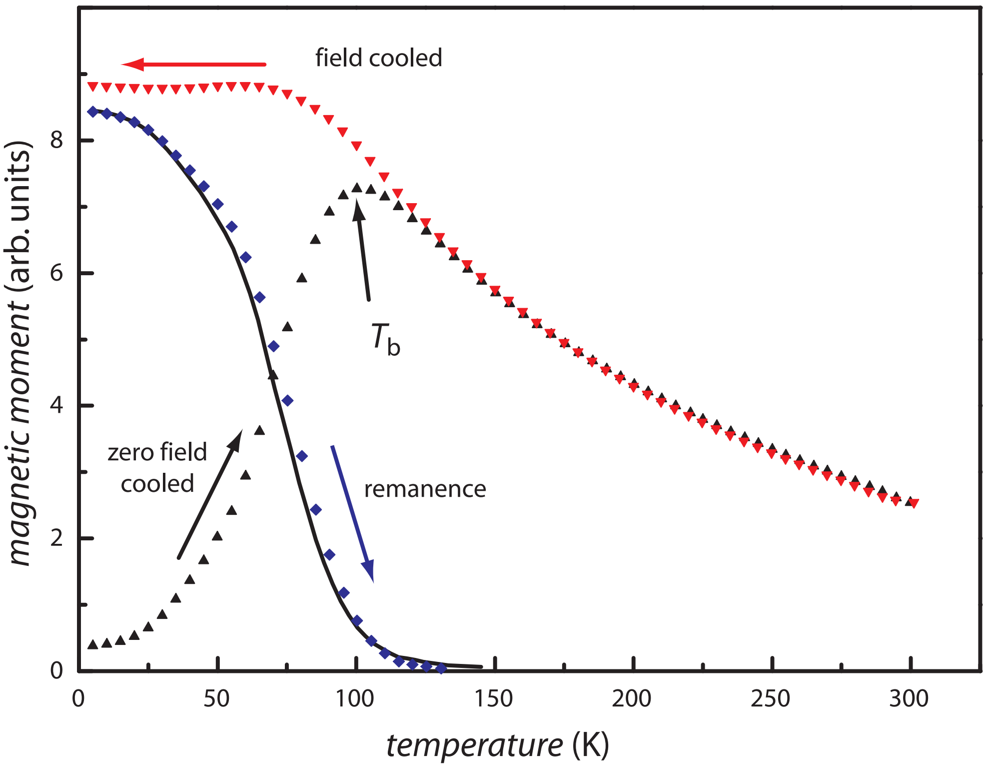

Figure 3.4: Exemplary temperature-dependent magnetization loops performed by using different measurement procedures. The appearance of a characteristic peak (T_b) during the zero field cooled procedure (ZFC) ▲ is an evidence for a superparamagnetic behavior. This peak is not provided by the field cooled (FC) ▼ measurement. ◆ displays the remanent magnetization after the FC procedure. At the temperature point where both curves (ZFC/FC) collapse the remanent magnetization vanishes. The black solid line displays the calculated remanence using Eq. 3.2.

Magnetization isotherms Figure 3.5 displays a typical magnetization isotherm of a ferromagnetic sample. Several magnetic parameters can be extracted from this field-dependent measurement at a constant temperature. At the saturation magnetization M_{sat} all magnetic moments are aligned parallel to a sufficiently strong applied field (a). The residual magnetization after a decrease of the applied field to zero is labeled as the remanent magnetization M_{rem} (b). The reverse field needed to reduce the magnetization to zero defines the coercive field H_{c} (c). In addition to these direct observables, the nucleation field can be obtained from these measurements. It specifies the state of the sample, after a saturation in high fields, at which the magnetization configuration starts to change. The relation between the nucleation and coercive fields can be quantified by the parameter squareness. It is given by the fraction of the magnetization between the saturated state and the remanent state ($\mathrm{M}_{\mathrm{sat}}/\mathrm{M}_{\mathrm{rem}}$). In the case of high squareness the coercive field equals to the nucleation field.

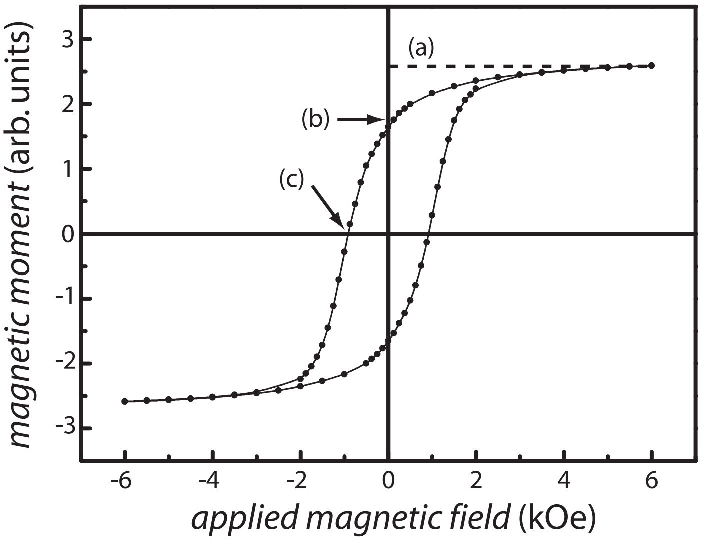

Figure 3.5: A typical magnetization isotherm of a ferromagnetic sample; point (a) defines the saturation magnetization $\mathrm{M}_{\mathrm{sat}}$, (b) the remanent magnetization M_{rem} at zero field and (c) the coercive field H_{c}, which defines the reverse field that is needed to reduce the magnetization to zero.

3.3 AC magnetometry

In contrast to the previously described DC magnetometry, the AC magnetometry allows the determination of the dynamic (time-dependent) magnetization of a sample. This technique uses a static magnetic field $\vec{H}_{\mathrm{DC}} \geq 0$, which is overlayered by an additional small alternating magnetic field $\vec{H}_{\mathrm{AC}}(\omega)$. This modulations reveal the time dependent magnetization. An introduction to this technique is given in [38].

If the excitation amplitude ($\vec{H}_{\mathrm{AC}}$) stays low enough, then it follows for the AC magnetic moment:

$$\vec{M}_{\mathrm{AC}} = (d\vec{M}/d\vec{H}) \times \vec{H}_{\mathrm{AC}} \sin(\omega t). \tag{3.3}$$

The susceptibility $\vec{\chi} = (d\vec{M}/d\vec{H})$ is the gradient of the curve of $\vec{M}(H)$. The flux change is only induced by the AC dependent magnetization. The determined differential or AC susceptibility consists of a real part χ' and an imaginary part χ''. The real part defines the slope of $M(H)$ and the imaginary part the energy dispersion inside the media. In case of low frequencies $f \rightarrow 0$, the imaginary part vanishes and the AC susceptibility becomes equal to the DC susceptibility.

AC susceptibility as a function of *T*. The temperature-dependent determination of the AC susceptibility reveals further information about the blocking processes in nanoparticles. ZFC measurements allow the determination of the occurring maxima of the imaginary part $\chi^{''}$, labeled as the freezing temperatures T_{f}. By plotting the frequency dependent values of T_{f} as an Arrhenius plot, it is possible to determine a mean barrier energy for the magnetization rotation from the slope of the linear curve, whereas the intersection with the x-axis defines the so-called “attempt-frequency” $\frac{1}{\tau_0}$.

3.3.1 Sample mounting

For a proper sample mounting, several requirements need to be fulfilled by the sample holder. The sample has to be fixed stable to prevent a sample shifting. In the other case, this could lead to a de-centering of the sample or - in particular for samples with an anisotropy - to a change of the angle between the magnetic field and the easy/hard axes, which results in an incorrectly determined magnetization. Furthermore the sample holder should consist of a material with low susceptibility and have a uniform material distribution to reduce a background signal from the sample holder. A sample holder is displayed in Fig. 3.6 (a), an uncolored polypropene (PP) straw is used as outer shell. The sample is glued with a cryogenic high vacuum grease[3] on a paper strip.

Gelatine capsules are used as a container for powder samples or other non-solid samples like suspended nanoparticles.

Horizontal sample rotator

For angle-dependent magnetization measurements, a special sample holder is available (Fig. 3.6 (b)). It provides a rotation of the sample over an angular range of 360°. This feature is integrated into the measuring software *MultiVu* and provides the angular dependence of the magnetization isotherms. The main disadvantage of this holder, which is made out of brass, is the large background signal caused by the impact of the material. The signal strength has to be larger than 10^{-4} emu to obtain a sufficiently precise measurement. The sample is fixed at the sample rotator with grease, as mentioned above.

---

[3] Apiezon N Grease

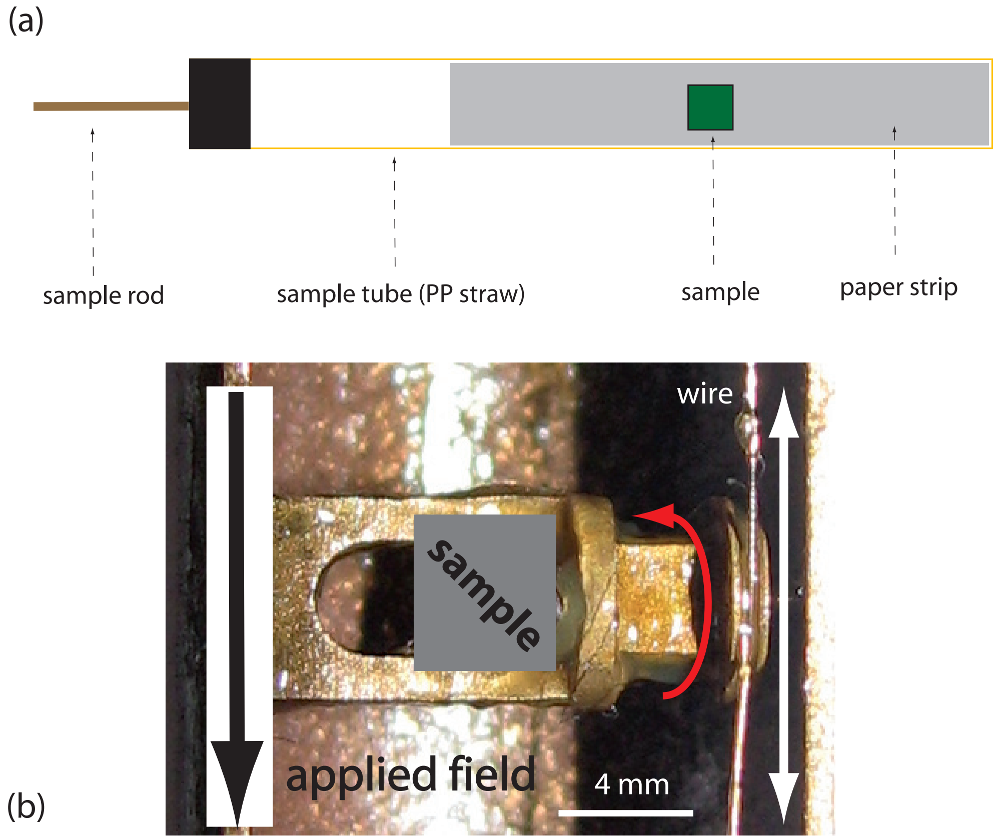

Figure 3.6: (a) Schematic drawing of a self-made sample holder. (b) The horizontal sample rotator is an add-on for the SQUID magnetometer and allows a rotation of the sample over 360°.

3.4 MOKE magnetometer

The MOKE (Magneto Optical Kerr Effect) magnetometer is based on the so-called Kerr effect, which describes the rotation of the plane of a polarized light beam after reflection on a magnetized sample surface ([39], Sec. 3.24). The rotation of the light, labeled as Kerr rotation angle θ_{Kerr}, is proportional to the magnetization of the sample. A schematic drawing of the setup used is displayed in Fig. 3.8. The main difference to a SQUID magnetometer, or in general, to induction based magnetometers, is the surface sensitivity of the magnetization determination. Diamagnetic influences from the substrate underneath the magnetic layer do not contribute to the measurements. This feature allows for the investigation of single nanostructures. On the other hand, unlike to inductive magnetometers, the MOKE setup used cannot determine the absolute magnetization values. The obtained values are relative and normalized to the saturated state. Further details about this commercially available magnetometer (*NanoMoke2^{TM} , Durham Magneto Optics Ltd.*) are given in Ref. [40]. It provides a sweeping of the applied field between 0.3 Hz and 28 Hz with an amplitude of up to ± 700 Oe for fast recording of magnetization isotherms. With the sample stage, which allows a rotation of the sample over a range of ± 165°, it is possible to determine the angle dependent coercive fields of this film or nanostructures. The setup presented operates at room temperature.

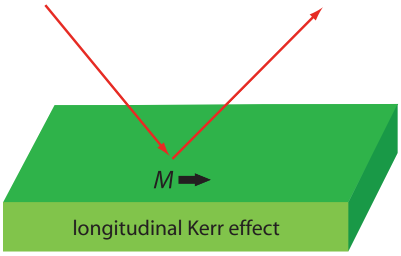

Figure 3.7: Schematic description of the used longitudinal Kerr effect.

The longitudinal Kerr effect is applied to investigate the in-plane magnetization (Fig. 3.7). This configuration is defined by a magnetization vector parallel to the plane of incidence. The rotation of linearly polarized light, which is reflected at the surface, is proportional the magnetization parallel to the plane of incidence.

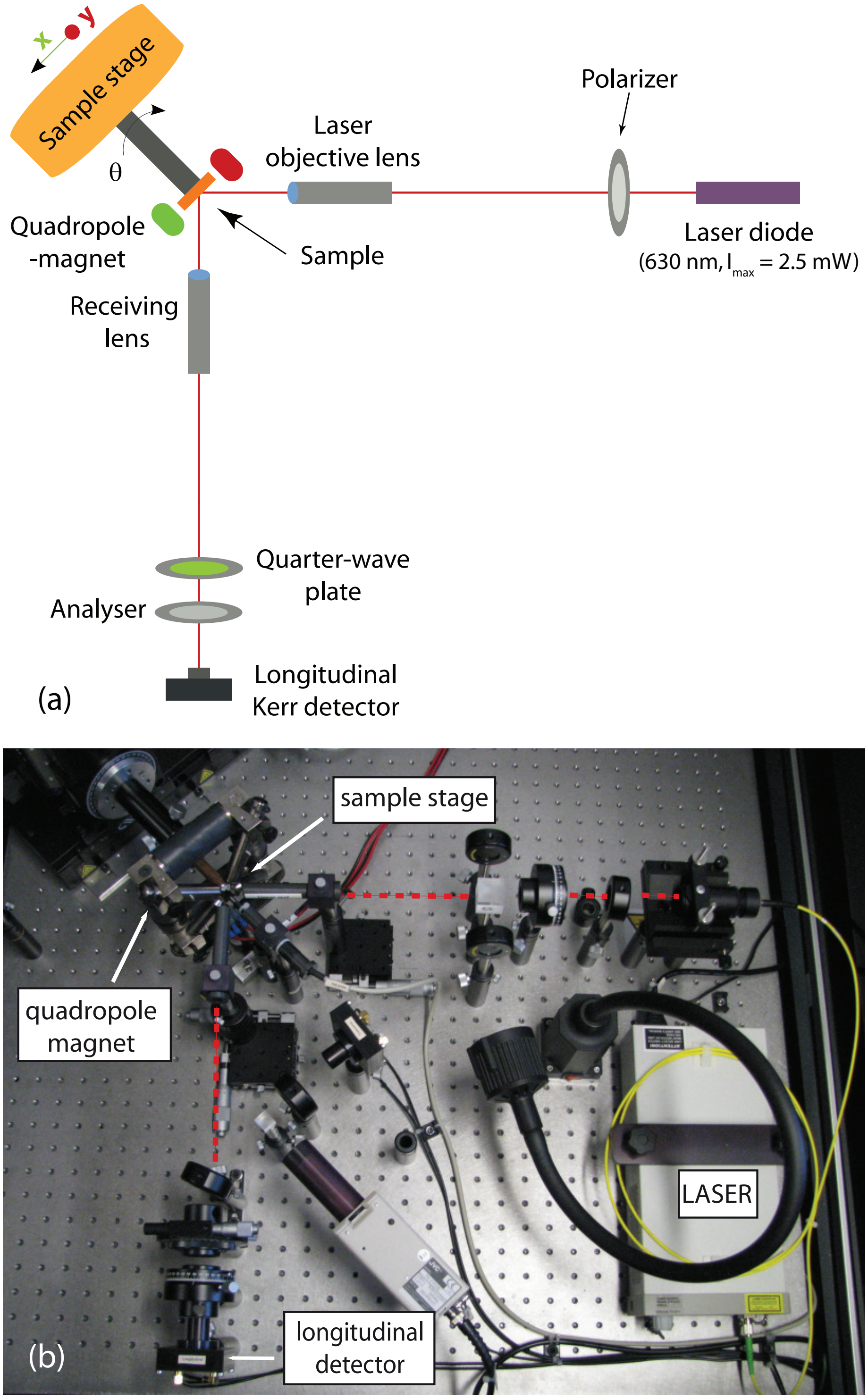

Figure 3.8: (a) Schematic drawing of the NanoMoke2$^{\mathrm{TM}}$ setup for the determination of the angle dependent-magnetization at room temperature. (b) Picture of the setup setup.

Chapter 4

Magnetic nanoparticles

For spherical or cubical nanosize particles, a new class of magnetic behavior was revealed in 1960's, namely superparamagnetism [41, 42, 34].

Recently, Sun et al. [1] presented a new approach for the synthesis of bimetallic magnetic nanoparticles (MNP). This hot organometallic synthesis has pushed the research on MNP forward during the last decade, with an ongoing series of investigations on transition metal nanoparticles. The main focus in these publications is on the FePt and the CoPt systems [2, 3, 43, 44]. Only few articles [4, 45] deal with the third magnetic transition metal, nickel, in a bimetallic system.

In general, such ferromagnetic single-domain particles offer a wide range of possible applications, with a recently increased focus on biomedical applications, such as magnetic resonance imaging, the hyperthermia of cancerous cells, and a further functionalization for drug delivery.

4.1 $\mathrm{Ni_xPt_{1-x}}$ nanoparticles

In this work, we investigate the static and dynamic magnetic properties of NiPt nanoparticles embedded in an organic matrix. The $\mathrm{Ni}_x\mathrm{Pt}_{1-x}$ nanoparticles were synthesized by Dr. Kirsten Ahrenstorf[1]. This hot organometallic preparation route was previously used for nanocrystals of $\mathrm{Fe}_x\mathrm{Pt}_{1-x}$ and $\mathrm{Co}_x\mathrm{Pt}_{1-x}$. The reduction of nickel(II)-acetate ($\mathrm{Ni(ac)_2}$) and platinium(II)-acetylacetonate ($\mathrm{Pt(acac)_2}$) in the presence of oleic acid, oleylamine and 1,2-hexadecanediol leads to almost spherical $\mathrm{Ni}_x\mathrm{Pt}_{1-x}$ particles with tunable

---

[1] Institute of Physical Chemistry, University of Hamburg.

composition and size (schematic synthesis route displayed in Fig. 4.1). Further information about the synthesis is given in [5] and [46].

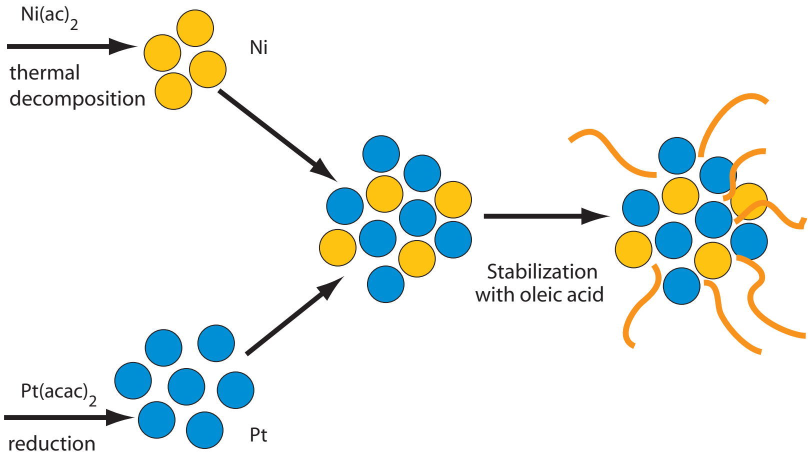

Figure 4.1: Schematic description of the NiPt synthesis route: The reduction of platinium(II)-acetylacetonate, nickel(II)-acetate (Ni(ac)$_2$), and (Pt(acac)$_2$) in the presence of stabilizing agents leads to Ni$_x$Pt$_{1-x}$ nanoparticles with tunable size and composition.

The properties of five samples with varying Ni content (42% to 75%) have been investigated. In a former work, a critical Ni concentration of 40% was found [35]. This concentration describes the transistion between paramagnetic and ferromagnetic states. This behavior also described in the literature for NiPt bulk alloys [47, 48, 49], as displayed in Fig. 4.2. NiPt multilayer as an approach for the synthesis of thin magnetic films with a perpendicular magnetic anisotropy are described in literature [50, 51].

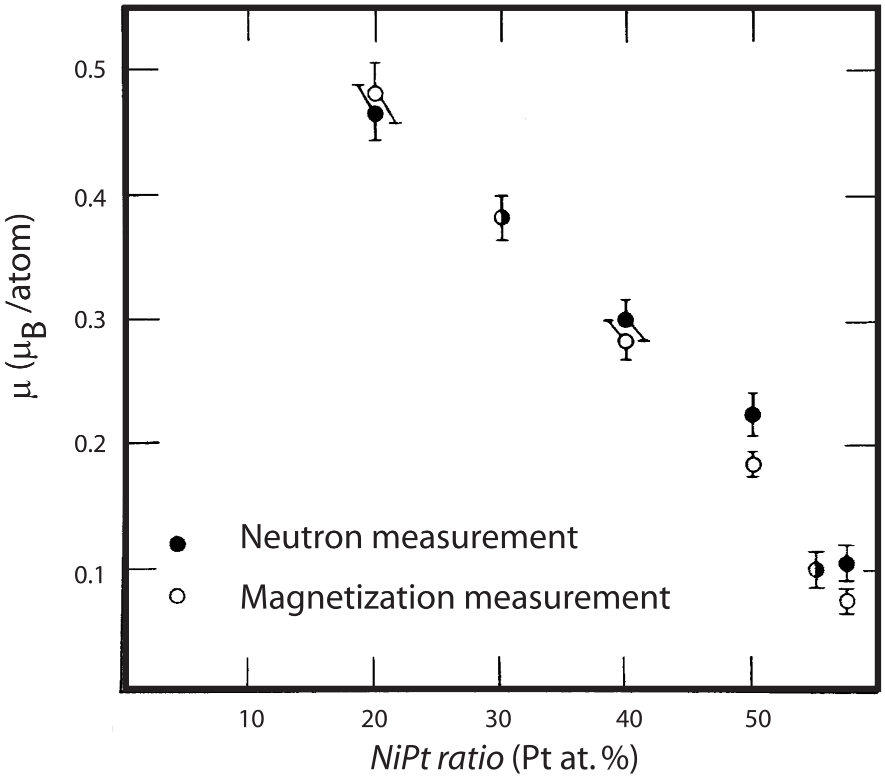

Figure 4.2: Ni content dependent magnetic moment of Ni-Pt alloys, determined by neutron and magnetization measurement. Taken from [49] and modified.

Characterization

The NiPt ratio of the investigated samples was determined by transmission electron microscopy using energy dispersive X-ray spectroscopy (TEM-EDX).

In the following, the main characterization route is exemplified for the sample $Ni_{0.73}Pt_{0.27}$. For the other samples, the results of this investigation are summarized in Tab. 4.1. The TEM micrographs and the magnetic measurements are displayed in the appendix. The size distribution and the shape of the particles was obtained by TEM micrograph processing, using *ImageJ* [52]. This program allows the automatic recognition of the particles displayed in the TEM micrographs. By adjusting the thresholds, the outline of the particles on the graph are set to the color black on a white background. Using this contrast the program determines the particle size. A Gaussian fit of the size distribution shows the mean area and the standard deviation. The shape was obtained visually. The exemplary result of the sample $Ni_{0.73}Pt_{0.27}$ is displayed in Fig. 4.3. All particles are mono-crystalline and have a disordered face-centered cubic (fcc) crystal structure [46].

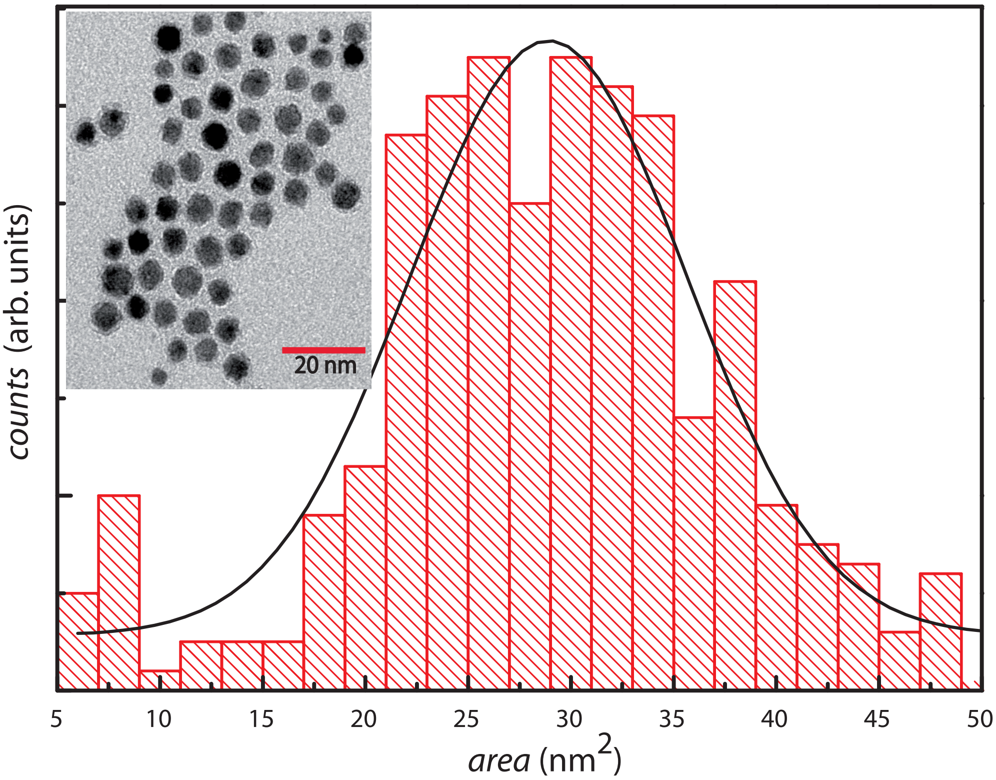

Figure 4.3: Inset: Exemplary TEM micrograph of the sample $Ni_{0.73}Pt_{0.27}$. The shape and the size distribution of the sample were determined by processing the TEM micrographs using *ImageJ* [52]. A Gaussian fit shows the mean area and the standard deviation.

Table 4.1 displays the the main characteristics of the five samples.

$\mathrm{Ni_xPt_{1-x}}$	mean area ($\mathrm{nm^2}$)	particle shape
x=0.42	nn	nn
x=0.45	33.5±14	□, ○
x=0.5	18±5.5	□, ○
x=0.65	27.7±9	□
x=0.73	28.9±13	○

Table 4.1: Characterization of the $\mathrm{Ni}_x\mathrm{Pt}_{1-x}$ nanoparticles: TEM micrograph processing yields the mean area, standard deviation and the shape of the particles. The symbols □ and ○ depict the observed particle shape

4.1.1 Magnetic properties

Figure 4.4 displays the magnetization isotherms recorded for two different temperatures, the measurement at 5 K reveals a coercive field of $H_\mathrm{c} = 737$ Oe. This value is dramatically reduced at a temperature of 10 K. This is an indication for a superparamagnetic (SPM) behavior.

An evidence for a SPM behavior, the characteristic blocking temperature T_b, can be revealed by a temperature dependent magnetization, determined in ZFC mode. For the investigated sample, a blocking temperature of 11.4 K was found (Fig. 4.5). At this point, the thermal energy is in the range of the energy barrier that prevents a magnetization reversal, as described in Sec. 2.5. In contrast to that, the dashed curve in Fig. 4.5 displays the temperature dependent magnetization obtained in FC mode. The difference of the magnetization determination procedures between both modes is typical for a superparamagnetic behavior.

For investigations of the blocking processes involved, the temperature-dependent ZFC AC susceptibility $\chi(\omega)$ was determined by using an AC magnetic field with an excitation field of $H_\mathrm{AC} = 4$ Oe between fixed frequencies of 0.01 Hz and 1 kHz in zero static field. The main focus is on the part of the AC susceptibility which defines the energy dispersion inside the particles during a measuring period of $(2\pi/\omega)$. This dispersion can be observed in the imaginary part of χ, χ''. As displayed in Fig. 4.6, the maxima of the temperature-dependent magnetization are shifted to higher temperatures with increasing frequency. These maxima are labeled as freezing tempera-

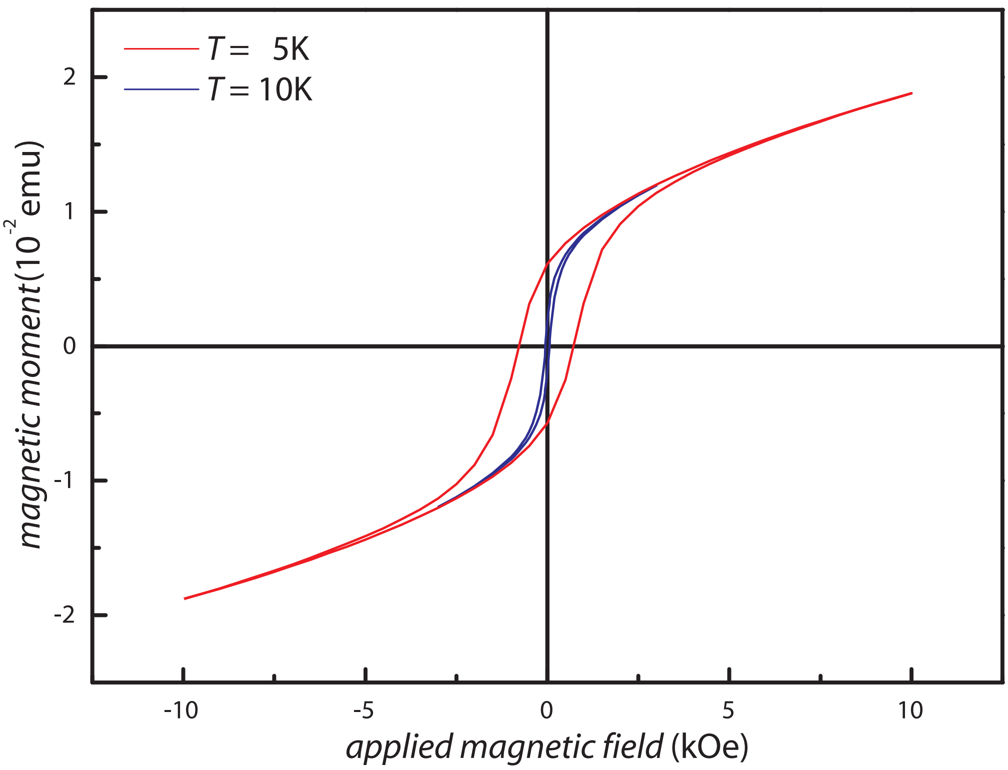

Figure 4.4: Magnetization isotherms of the sample $Ni_{0.73}Pt_{0.27}$ for two different temperatures. The measurement at 5 K (red curve) exhibits a coercive field of 737 Oe. The measurement at 10 K (blue curve) is in the same range as the blocking temperature, showing an almost vanishing coercivity.

tures T_f. The measurements allow the determination of a mean energy barrier involved in the blocking process. This barrier inhibits a rotation of the magnetic moment below T_f. The frequency dependence can be described by the Neel-Arrhenius law.

$$\tau(T_\mathrm{f}) \;=\; \tau_0 \;\exp\;(E_\mathrm{M}/k_\mathrm{B}T_\mathrm{f}) \tag{4.1}$$

If the reciprocal of $T_\mathrm{f}(\omega)$ is plotted against the logarithmic value of the particular frequency Fig. 4.7, a linear fit yields a slope and an intersection with the x-axis. The slope determines the value of the inverse energy barrier $k_\mathrm{B}/E_\mathrm{mean}$ and the intersection the so-called attempt frequency $f_0 = \frac{1}{\tau_0}$. This frequency is often interpreted as the smallest possible switching time.

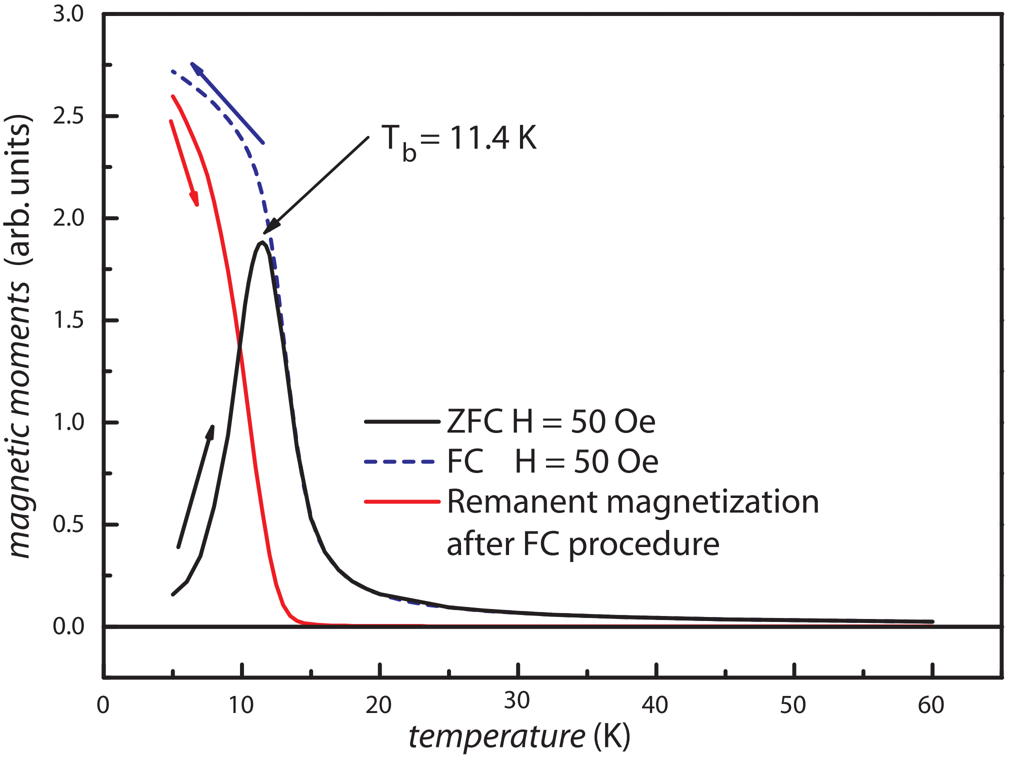

Figure 4.5: The temperature dependent magnetization measurement of the sample $\mathrm{Ni}_{0.73}\mathrm{Pt}_{0.27}$ in ZFC mode in a field of 50 Oe reveals a characteristic blocking temperature for superparamagnetic particles at 11.4 K. In addition, a field-cooled measurement and the subsequent determination of the remanent magnetization are shown. The arrows display the sweep directions.

The values obtained for τ_0 ($\approx\ 1^{-80}$ s), are unphysically small. Even with a correction, suggested in [2], the value is not in the range of $\approx\ 1^{-11}$ s [2]. Masunga et al. [53] describe a dramatic decrease of τ_0 for nanoparticles with an increasing Ni content. It is explained by the dipolar interaction that cannot be neglected, making the simple Neel-Arrhenius law inapplicable.

By interpreting the barrier energy as an anisotropy energy [2], it is possible to determine a general anisotropy constant. The particle volume was estimated by assuming a spherical shape and using the particle size determined by the TEM micrograph processing.

$$K_\mathrm{A} = \frac{E_\mathrm{A}}{V} \approx 2.4 \cdot 10^4\ \frac{\mathrm{J}}{\mathrm{m}^3} \tag{4.2}$$

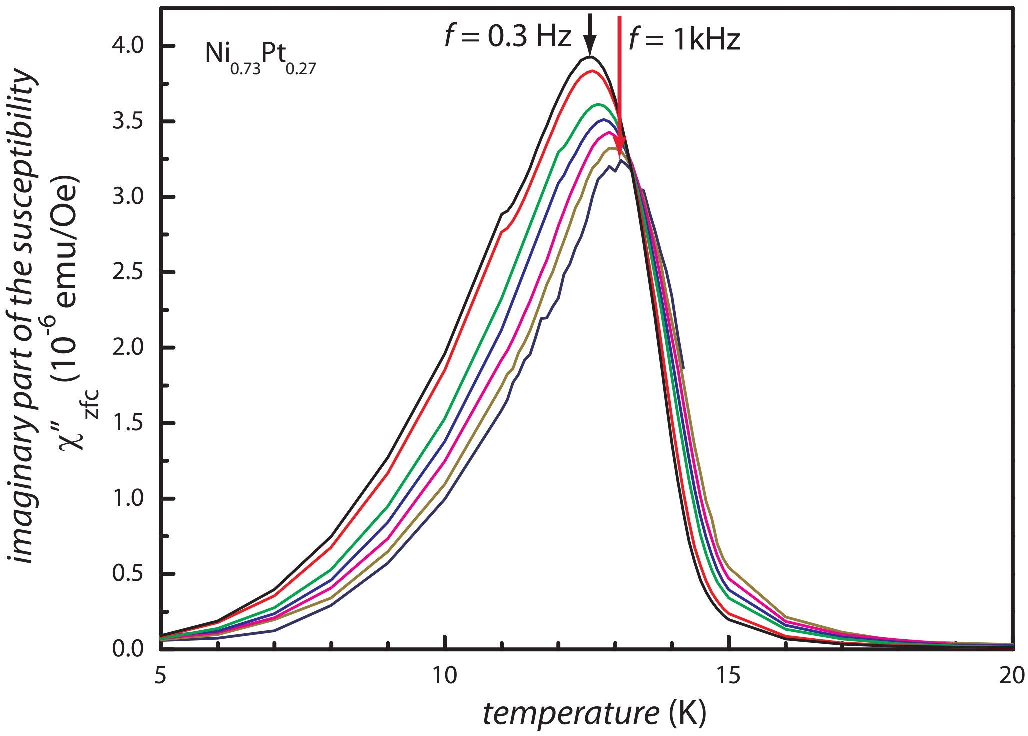

Figure 4.6: The imaginary part of the temperature dependent dynamic zero field susceptibility of the sample $\mathrm{Ni}_{0.73}\mathrm{Pt}_{0.27}$ for a frequency range between 0.3 Hz and 1 kHz reveals a strong correlation between the characteristic temperature peak, labeled as freezing temperature, and the frequency.

The direct comparison to the magnetocrystalline anisotropy energy of NiPt bulk alloys [54] with the same nickel content ($\approx\ 0.6 \cdot 10^4$ J/m^3) reveals, that additional energy terms dominate the generalized anisotropy constants. S. Morup [55] reported that the generalized anisotropy constant for Ni nanoparticles may be about 25 times larger than the intrinsic magnetocrystalline anisotropy constant found in macroscopic crystals. This increase is explained by several additional contributions to the anisotropy constant, such as the stress or the surface anisotropy [55]. These effects can also be responsible for the increase of the obtained anisotropy constant in our investigations. A contribution of an exchange bias due to an antiferro/ferromagnetic layer [45, 56] was not found during the measurements. A detailed investigation of the origin of anisotropy energies was not possible within the framework

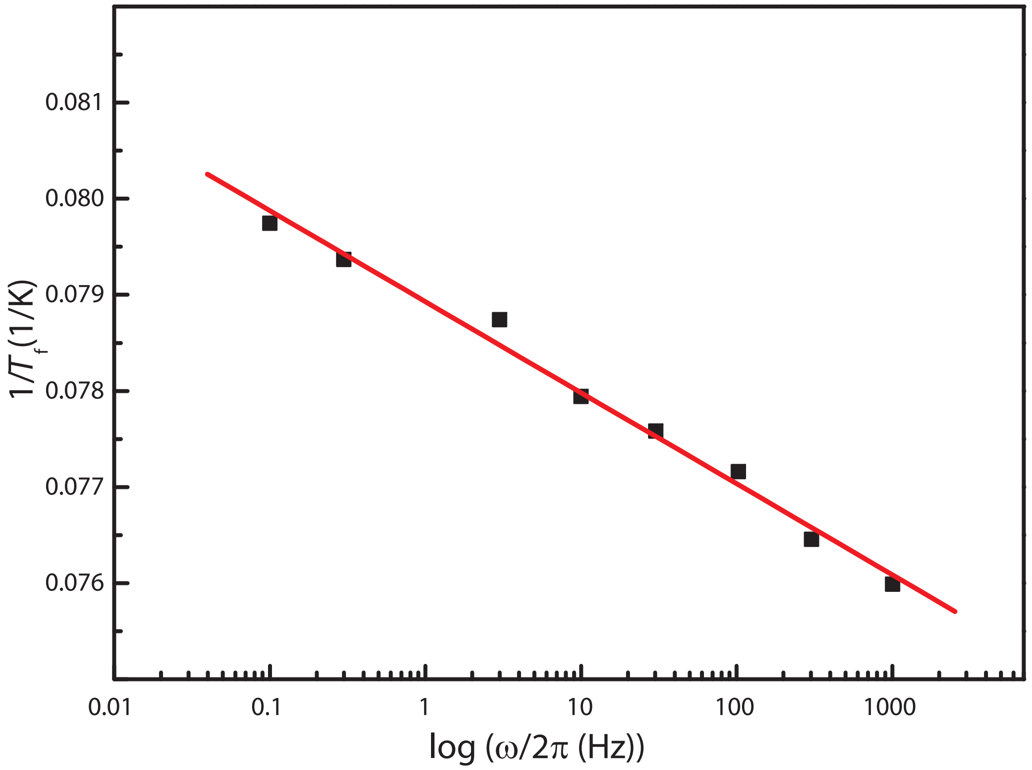

Figure 4.7: Arrhenius plot: $1/\mathrm{T}_\mathrm{f}(f)$ vs. *frequency*, the slope of the linear fit determines a mean energy barrier and the intersection, the so called attempt-frequency $f_0 = \frac{1}{\tau_0}$ of the sample $\mathrm{Ni}_{0.73}\mathrm{Pt}_{0.27}$.

of this work. All measurements and calculations described above were also applied to the remaining samples. The results are displayed in Tab. 4.2.

Ni_xPt_{1-x}	T_b(K)	E_m/k_B(K)	H_c (Oe)	$K_A(10^4 J/m^3)$	V (nm)^3
x=0.42	5.7	nn	18	nn	nn
x=0.45	6.25	35.86	230	☐ 0.26 ○ 0.34	☐ 193 ± 60 ○ 146 ± 45
x=0.5	7.4	57.87	327	☐ 1.05 ○ 1.4	☐ 76 ± 15 ○ 57 ± 11
x=0.65	10.1	57.4	732	☐ 0.54	☐ 146 ± 35
x=0.73	11.4	189.4	737	○ 2.4	○ 117 ± 40

Table 4.2: Summary of all investigated magnetic parameters; the blocking temperature T_b, the mean energy barrier E_m/k_B, and the calculated anisotropy constant assuming a cubic ☐ or spherical ○ particle shape.

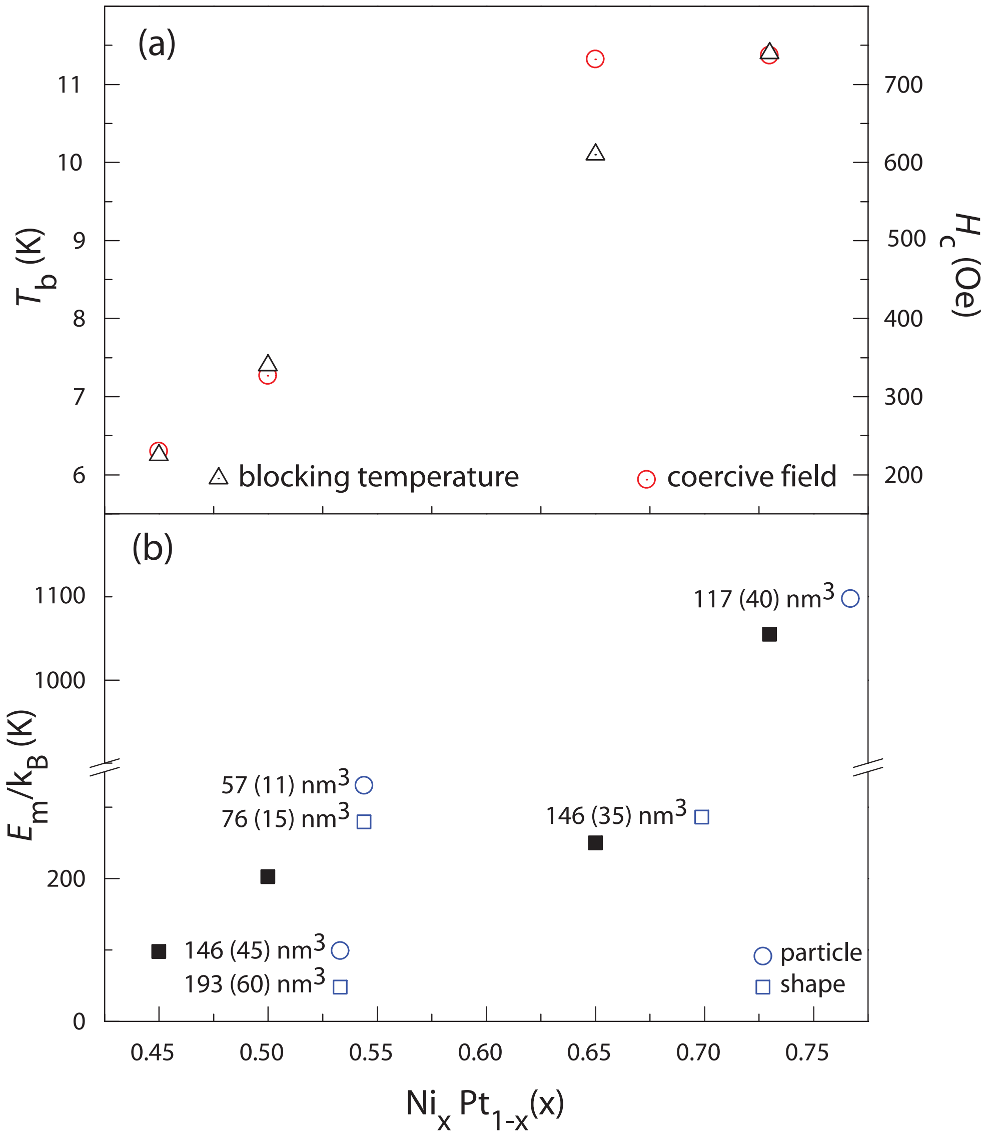

Figure 4.8: (a) Ni content dependent blocking temperatures △ and coercive fields ⊙. (b) Ni content dependent mean energy barrier ■ obtained by dynamic measurements. ○, □ depict the assumed particle shape and the mean particle size, including the standard deviation inside the brackets.

A clear dependence of the static and dynamic magnetic properties could not be revealed. The variation of the blocking temperature between ≈ 5 and 11 K is too small to obtain a direct influence of the parameters like size, shape and composition to this characteristic temperature. As described in Sec. 2.5, the particle size has a huge influence on the blocking temperature of the system. Due to the high standard deviation of the determined particles volumes, the relevance of this influence is not predictable.

The decreased coercive fields (at 5 K) for lower Ni contents are a direct result of the shift of the blocking temperature to lower values. The measurement temperatures are close to the blocking temperature. At this temperature the thermal fluctuations between both energy states lead to a decreased coercive field. To achieve a coercive field independent of the blocking temperature, the measurement temperature should be sufficiently lower ($T_{\mathrm{meas.}} \ll T_{\mathrm{b}}$).

The calculated generalized anisotropy constants for the four remaining samples (0.45 to 0.65 Ni content) are significantly smaller than of the Ni richest sample. This can be explained by the vanishing influence of the magnetocrystalline anisotropy for Ni contents below 0.70 [54]. For the obtained anisotropy constants, no clear dependence could be revealed. The Ni content only has a minor influence on the anisotropy energy in this range of compositions. Contributions from other terms cannot be separareted from the generalized constant, determined by using SQUID magnetometry. The obtained values of the mean energy barrier in units of $1/k_{\mathrm{b}}$ depict this dependence, for the samples with a Ni ratio of 0.5 ($T_{\mathrm{b}} = 7.4$ K) and 0.65 ($T_{\mathrm{b}} = 10.1$ K): one would expect also a higher energy barriers for an increased NiPt ratio but in fact both energy barriers are equal.

Summary

The preparative constraints were such, that it was not possible to tune the parameters, such as the NiPt ratio, the shape or the size, independently of each other. This situation prevents a detailed investigation on physical properties of the particles. Only a relation between the nickel content and the blocking temperature can be observed. It would be a challenge for further synthesis steps to control these parameters independently and introduce additional contributions to the anisotropy energy, such as an increased shape anisotropy by anisotropic structures, or a controlled oxidation resulting in an exchange bias.

As described by Mesnus et al. [48], the Curie temperature of NiPt alloys strongly depend on the Ni content. $\mathrm{Ni_{0.55}Pt_{0.5}}$ nanoparticles reveal a Curie temperature of 108 K [35], this value is in the range of the bulk value ($T_\mathrm{C} = 100$ K). The Curie temperatures of the other two bimetallic transition metal alloys are significantly above room temperature [57, 2]. This fact and the decreased anisotropy constants, compared to FePt and CoPt nanoparticles [2, 44] (up to two orders of magnitude), suggest that NiPt systems are not suitable as a system for data storage applications. However, as presented in the next section, these particles are promising for biomedical applications due to the superparamagnetic properties.

4.2 NiPt/CdSe nanoparticles

A further functionalization of magnetic nanoparticles extends the range of possible applications. Additional to the magnetic behavior optical properties can be added to these particles. This allows a use of these particles in biomedical applications, such as the in-situ investigation of cells with two separate imaging methods (magnetic resonance imaging (MRI) and fluorescent imaging) [58, 59, 60]. In a second synthesis step, the $\mathrm{Ni_{0.42}Pt_{0.58}}$ nanoparticles described in the previous section were covered by a semiconducting CdSe layer to build a hybrid particle having a core/shell structure. A schematic drawing of this structure is displayed in Fig. 4.9 (a). In Fig. 4.9 (b) a TEM micrograph depicts this coating. CdSe, a semiconducting material with a direct bandgap, exhibits optical activity. The properties of pure CdSe nanocrystals were investigated by photoluminescence (PL) spectroscopy by Torben Menke[2]. A brief description of this technique is given in Sec. 4.2.1. The synthesis step was performed by Jan Niehaus[3].

The NiPt/CdSe particles were suspended in chloroform ($\mathrm{CHCl_3}$). For the magnetic measurements, the suspension was dropped into a gelatin capsule. After drying in an atmospheric environment, the inner shell of the capsule is covered by a layer of the nanoparticles. For the investigation of the optical properties, the suspension was dropped on the surface of a Si substrate. This sample was dried as described previously.

---

[2] Institute of Applied Physics , University of Hamburg.

[3] Institute of Physical Chemistry, University of Hamburg.

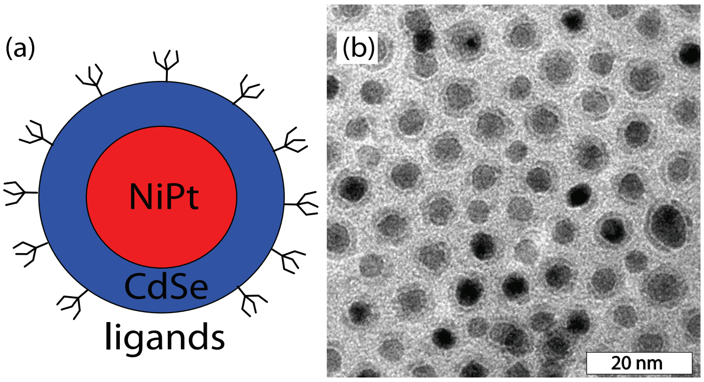

Figure 4.9: (a) Sketch of the NiPt/CdSe nanoparticles. (b) Transmission electron micrograph (TEM) of NiPt/CdSe particles. This micrograph reveals a structure with a magnetic core and a surrounding semiconducting layer.

4.2.1 Measurements

Optical properties

The photoluminescence principle is based on the absorption and emission of photons in a semiconducting material with a direct bandgap (Fig. 4.10). The incident photons excite an electron to shift from the valence to the conducting band, if the photon energy γ_1 is higher than the band-gap energy E_{gap} of the semiconductor. During this process, an electron/hole pair is generated. After this step, both relax to their respective band edge by the formation of phonons (quantized lattice vibration). This non-radiative process causes an energy transfer to the lattice. If both particles reach the band edge, they combine to the ground state under the emission of a photon of energy γ_2. For bulk CdSe, the photon energy is in the range of approx. 1.74 eV at room temperature.

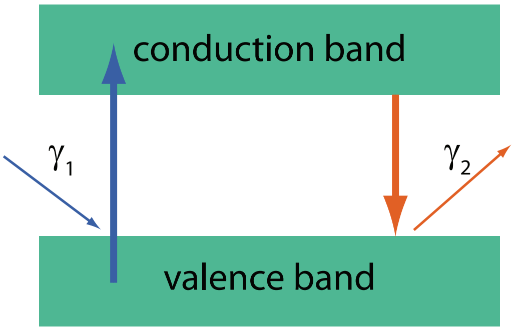

Figure 4.10: Principle of the photoluminescence (PL) for a semiconductor with a direct bandgap. After illumination of the sample, an electron is lifted from the valence band to the conduction band (blue arrow). The light energy must be higher than the energy of the band gap. An electron hole pair is formed. After a non-radiating relaxation with the lattice down to the band gap, the electron falls back into the valence band, emitting a photon (red arrow). This band gap is increased by the confinement in nanocrystals or by a reduction of the temperature.

If the size of the bulk material is reduced to the range of nanometers, quantum mechanical effects appear in the material [61]. Due to this confinement, an additional energy term (E_{c}) is added to the bulk bandgap energy:

$$E_{\mathrm{gap,total}} = E_{\mathrm{gap,bulk}} + E_c. \tag{4.3}$$

This term can be described by a quantum mechanical model of a particle in a one-dimensional quantum well of length L with the following wave function ψ and the quantized energy E:

$$\psi_n(x) = \sqrt{\frac{2}{L}} \sin \frac{n\pi x}{L}, \tag{4.4}$$

$$E_\mathrm{c} = \frac{\hbar\pi^2}{2mL^2} \quad \text{for} \quad n = 1. \tag{4.5}$$

This energy term only reaches appreciable magnitudes at high values of $\frac{1}{L}$, which appear at small length scales.

As presented by [61], we expect shift of the energy to a value of 2.1 eV due to confinement and to an additionally cooling at liquid helium temperatures. A detailed introduction to these effects and the measurement setup used is described also in [61].

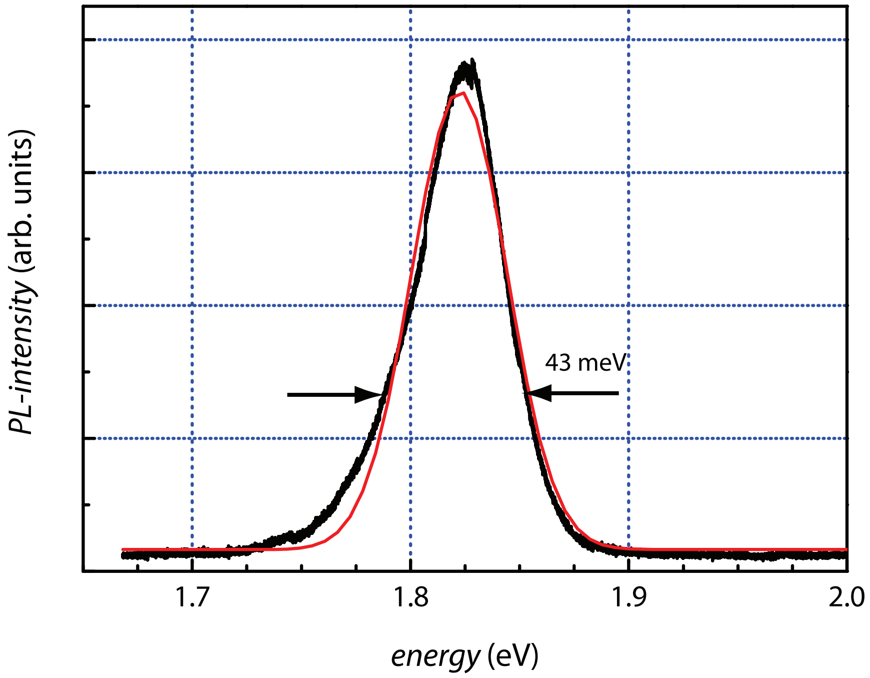

Figure 4.11: Measured spectrum of the NiPt/CdSe hybrid particle after the illumination with a green laser source ($\lambda = 523$ nm $\equiv$ 2.33 meV) at a temperature of $T = 3$ K. This spectrum exhibits a band gap of 1.82 eV, a Gaussian fit yields a full width at half maximum of 43 meV.

The ensemble measurement was obtained at a temperature $T = 3$ K with a green laser source ($\lambda = 523$ nm $\equiv 2.33$ eV). The energy of the laser has to be sufficiently higher than the band gap to allow the formation of an electron/hole pair. The resulting spectrum is displayed in Fig. 4.11. This spectrum exhibits a maximum at 1.82 eV. A Gaussian fit yields an energy width of 43 meV, the size distribution of the shells is responsible for this effect. For CdSe nanocrystals with a comparable size, we would expect an energy of 2.1 eV [62, 63]. A possible diffusion between both material systems might have caused this shift of 300 meV.

Magnetic properties

The magnetic properties of these hybrid particles were investigated by the SQUID measurement technique previously described. The ZFC measurement, shown in Fig. 4.12, reveals a blocking temperature of $T_\mathrm{b} = 3$ K . The appearance of this characteristic temperature is, as in pure NiPt nanoparticles, an evidence for a superparamagnetic behavior. The blocking temperature is dramatically reduced after the second synthesis step. This shift from a value of 5.7 K to 3 K could be explained by a possible diffusion between material of the core and the shell.

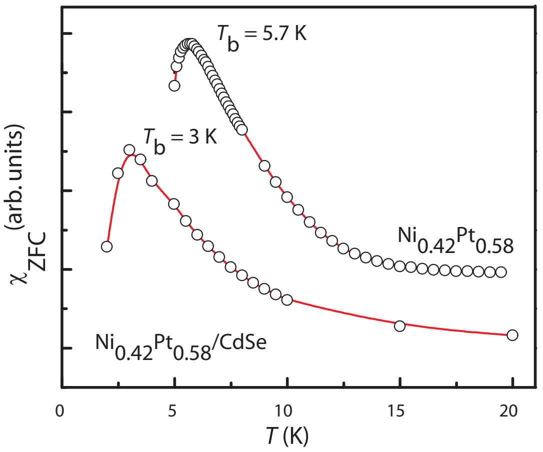

Figure 4.12: Temperature-dependent susceptibility (arb. units) determined in ZFC procedure for the NiPt and the NiPt/CdSe samples. After the second synthesis step (CdSe shell) the blocking temperature is decreased to 5.7 K from 3 K.

Summary

Thus, besides the magnetic properties of NiPt nanoparticles, a second functionality was successfully added by a further synthesis step. As mentioned in the previous chapter, a main challenge is the increase of the obtained blocking temperature and a covering of the hybrid particles with a biocompatible material such as SiO_2, which would make them suitable for in-vivo usage.

Chapter 5

Magnetic properties of patterned thin films

The fabrication of patterned thin magnetic films as a system for possible technology applications is widely described in literature. These kinds of templates can be prepared by nanoimprint [64], e-beam/inference lithography [64, 65] or by etching [66, 67] of substrates and subsequent deposition of magnetic materials. A detailed review about different synthesis methods is given in [68]. The domain configurations involved in single magnetic structures such as dots, rings or other shapes [69] are often investigated by MFM (magnetic force microscopy), MOKE magnetometry and micromagnetic simulations [70]. The interactions between the individual magnetic elements in ordered arrays are a focus of research [71]. Antidot structures, which are the reverse of dot structures, can be apprehended as a thin magnetic film with arranged holes [15, 18, 72]. Their magnetic properties are mainly dominated by the interaction of the magnetic lattice elements. Two different structures, namely submicron ferromagnetic rings and thin magnetic films deposited on structured surfaces are presented in this chapter.

5.1 Submicron ferromagnetic rings

The static and dynamic magnetic properties of ferromagnetic submicron rings have been in focus of research for about one decade. The research on this topic has mainly focused on the dynamic properties determined by ferromagnetic resonance experiments and other techniques. The static magnetization properties were determined by MOKE magnetometry [21, 73], PEEM (photoemission electron microscopy) [27] or by simulations [21, 22, 23]. The aim of this work is the investigation of the static magnetization properties obtained by SQUID magnetometry. This includes the influence of the ring width on the different states of magnetization and the appearance of these states during magnetization isotherm minor loops.

5.1.1 Preparation

The ferromagnetic submicron rings were produced by e-beam lithography. This technique uses electrons to depolymerize a resist. The main advantages over conventional optical lithography are the possibility of maskless writing and the ability to achieve smaller structures due to the decreased wavelength of the electrons compared to the wavelength of light. The shape of the structures written can be designed by a CAD software[1] and a subsequent electronic transfer to the e-beam writer device. This allows for an easy design and fabrication of the structures. The writing unit is an optional add-on for standard scanning electron microscopes (SEM). The e-beam, which is normally used for imaging techniques, can write structures directly into the resist. For this, a *SUPRA 55^{TM}, Zeiss FE-SEM* was used. A schematic drawing of the structures written is displayed in Fig. 5.1.

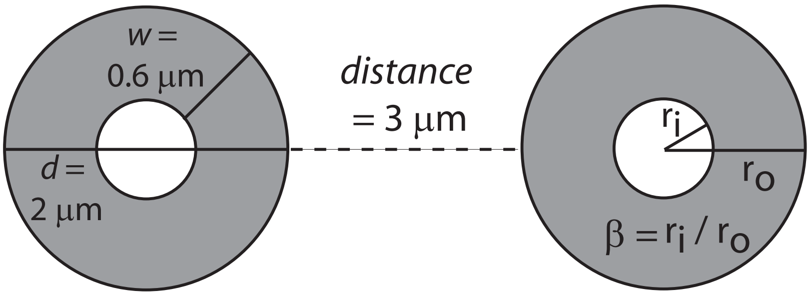

Figure 5.1: Schematic drawing of two rings, with a distance of 3 μm, an outer diameter of 2 μm and a width of 0.6 μm. The factor $\beta = r_\mathrm{i}/r_\mathrm{o}$ describes how ring-like the structure is. A value of $\beta = 1$ is identically with a vanishing ring width whereas $\beta = 0$ describes a disk. This structure was used as a template for the e-beam lithography preparation step.

---

[1] CAD computer aided design *Elphy^{TM}, Raith*

Figure 5.2 displays the synthesis procedure for the writing of ferromagnetic submicron rings. In the first step (a), a double stack layer of PMMA[2] resist is applied to a piece of Si substrate (4×4 mm^2) by spin coating. Both resists are positive resists, which means that the exposed area is removed after the development process. The resist of the bottom layer is more sensitive to the e-beam. This results in an inverted funnel-like hole. After the exposure procedure and a subsequent treatment with developer and stopper, a negative template of the desired structure is achieved (Fig. 5.2 (b)). This template is then coated with a 15 nm thick Permalloy layer by thermal evaporation in a high vacuum coating chamber and is subsequently covered with a 4 nm thick Au layer which inhibits the oxidation of the Permalloy layer. The Py was deposited under an angle of 90° to the substrate to prevent an unwanted additional anisotropy term, as described in [74]. In a last step (Fig. 5.2 (d)) the resist template is removed by acetone. This ”lift-off” is facilitated by the inverted funnel shape of the resist holes. All process parameters are mentioned in the appendix (D.2, D.3).

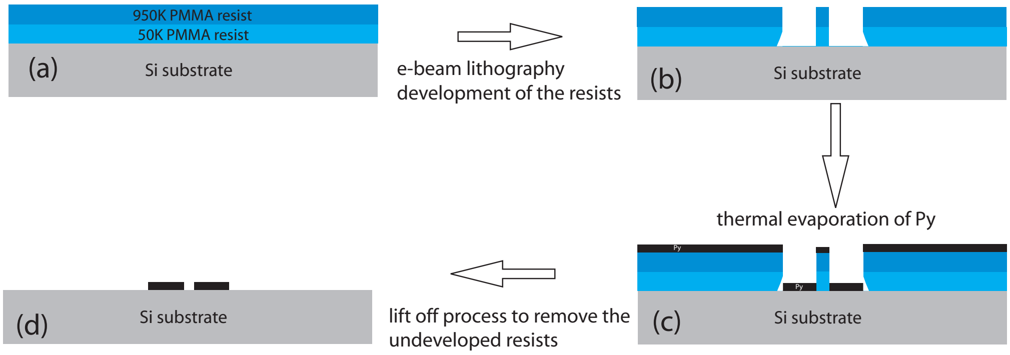

Figure 5.2: Preparation steps for the fabrication of submicron magnetic rings: (a) Spin coating of a Si-substrate with a double stack of resists (PMMA 50K/950K). (b) Exposure of the resists by e-beam and a subsequent development of the resists. The exposed resist is removed. The unexposed areas form a negative template for the rings. (c) Thermal evaporation of 20 nm thick Permalloy layer and 4 nm Au by an e-beam evaporation as protective layer. (d) Lift-off process to remove the undeveloped resists by acetone.

---

[2] PMMA: poly-methyl-methacrylate

The write field size determines the quantity and quality of the structures, which can be written into the resist without moving the SEM's sample stage. A large write field size reduces the achieved accuracy of the written structures. The used write field size of $200 \times 200\ \mu\mathrm{m}^2$ contains 1600 ring elements (40 rows and 40 columns). To achieve a measurable signal, this array was written sixteen times on a Si substrate, which results in approx. 25,000 written single structures (Fig. 5.3). This is necessary to improve the ratio between the positive ferromagnetic signal of the rings and the negative diamagnetic contribution of the substrate. A further improvement is achieved by the use of special thin (250 μm) undoped Si substrates, which reduces the background signal. This substrate material exhibits a low, temperature independent, volume susceptibility, as displayed in Fig. 5.4. Other substrate materials, such as doped Si or GaAs exhibit higher, temperature-dependent volume susceptibilities. For example, the value of GaAs at 300 K is about eight times higher than the signal of the undoped Si substrate.

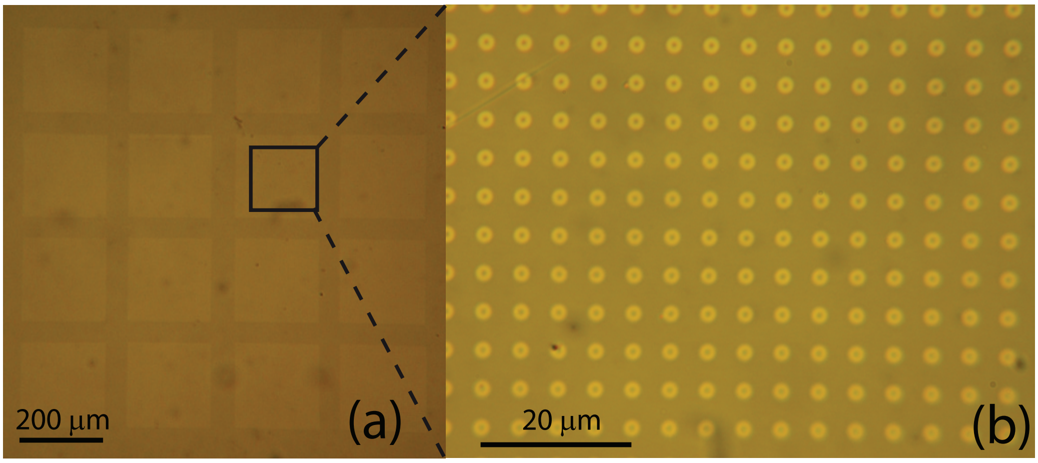

Figure 5.3: Optical microscope images of a negative resist template for submicron ring arrays with different magnification: (a) displays sixteen arrays of 40 × 40 rings. (b) displays an extended part of one array.

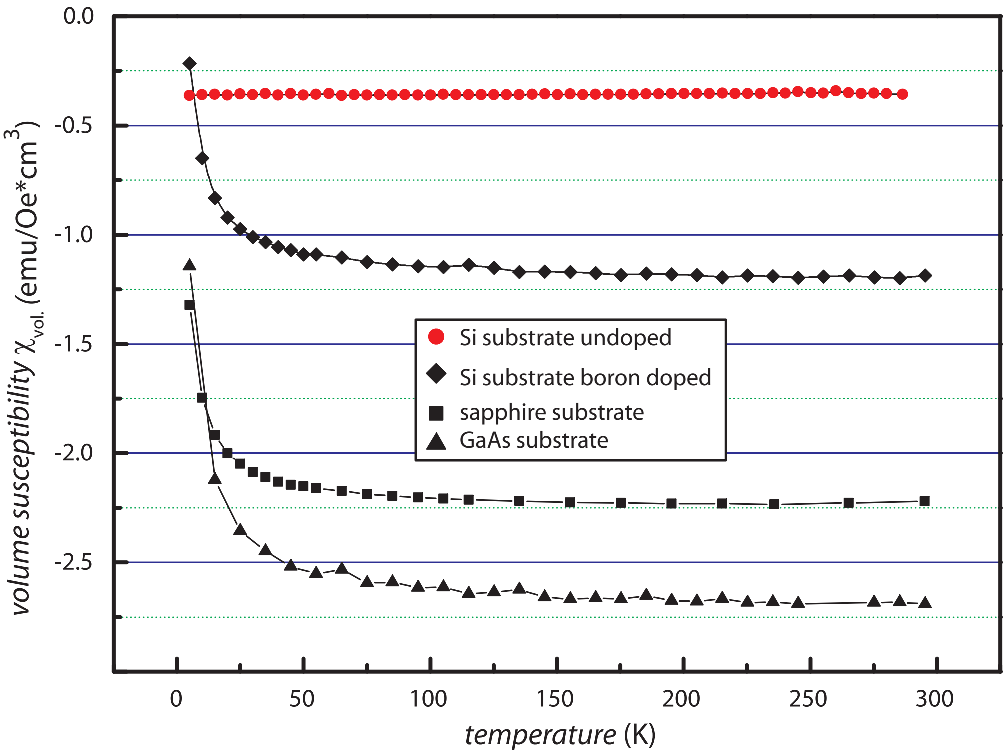

Figure 5.4: Temperature dependent volume susceptibility of different substrate materials obtained by SQUID magnetometry. The undoped Si substrate ● exhibits a low temperature independent volume susceptibility. This substrate was used for the preparation of the submicron rings.

5.1.2 Magnetic measurements

Figure 5.5 displays magnetization isotherms of the submicron ring array at 300 K with an external field applied in the plane of the substrate (± 500 Oe). These measurements reveal a mean coercive field of 50 Oe and the appearance of different magnetization states. After saturation in a magnetic field of 500 Oe (A) and a subsequent decrease of the field the so-called onion state (B) appears [23]. The state is defined by a head-to-head domain wall. With further decrease the vortex state (C) is reached first followed by the reverse onion. The oscillation of the measurement curve could be an indication for a meta-stable configuration until the saturation field is reached. Additionally, in the saturated state the return path of the curve does not overlap with the curve at the beginning of the measurement. A pinned local vortex state could provoke this effect. A minor loop (Fig. 5.6) was performed to prove the the appearance of the stray field free vortex state and investigate the origin of the observed unstable state. Instead of a decrease of the applied field to the saturated negative state (as in full magnetization loops), the field was reversed at the appearance of a step in the full magnetization isotherm curve. Due to this procedure the magnetization curve reveals a zero magnetization in a certain range of a applied field. This behavior is attributed to stray field free state in the vortex regime. In contrast to the full magnetization isotherms the minor loop exhibits no oscillations between a applied field of 100 Oe to 500 Oe. This supports the hypothesis of an unstable configuration during the full magnetization isotherms. The return path of the curve reaches at the saturated state the same magnetization values this leads to the conclusion that during a full magnetization isotherm a non-observable state such as a local vortex state appears. The state annihilates only at sufficiently high fields. It has been reported in the literature that the difference of the wall energies between the vortex and transverse wall is in the range of the thermal energy at room temperature [29].

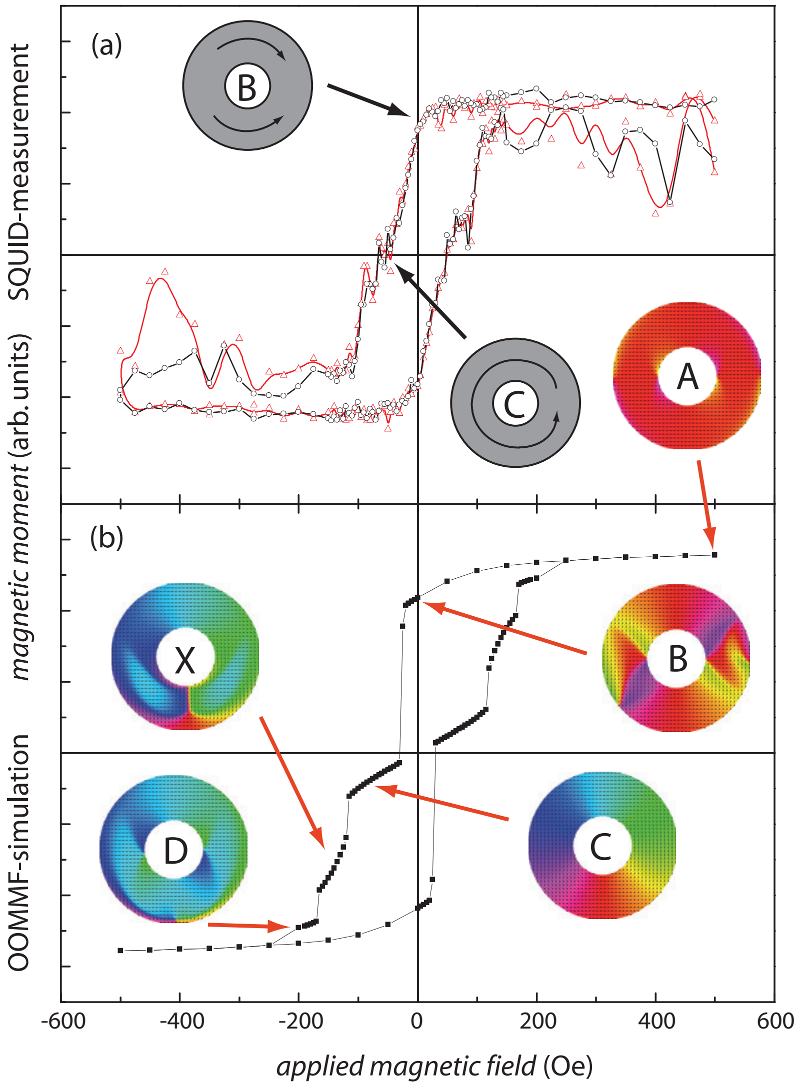

Figure 5.5: (a) Magnetization isotherms at 300 K with an applied field in plane of the substrate (± 500 Oe). After saturation, the magnetization isotherm displays at the remanent state the so-called onion-state (B) with the appearance of a head-to-head and tail-to-tail domain wall inside the ring. With a further decrease of the applied field, the magnetization isotherm exhibits a step (C). It can be attributed to the appearance of a stray-field-free vortex state. The coercive field is approximately 50 Oe. The oscillation of the measurement curve could be an indication for an unstable configuration until the saturation field is reached. (b) Performed micromagnetic simulation using OOMMF. The calculated magnetization isotherm exhibits almost the same coercive field and reveals the observed onion and vortex state during the recorded magnetization isotherms.

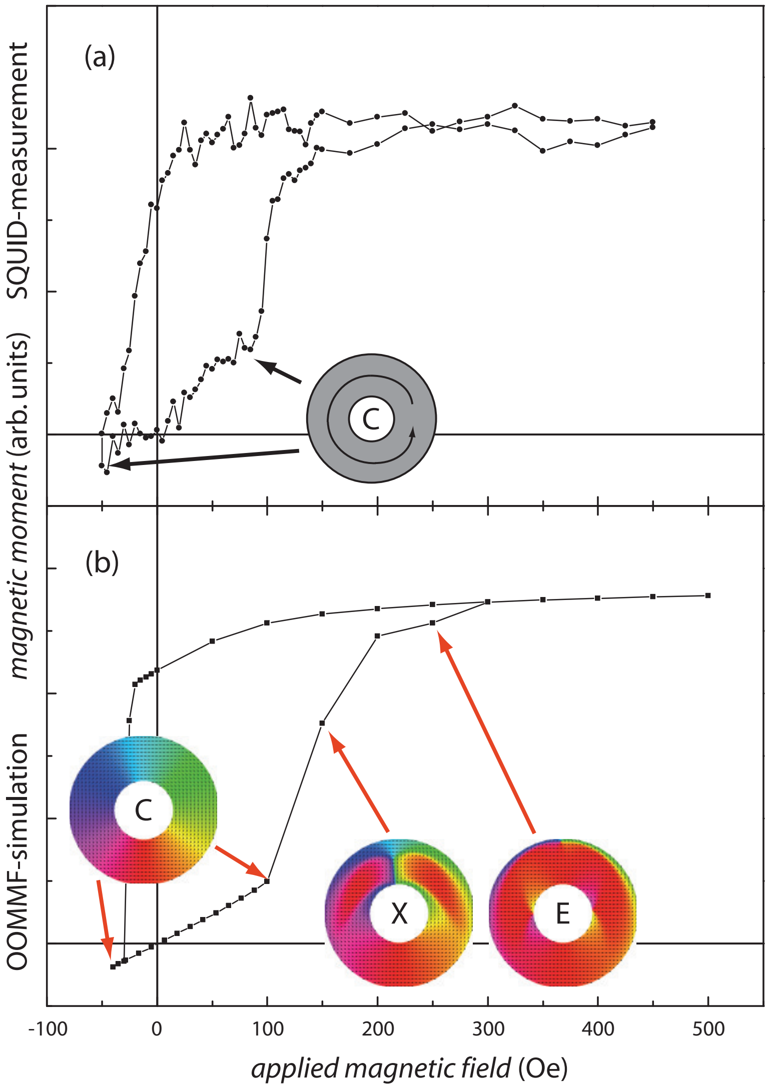

Figure 5.6: (a) Magnetization isotherm minor loop at 300 K with an applied field in plane of the substrate. The reverse point is identical with the appearance of a step in the magnetization isotherm loop displayed in Fig. 5.5. At this point the rings exhibit a vortex domain configuration. (b) Perfomed micromagnetic simulation by OOMMF reveals the vortex state (C) and the transition to the vortex-core (E) via an unphysical domain configuration.

5.1.3 Micromagnetic calculations

In order to determine the field dependent domain wall configurations micromagnetic simulations *OOMMF* [75] were performed. The micromagnetic framework utilizes the time-dependent Landau-Lifshitz-Gilbert equation:

$$\frac{\partial \vec{M}}{\partial t} = -|\gamma| \vec{M} \times \vec{H}_{\mathrm{eff}} + \alpha \frac{\vec{M}}{M_{\mathrm{s}}} \times \frac{\partial \vec{M}}{\partial t} \tag{5.1}$$

to determine the spin configuration of each field increment. The effective field term $\vec{H}_{\mathrm{eff}}$ used in this equation consists of several contributions including the exchange, anisotropy, dipole-dipole and Zeeman interaction. γ is the gyro magnetic ratio and α the phenomenological damping factor of the precession. During the calculation process the framework calculates a spin configuration with the lowest energy state. This step is repeated for all field increments. The calculations reveal for each step a possible configuration of the magnetic moments of a single submicron ring. Due to the distance between the ring elements, which results in a negligible interaction between the elements, it is suffices to consider a single ring structure during the calculations, as displayed in Fig. 5.1. From the magnetic snapshots the magnetization isotherms can be calculated. The snapshots and parameters used are displayed in appendix B.

The simulation for a full magnetization isotherm loop (Fig. 5.5 (b)) starts with a sufficiently high field (500 Oe) to align all magnetic moments parallel to the applied field (A). After a stepwise decrease of the applied magnetic field, the onion state appears at zero field (B). From this head-to-head state, the ring switches with a further decrease of the magnetic field to the flux-closed vortex state (C). This configuration is stable up to a certain negative magnetic field (indicated by the arrows). Both states were also found during the recorded magnetization isotherms (Fig. 5.5 (a)). The calculated ring configuration changes from the global vortex state (C) to a vortex-core state (D) via a configuration displayed in (X), which consists out of a mixture of vortex and transverse domain wall. This domain wall type is not reported in the literature as a possible spin configuration for this kind of structures. It is more reasonable, that the high symmetry of the structure is responsible for this calculation artefact [76].

In addition to the recorded minor magnetization isotherm (Fig. 5.6 (a)), calculations for a minor loop were performed. The magnetic spin configuration was calculated from the reverse field up to 500 Oe again (Fig. 5.6 (b)). At the starting point of -40 Oe the structure exhibits a global vortex config-

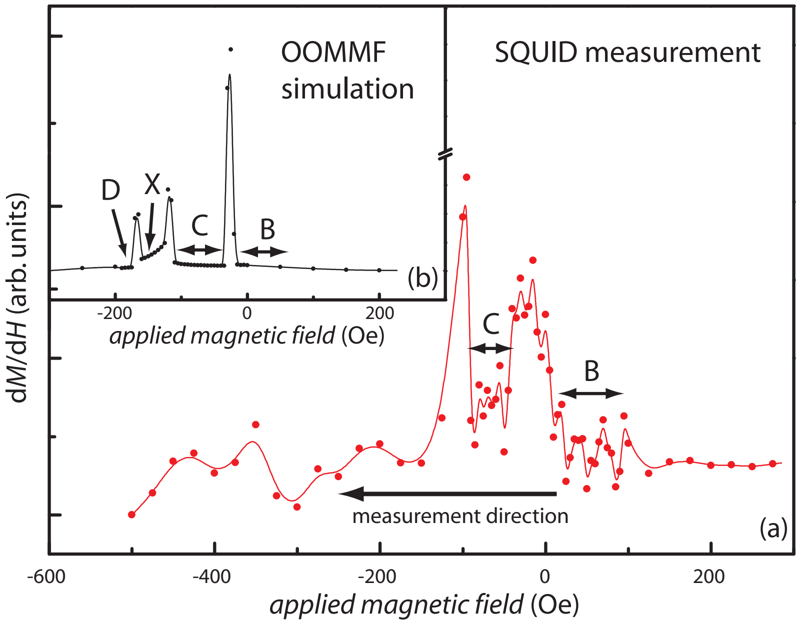

Figure 5.7: The derivative of the magnetization ($\frac{\mathrm{d}M}{\mathrm{d}\vec{H}}$) for a single sweep between 500 and -500 Oe. The peaks are attributed to a change of the spin configuration between different regimes. Figure (a) displays the derivative of the SQUID measurement. The change from the onion state (B) to the vortex state (C) is indicated by the peak at ≈ -25 Oe. The second peak at ≈ -100 Oe can possibly be attributed to a change from the vortex (C) to the vortex-core state. The inset (b) displays the change of the magnetization configuration determined by OOMMF simulation on a single structure. In contrast to the experimentally obtained curve, which is smeared out by the ensemble measurement, the calculated peaks between the regimes are sharp and well defined. The peaks between the onion (B) and vortex state (C) and between the vortex (C) and vortex-core (D) appear almost at the same field.

uration (Point C). The configuration is stable up to a field of 100 Oe. This behavior is similar to the recored minor loop (Fig. 5.6 (a)). A difference between the recorded and simulated magnetization loop is clearly observable at the transition between the global vortex (C) and the vortex-core state (D). At the recorded magnetization loop, the calculated configuration of X did not appear, i.e., the recorded loop exhibits a higher magnetization gradient between the global vortex and the local vortex configuration.

The derivatives of the magnetization isotherm loops clearly display the

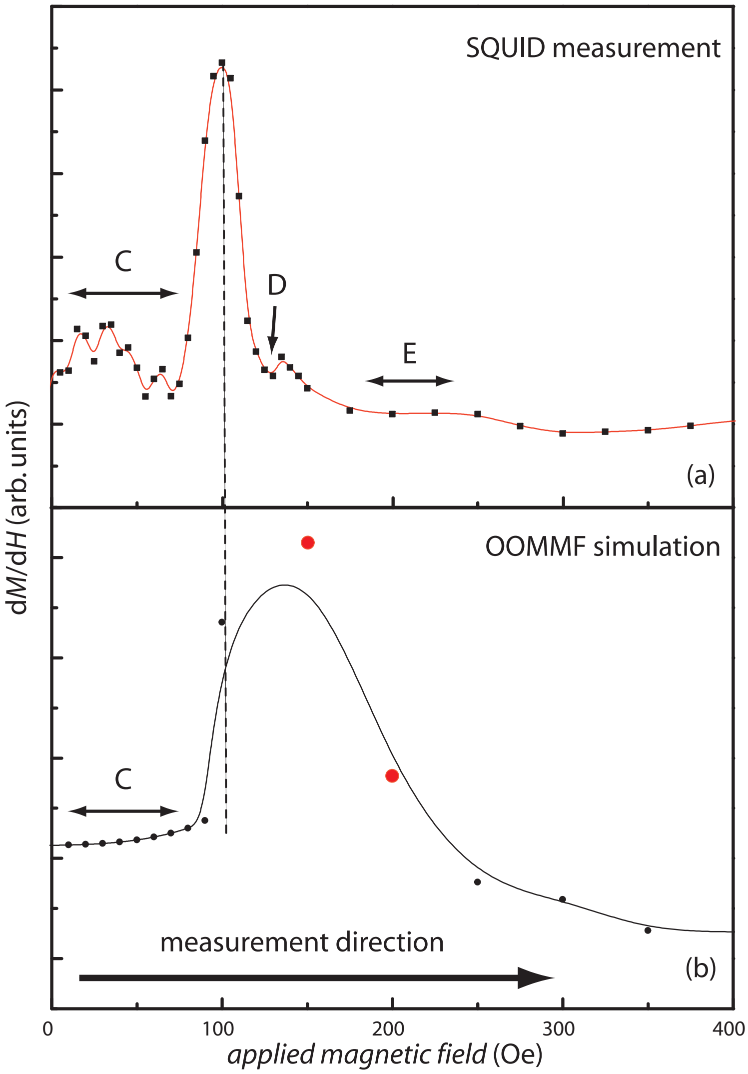

Figure 5.8: The derivative of the magnetization ($\frac{\mathrm{d}M}{\mathrm{d}\vec{H}}$) for a single sweep between -40 Oe and 500 Oe. Figure (a) displays the recorded minor loop, which exhibits the transition between global vortex (C) and vortex-core (D) configuration indicated by the peak at 100 Oe and the transition to the reversed onion state (E) at ≈ 125 Oe. The calculated derivative (b) is characterized by an broad transition peak at 150 Oe. It can be attributed to an incorrectly determined spin configuration, revealed by the vortex/transverse domain wall.

difference between the recorded and calculated loops. The transition from the global vortex (C) to the a local vortex state (D) is observable during the recorded loop, indicated by the sharp peak at $\approx$ 100 Oe (Fig. 5.8 (a)). The second peak indicates the transition between the local vortex (D) and the reversed onion state (E). The derivative of the calculated loop (Fig. 5.8 (b)) is characterized by a broad peak at $\approx$ 150 Oe. This peak describes the transitions between the vortex and local vortex and a transition to the reverse onion state. The two red circles in the lower panel belong to the calculated vortex-core state, which is characterized by a vortex/transverse domain-wall configuration. The broadening of the peak can be treated as an evidence for an unphysical calculated domain wall configuration. Only imaging methods, like MFM or PEEM, can reveal if the calculated domain configuration is realistic. The investigated spin configurations are in agreement to the properties reported in the literature. Moore et al. [77, 78] investigated by single objects measurement the magnetic properties of Permalloy submicron rings with a comparable size and thickness. Their measurements reveal an onion to vortex transition almost at zero field and in contrast to our investigations, a vortex-core state was not experimentally observed. In contrast to earlier investigation [35], we were able to determine the magnetic configuration evoked by the structuring at room temperature and not only at low temperatures. This was achieved by further synthesis improvements, such as the use of a special substrate material. In order to observe experimentally all states generated by OOMMF, one would need a better signal to noise ratio. This could achieved by an increased quantity of ferromagnetic elements written on the substrate. The main disadvantage of e-beam lithography is that this technique is extremely time consuming. Others lithography techniques, such as zone-plate [79] and, interference lithography [80] are able to fabricate long range ordered magnetic nanostructures up to a cm range. Using this techniques would improve the determination of the magnetization configuration by ensemble measurements, as used in this investigation.

5.2 Arranged magnetic dots

The drawbacks of the synthesis method presented in the previous section can be avoided by using an alternative approach based on template synthesis. Several routes for templates ordered on a long-range are described in literature [15]. The investigated structures can be apprehended as magnetic islands or dots having a hexagonal arrangement. Due to the small distance between the elements one expects that they will be affected by the interaction between neighbors.

The template for the investigated samples was prepared by the Glancing Angle Deposition (GLAD) technique on a prestructured substrate.

The prestructuring was achieved by using the nanosphere lithography (NSL) technique [81]. A monolayer of polystyrene nanospheres was deposited on a Si substrate. By self-ordering the spaces between the spheres are arranged in a hexagonal configuration. A 5 nm thick Au film was deposited onto the substrate by thermal evaporation. After removal of the spheres, the deposited material exhibits a triangular shape in a hexagonal arrangement. These triangles are an artificial seed for the subsequent GLAD deposition.

GLAD is a physical vapor deposition method based on self-shadowing effects at the substrate under oblique particle incidence circumstances. In combination with a suitable substrate rotation, it allows for the growth of nearly arbitrarily shaped nanostructures in a simple bottom-up deposition process [82, 83, 84].

These GLAD templates were prepared by Dr. Christian Patzig[3] and a detailed description about the GLAD deposition on prestructured templates is given in Ref. [85]. The honeycomb structure used is made out of Si on a Si substrate, displayed in Fig. 5.9.

In the next step, a 15 nm thin Permalloy film was deposited on top of the GLAD structure by thermal evaporation, finally a 4 nm thick film of Au was deposited by e-beam evaporation to protect the magnetic layer against oxidation. The parameters for the deposition steps are displayed in the appendix (D.3). These magnetic structures can be apprehend as an arranged array of magnetic dots.

---

[3] Leibniz Institute for Surface Modifications, Leipzig

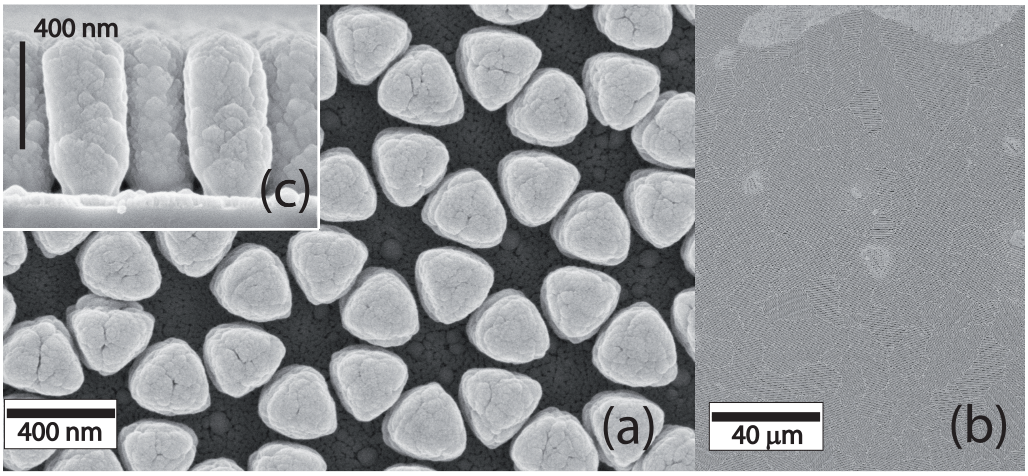

Figure 5.9: Si honeycomb structure deposited on a Si substrate by the GLAD technique. SEM micrographs (a,b) display the top view of the Si columns with different magnifications. Graph (c) depicts the height of the columns.

5.2.1 Magnetic measurements

A first magnetic characterization was performed by SQUID magnetometry. A magnetization isotherm at 300 K is displayed in Fig. 5.10. The measurement with a magnetic field applied between the magnetic elements reveals a squareness of 70 % and a coercive field of 40 Oe. The obtained curve exhibits a narrowing in the low-field regime, this behavior can be an indication for the apperance of a flux-closed state. A similar behavior was described by [12] for circular Permalloy dots with a comparable size and thickness. For the investigated sample SQUID magnetometry did not allow for angle dependent magnetization measurements using the rotatable sample holder (described in Sec. 3.3.1), due to the very weak magnetic moment of the sample compared to the background of the sample holder. In order to investigate the angle dependent in-plane magnetic behavior, magnetization isotherms were recorded over a range of ± 165° using an increment of 1° by employing the longitudinal Kerr effect. From the recordings the angle dependent coercive field was extracted. The obtained curve, displayed in Fig. 5.11, exhibits a recurring shape, with minimum in the coercive field every 60°. These measurements reveal that an angle of 30° separates the easy and hard axes. Obviously, this behavior reflects the geometric shape of the top side of the honeycomb structure. The artefacts of the curve are caused by the low long-range ordering of the sample, as displayed in Fig. 5.9 (b). During the angular dependent measurement the laser spot crosses the boundaries between domains which were slightly tilted to each other.

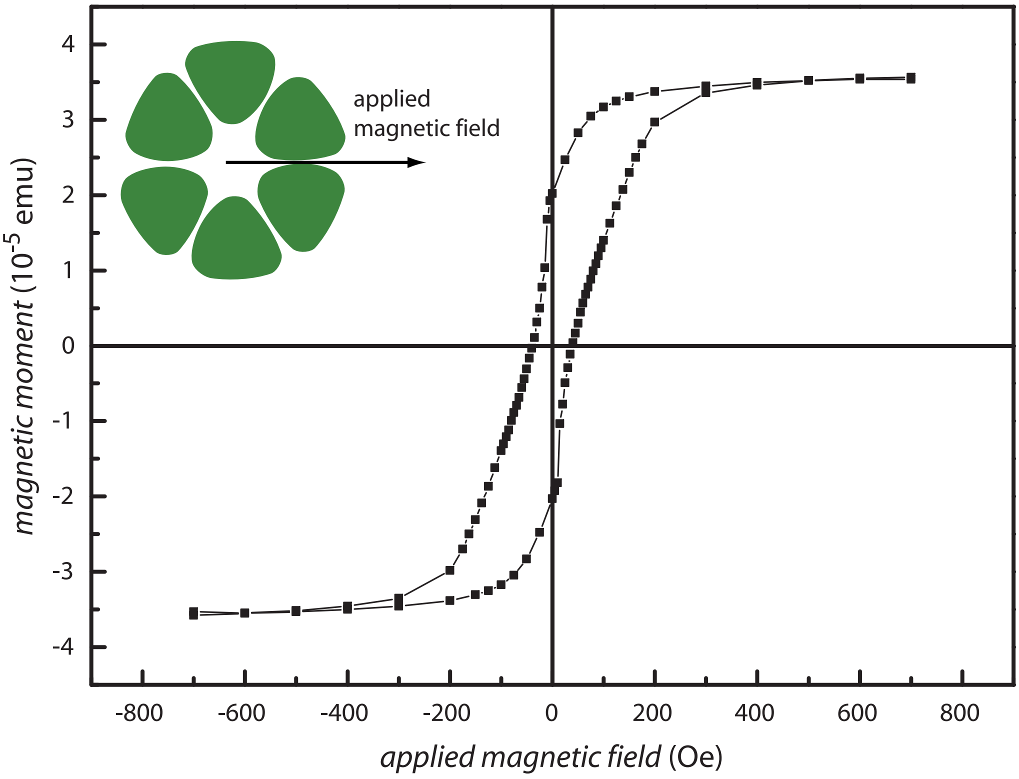

Figure 5.10: Magnetization isotherm performed at 300 K with an applied magnetic field in-plane of the substrate between ± 700 Oe. The coercive field is about 40 Oe and the squareness 70 %. The narrowing of the curve in the low field regime is an indication for the appearance of a flux close vortex state.

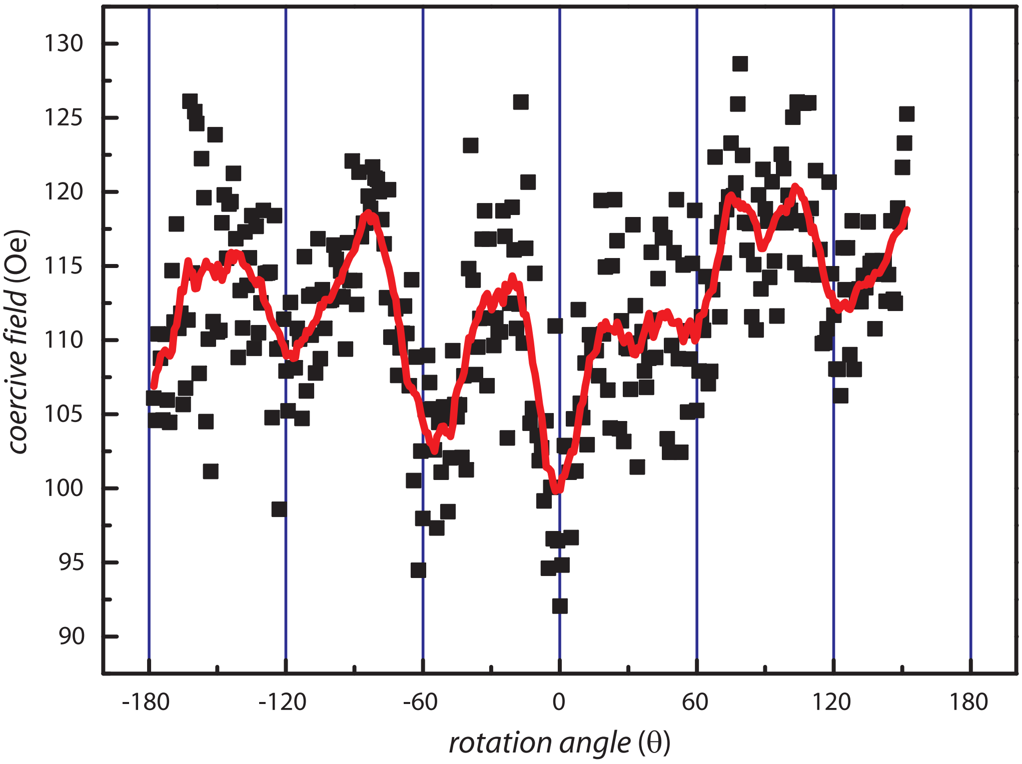

Figure 5.11: Angular dependence of the coercive field of the arranged Py dots sample, extracted from MOKE magnetization isotherms at room temperature. This dependence reflects the shape of the sample, a minimum appears every 60°.

5.2.2 Micromagnetic calculations

Micromagnetic simulation were performed to identify the origin of the observed behavior. Using the micromagnetic simulation framework *OOMMF* (described above), calculations for magnetization isotherms at two prominent configurations were performed. Both configurations ($\vec{\mathrm{H}}, \| \ \Delta\theta = 30°$) are defined in Fig. 5.12. To include the interaction between the circular arranged structures during the calculations, the region of interest (inside of the red box) is surrounded by the recurring ones, as displayed in Fig. 5.12. The calculations start with a saturated state (1000 Oe) of the sample followed by a step wise decreasing of the applied field down to -1000 Oe.

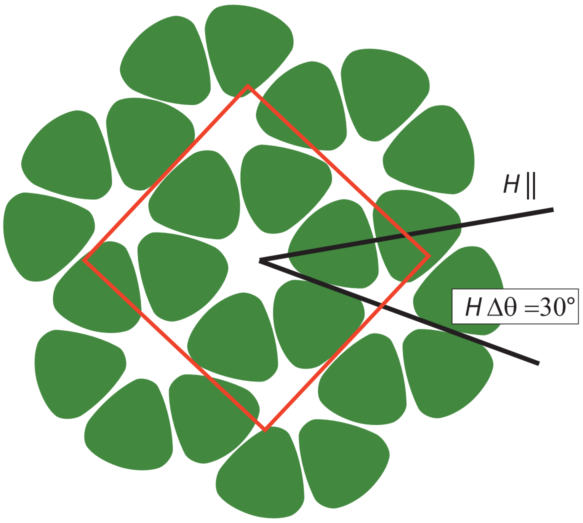

Figure 5.12: The schematic drawing depicts the structures used for the micromagnetic calculation. To include the interaction between the arranged super lattice of magnetic dots the used structure is extended by the surrounding dots. The region-of-interest is defined by the rectangular outline.

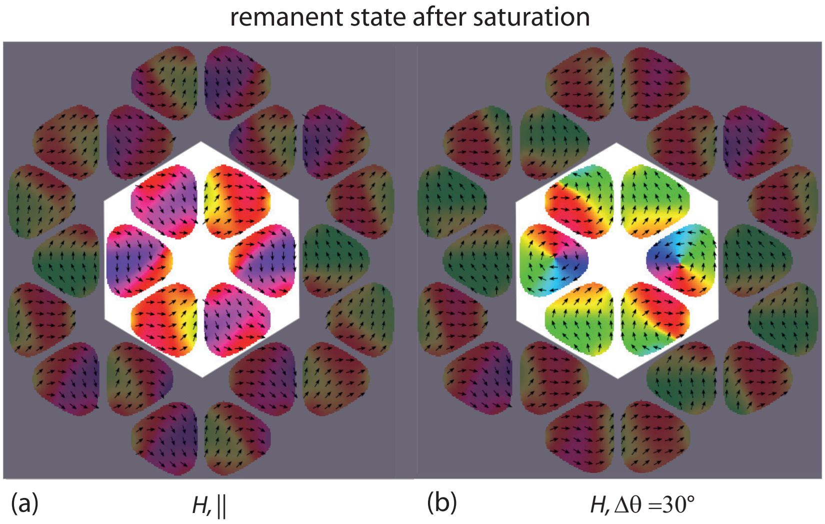

Figure 5.13: Calculated remanent state for two different configurations ($\vec{H}, \parallel \Delta\theta = 30°$), as defined in 5.12. The configuration with an applied field between the dots displays a vortex state in two magnetic dots. Both calculations exhibit the interaction between the magnetic dots. The gray shadowed masks cover the super lattice, which is taken into account to consider the interaction between the magnetic elements during the calculations.

Figure 5.13 displays a snapshot of the calculated spin configuration at the remanent state for both configurations. The $\Delta\theta = 30°$ configuration exhibits flux-closed vortex states inside of two magnetic dots. This feature is not provided by the calculation for the $\vec{H}\parallel$ configuration.

From the obtained spin configuration, as displayed in Fig. 5.13, magnetization isotherms can be extracted. For this, the directions of all magnetic moments in the region-of-interest (Fig. 5.13, highlighted area) are summed for each field step. The results are plotted in Fig. 5.14.

This calculations reveal values of the coercive field and remanent magnetizations comparable to the SQUID measurement, additionally the shape of the curve is reproduced. The narrowing of the magnetization isotherms can be attributed to the local vortex states in certain parts of the structures, as displayed in Fig. 5.13. The derivatives of the recorded and calculated magnetization isotherms reveal a similar behavior with a peak at almost 0 Oe. The calculations reveal a second peak at ≈ 400 Oe (Fig. 5.14 (b, II)) which is not observable in the recorded measurement.

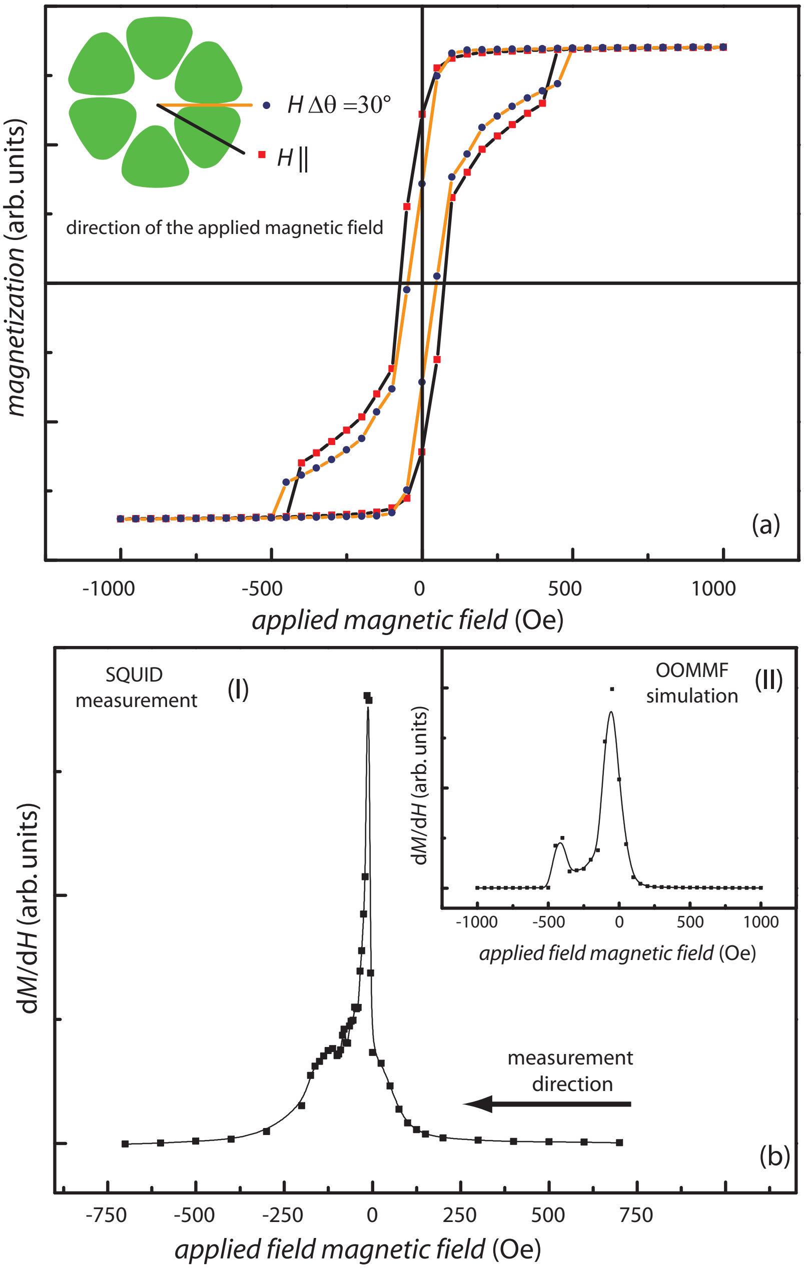

Figure 5.14: (a) Calculated magnetization isotherms for two different configurations. The calculations for an applied field trough the center of a magnetic dot ($\vec{H}, \|$) exhibit a coercive field of 76 Oe and a squareness of 72 %. The calculations of an applied field under an angle of $\vec{H}, \Delta\theta = 30°$ reveal a reduced coercive field of 46 Oe and a squareness of 42 %. This can be attributed to the appearance of vortices inside of certain magnetic dots. (b) The derivative of the magnetization ($\frac{\mathrm{d}M}{\mathrm{d}\vec{H}}$) for a single sweep between 750 Oe and -750 Oe. (I) displays the derivative of the experimentally obtained curve, shown in Fig. 5.10. The calculated curve (II) displays the first peak at the same applied field, as the measured one. The second peak at $\approx$ 400 Oe is not provided by the experimentally obtained curve.

In contrast to investigations on the submicron rings, the measurements reveal that the magnetic properties of the dot structures are dominated by the interaction between the magnetic elements by the magnetostatic energy and by the configuration anisotropy. The geometric influence of the honeycomb structure is clearly observable. The anisotropy contribution leads to similar results, such are described by Wang et al. [16] for Permalloy antidots with different geometrical arrangements. They observe for a honeycomb lattice a sixfold geometry and a difference between the easy and hard axis of 30°. In a former work [15], we investigated the magnetic properties of rectangular arranged permalloy and obtain a different magnetic behavior. For the investigated structure of arranged dots, the measurements reveals a comparable behavior to the hexagonal arranged antidots. For a detailed investigations on the origin of the magnetic properties additional angle dependent micromagnetic simulation should be performed. And furthermore, by using the same prestructured template, a investigation on the influence of the film thickness on the magnetic properties.

Summary

The ensemble measurements on the array of the magnetic submicron rings reveal almost the same magnetic properties, than reported investigation on single structures or by the performed micromagnetic simulations considering a single structure. For a satisfactory precise SQUID measurement of the static magnetization a lot of preparative efforts during the synthesis have to be done. This earned knowledge about the efforts can be transfered and used at the investigations of other magnetic nanostructures.

Chapter 6

Magnetic nanotubes

Highly anisotropic magnetic nanostructures offer a possibility to overcome the superparamagnetic limit of magnetic nanoparticles described in Chap. 4. A well-established approach to yield such highly anisotropic structures is the fabrication of magnetic nanowires and nanotubes. Several methods concerning the preparation of wires and their magnetic properties have been described in the literature during the last decade [86, 87, 88, 89, 90, 91, 92, 93, 94]. While wire-like structures offer two parameters that can be adjusted independently to influence the magnetic properties, namely length and radius, tubular structures allow for the variation of an additional degree of freedom, the wall thickness. This parameter enables the experimentalist to tune the geometric shape of the structure between a rolled-up thin film (tube) and a wire-like structure with an almost vanishing hollow center. This tuning directly influences the magnetic properties.

A well-known route for the fabrication of tubular nanostructures is the use of porous alumina membranes [95, 96] as templates for a subsequent covering with magnetic materials for this purpose. Beside the common use of the atomic layer deposition technique [97, 98] electrodeposition is also widely used [99, 100]. The static magnetization properties of nanotubes were mainly investigated by SQUID or VSM[1] magnetometry parallel or perpendicular to the long axis of the tube [101, 102, 31, 103]. Recently, the full angular range between these prominent configurations has been investigated [100].

Escrig et al. [104] presented a detailed investigation on the influence of the magnetic layer thickness in arrays of nanotubes to the reversal mode. For an applied magnetic field parallel to the long axis of the tubes, they discovered

---

[1] VSM: vibrating sample magnetometer

a transition between two reversal modes that depends on the material and the geometrical parameters.

Allende et al. [105] theoretically predicted a non-monotonic behavior of the angular dependent coercive field in a magnetic nanotube and explain this feature by a transition of reversal modes. The analytical calculations suggest that a transition should occur between the vortex and transverse reversal modes at a specific angle between the long axis of the tube and the applied magnetic field. Sharif et al. [100] observed a non-monotonic angular dependence of the coercive field in ferromagnetic tubes and interpreted it as a transition between two modes. In the present work, an alternative synthesis approach, different from the well-established combination of porous alumina membrane templates and ALD, is presented for the fabrication of tubular magnetic nanostructures. We have performed ALD on a sculptured thin film (STF) of Si prepared by glancing angle deposition (GLAD). This complementary combination overcomes several restrictions of the porous alumina template which presently is commonly used for the preparation of magnetic nanotubes. In particular, GLAD can be utilized to sculpt more complex tubular nanostructures, such as kinked ones involving one or several adjustable angles between adjacent segments.

6.1 Preparation

The deposition of inclined and upright vertical columnar structures was realized by means of ion beam sputter GLAD of Si, with a deposition setup described elsewhere [106, 107]. This deposition was done by Dr. Christian Patzig[2]. A scheme of this technique is displayed in the left part of Fig. 6.1. On Si (100) substrates (size approximately 1 cm × 1 cm), columnar Si structures were grown under a deposition angle $\theta \approx 85°$. For the growth of inclined columns, a “swing rotation” deposition scheme [108] was used in order to minimize a lateral broadening of the structures in a direction perpendicular to the plane of particle incidence. The column inclination angle β (with respect to the substrate normal) is approximately $\beta = (57 \pm 2)°$ for this sample, whereas the height of the sculptured thin film amounts to (800 ± 100) nm. To deposit a second STF sample comprising inclined columns with a different inclination angle β, a “three-phase” substrate ro-

---

[2] Leibniz Institute of Surface Modification, Leipzig

tation approach as described in Ref. [107] was used. For this sample, an inclination angle $\beta = (47 \pm 2)^\circ$ evolved, whereas the STF height accumulated to approximately (600 ± 100) nm. Additionally, using a rapid continuous substrate rotation of 0.2 rev/min, STFs comprising upright, vertical columnar Si structures were deposited ($\beta = (0 \pm 2)^\circ$), with a film height of approximately (520 ± 100) nm. Figs. 6.2 (a), (b) and (c) show SEM micrographs of all three samples prepared by GLAD. Further information on glancing angle deposition of Si by ion beam sputtering can be found in Refs. [109, 110, 111].

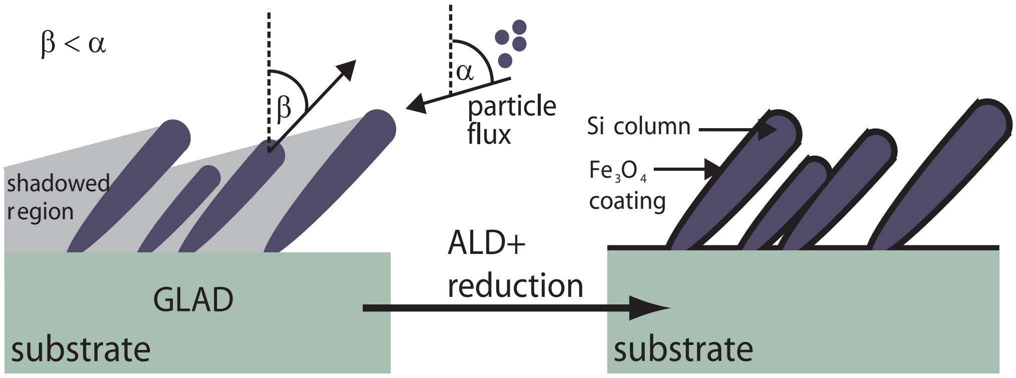

Figure 6.1: Illustration of the combination of GLAD with ALD. Left: the growth of inclined columnar (Si) structures as a result of the oblique angle deposition conditions. α is the deposition angle, and β is the column inclination angle (with respect to the substrate normal). Right: After ALD and subsequent reduction step, the (Si) columns are conformal covered with Fe_3O_4.

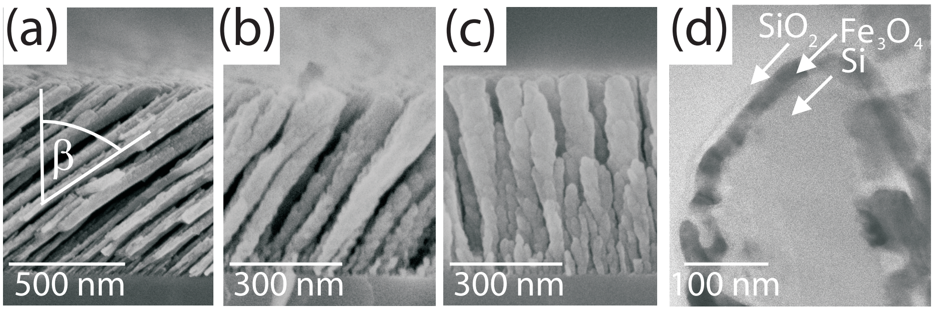

Figure 6.2: SEM micrographs of inclined Si columns as mechanically supporting structure (a to c) with different inclination angles with respect to the substrate normal (a) $\beta = (57 \pm 2)°$, (b) $\beta = (47 \pm 2)°$, (c) $\beta = (0 \pm 2)°$, fabricated by glancing angle deposition. The TEM bright-field micrograph (d) of the top of a GLAD-grown Si structure after ALD indicates the conformal coverage of the Si template with 20 nm Fe_3O_4 and 5 nm SiO_2. For the sample in (d) the parameters of the ALD coverage of Fe_3O_4/SiO_2 were the same as for all other samples.

sample no.	inclination angle (°)	length (nm)	∅diameter (nm)
1	0±2	500	75
2	47±2	825	86
3	57±2	1400	50

Table 6.1: Geometric parameters of all three investigated GLAD columns.

Atomic layer deposition is then used to coat the Si columns conformally with a 10 nm thick layer of magnetic material. In contrast to the situation of most techniques for the deposition of thin solid films from the gas phase, the deposition rate in ALD is not limited by mass transport of gaseous species (ions, atoms, or molecules) to the surface. Instead, the method relies on a well-defined chemical reaction between two or more molecular precursors at the surface to control the growth of the film [97]. The precursors must be thermally stable at the working temperature and very reactive towards one another. The substrate to be coated is exposed consecutively to vapors of the various precursors — in this manner, reactions between precursors are prevented in the gas phase. On the solid surface, however, each exposure to a precursor leads to the chemisorption of one full monolayer of it, after which

the surface is saturated and unreactive. Therefore, each repetition of the cycle of consecutive exposures results in the addition of a constant thickness of material, independent of the experimental parameters temperature and pressures (within a certain window of those parameters). This self-limiting feature of the surface chemical reaction results in conformal depositions onto non-planar substrates, making ALD the method of choice for coating highly complex templates, such as the GLAD columns used here [98].
We recently established the methodology for creating arrayed tubular magnetic nanostructures based on iron oxide from the ALD precursors ferrocene and ozone [104] in a *Cambridge Nanotech Savannah 100* ALD reactor at 200 °C substrate temperature. The organometallic precursor was heated up to 100 °C, whereas the oxygen/ozone mixture was generated in an ozone generator of *OzoneLab* ^{TM} from pure oxygen at room temperature as source (inlet pressure of 0.5 bar). To achieve a homogeneous deposition of the whole Si STF down to the substrate-near region of the columns, the sample was exposed for 30 s to each precursor, after a 2 s pulse of ferrocene and a 0.2 s pulse of the ozone mixture. The pumping time to remove all by-products and non-reacted precursor materials was set to be at least 35 s in all cases. During the whole deposition a constant nitrogen purge flow of 40 sccm was set. After a subsequent reduction step, which is described later in detail, transmission electron micrographs show a distinct Fe_3O_4 layer of constant thickness covering the Si-GLAD column (Fig. 6.2 (d)).

A protective layer is also necessary to prevent aerobic re-oxidation of the ferrimagnetic Fe_3O_4. For this purpose, a novel ALD reaction for SiO_2 [112] is used.

A 5 nm layer of silica, respectively 80 cycles, is found to be a sufficient protective layer against aerobic oxidation. Using an annealing step at 400 °C in an argon (95%)/hydrogen(5%)-atmosphere, the Fe_2O_3 was finally reduced to ferrimagnetic iron (II, III)-oxide (Fe_3O_4) through the silica layer. The results are convincing from a magnetic viewpoint: The magnetic properties of the samples kept in air remain unchanged over periods of several months. The parameter for both ALD-processes are displayed in D.5.

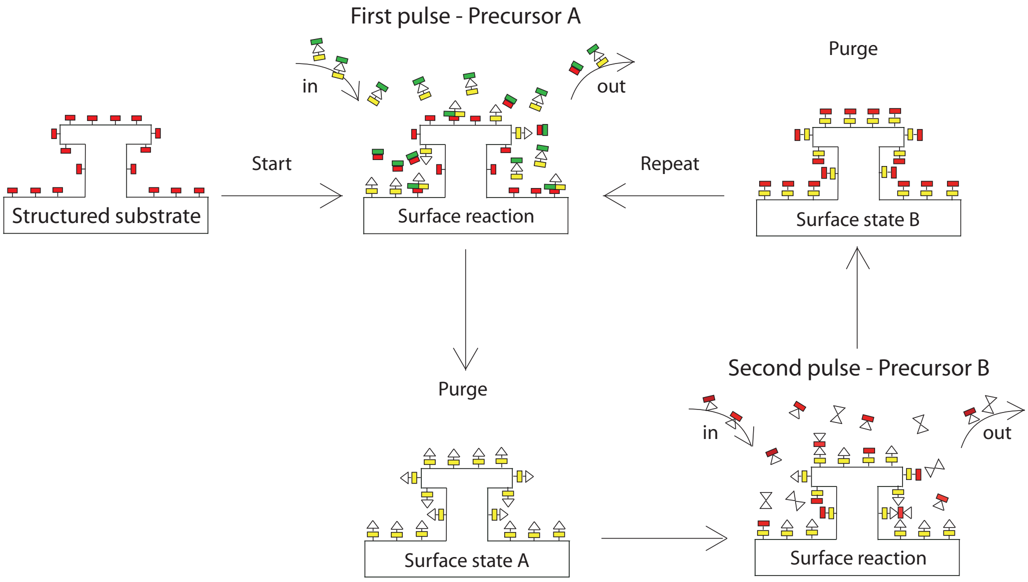

Figure 6.3: Simplified illustration of an ideal ALD process (Fig. similar to [Geo96]). Starting with a pulse of the precursor A the substrate is exposed to that reactant and a self-limiting, irreversible gas-solid reaction takes place at the substrate surface. During a pumping and purging step the non-reacted precursor A and the by-products of the surface reaction are removed from the chamber. In a next step the substrate with a recent surface state A is exposed to a precursor B which reacts in a self-limiting, irreversible way with the substrate surface. Subsequently the by-products and non-used precursor molecules B are removed in a pumping and purging step. After these two gas-solid reactions the initial chemical identity of the surface has been regenerated, with addition of one layer of the desired layer. The film thickness is controlled by the number of cycles run.

6.2 Magnetic measurements

The magnetic properties of the sample with vertical columns ($\beta = (0 \pm 2)^\circ$) can be apprehend by two extreme configurations - the out-of-plane configuration ($\vec{z'}$ axis of the columns parallel to the applied field) and the in-plane configuration ($\vec{z'}$ axis of the columns perpendicular to the applied field). Magnetization isotherms at 300 K (Fig. 6.5) yield an easy axis ($H_c = 1000$ Oe) for $\vec{z'} \| \vec{H}$ and two equivalent hard axes ($H_c = 750$ Oe) for $\vec{z'} \perp \vec{H}$. An additional in-plane measurement $\Delta\delta = 90^\circ$ exhibits the same coercive field and leads to the conclusion that there is no preferred in-plane orientation. The axes $\vec{x}, \vec{y}$ are equivalent. The observed coercivity difference between the easy and hard axes is comparable to values described in literature for Fe_3O_4 nanotubes with a similar aspect ratio [101].

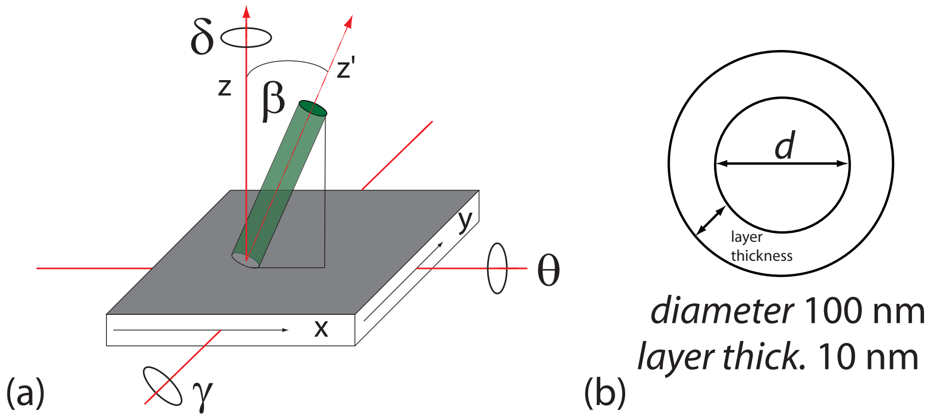

Figure 6.4: (a) Coordinate system used in the discussion: The inclination of the columns with respect to the $\vec{x} - \vec{y}$ plane of the substrate is described by the angle β. The angles γ and θ are describing the two in-plane → out-of-plane → in-plane rotations (with respect to the substrate plane). (b) Top view sketch displays the parameters of the Si core and the magnetic tube.

6.2.1 In-plane rotation

Due to the column inclination of the other samples, a more complex behavior of the angular dependent magnetization is expected. This investigations are performed by a horizontal sample rotator, described above (Sec. 3.3.1).

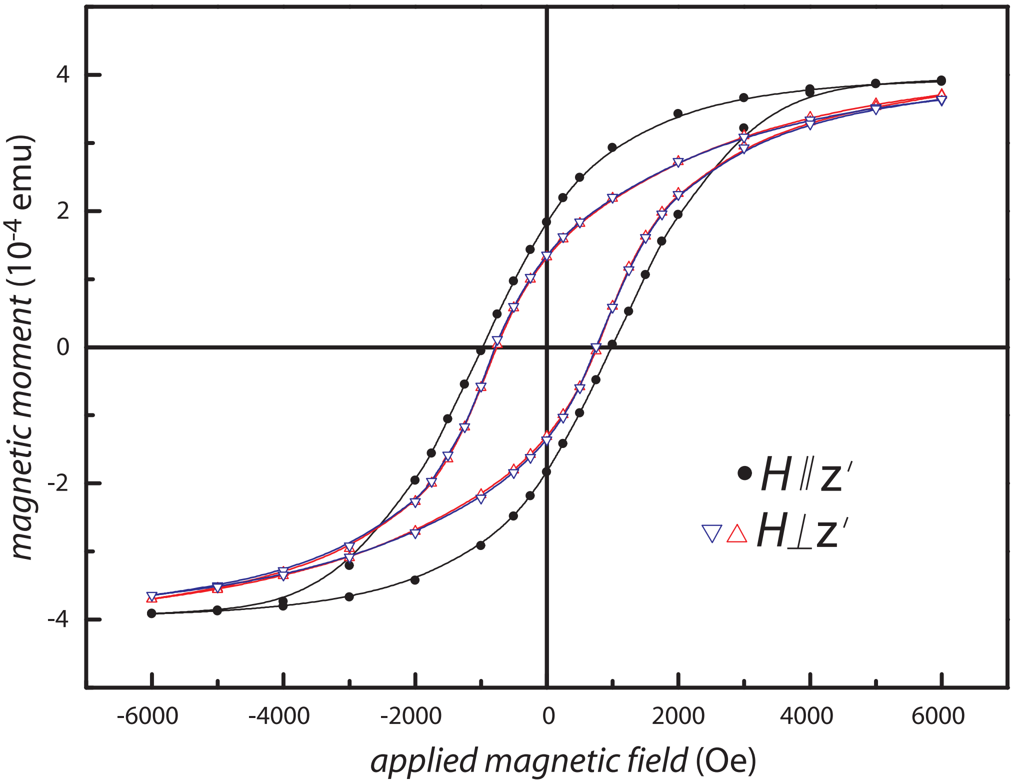

Figure 6.5: Magnetization isotherms of the sample with vertical columns ($\beta = (0 \pm 2)°$) for three different alignments: two configurations with an applied magnetic field perpendicular to the coloumn axis $\vec{z'} \perp \vec{H}$ having a different in plane rotation angle $\Delta\delta = 90°$ and one configuration with an applied field parallel to the column axis $\vec{z'} \| \vec{H}$.

For a better understanding of the angular dependence, Fig. 6.4 displays a schematic drawing of a single structure grown on its substrate. The plane of the substrate is defined by the axes $\vec{x}$ and $\vec{y}$. The $\vec{z}$ axis, being perpendicular to that plane, is defined as the rotation axis of the angle δ. The inclination of the structure with respect to the substrate normal is described by β, i.e. the angle between the surface normal $\vec{z}$ and the direction of the long axis of the tube $\vec{z'}$. The angle δ increases with a counter-clockwise substrate rotation.

If a rotation of the sample during the magnetization measurements is performed while the applied magnetic field axis $\vec{H}$ remains stationary in the plane of the substrate, the orientation behavior of the coercive field strongly depends on the angle β between the columns and the substrate normal. In this setup, the measurement starts with $\vec{H}$ aligned parallel to the sample's $\vec{y}$ axis. The substrate rotates around the rotation axis $\vec{z}$, starting at $\delta = 0°$, i.e. the long axes of the columns are aligned with the plane defined by the axes $\vec{x}$ and $\vec{z}$. After a 90° shift of δ, $\vec{H}$ is parallel to $\vec{x}$, and therefore parallel to the projection of the columns' long axis on the substrate surface as well. After another 90° shift of δ, $\vec{H}$ is finally anti-parallel to $\vec{y}$: $\vec{H} \| \vec{y} \rightarrow \vec{x} \rightarrow -\vec{y}$. As shown in Fig. 6.7, at the starting point A of the measurement ($\delta = 0°$), concerning the STF comprising inclined columns as shown in Figs. 6.6 (a) and (b), the parallel component of the columns' axis with respect to the applied field, and therefore their contribution to the coercive field, is minimal. With an increase of the rotation angle upon performing a counterclockwise substrate rotation, the parallel component of the columns with respect to the applied field increases, until a maximum of this portion is reached at point B ($\delta = 90°$). This leads to a maximum of the coercive field H_c, as can be seen in Fig. 6.7. Passing this point of maximum coercivity, the coercive field decreases again, until at point C ($\delta = 180°$), in the anti-parallel alignment of $\vec{H}$ and $\vec{y}$, the coercivity is at a minimum value again. As expected, the extent of this variation increases for a larger value of β. A control experiment with upright, vertical columnar structures as shown in Fig. 6.2 (c) ($\beta = (0 \pm 2)°$) resulted in the variation of the coercive field being close to zero within the measurement uncertainty. A top-view sketch of the measurement setup, highlighting the difference between the cases of inclined and upright columns, is shown in Fig. 6.6. The observed behavior leads to the conclusion that the tube-like ferrimagnetic $\mathrm{Fe_3O_4}$ structures that surround the columnar Si backbone exhibit the magnetic easy axis in the direction of the long axis of the tube. In contrast to this in the case of vertical columns, the coercivity H_c is angle-independent and stays approximately constant for all values of δ. In the case of inclined columns, the magnetic response of the sample shows an angular dependence, having the largest H_c values when the projection of the columnar growth direction on the substrate is aligned parallel with the direction of the external magnetic field $\vec{H}$. Figures. 6.6 (c) and (d) depict the influence of the alignment of the tube axis with the direction of $\vec{H}$ on H_c for the two extreme cases $\delta = 0°$ and $\delta = 90°$.

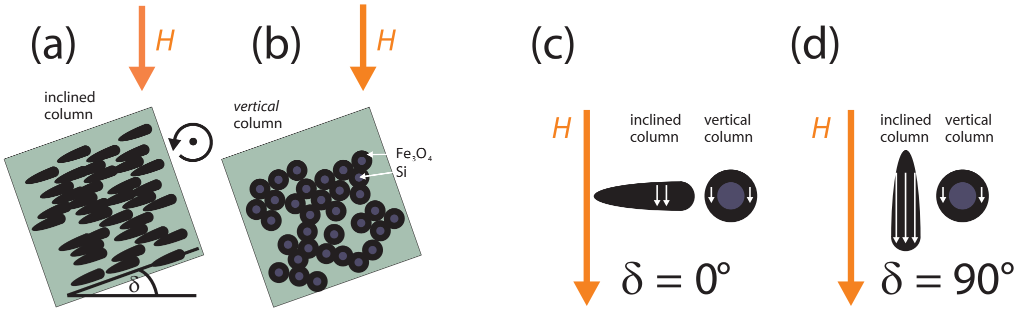

Figure 6.6: Sketch (top view) to underline the angular dependence of the coercivity H_c on the alignment of the column growth direction with the applied magnetic field $\vec{H}$ for inclined (a) and for vertical, cylindrically symmetric columns (b) if the sample is rotated with the substrate normal as rotation axis. For the case of the vertical columns, a cross-section of the columns is drawn to illustrate the difference between the Si core and the Fe_3O_4 cladding. In contrast to that, for the case of inclined columns, H_c can be expected to show a minimum, if the projection on the substrate surface of the long axis of the Fe_3O_4 tube is perpendicular to the direction of $\vec{H}$ (c) and to show a maximum at $\delta = 90°$ (d). For the vertical columns no variation of H_c on $\vec{H}$ should expected ((c), (d)).

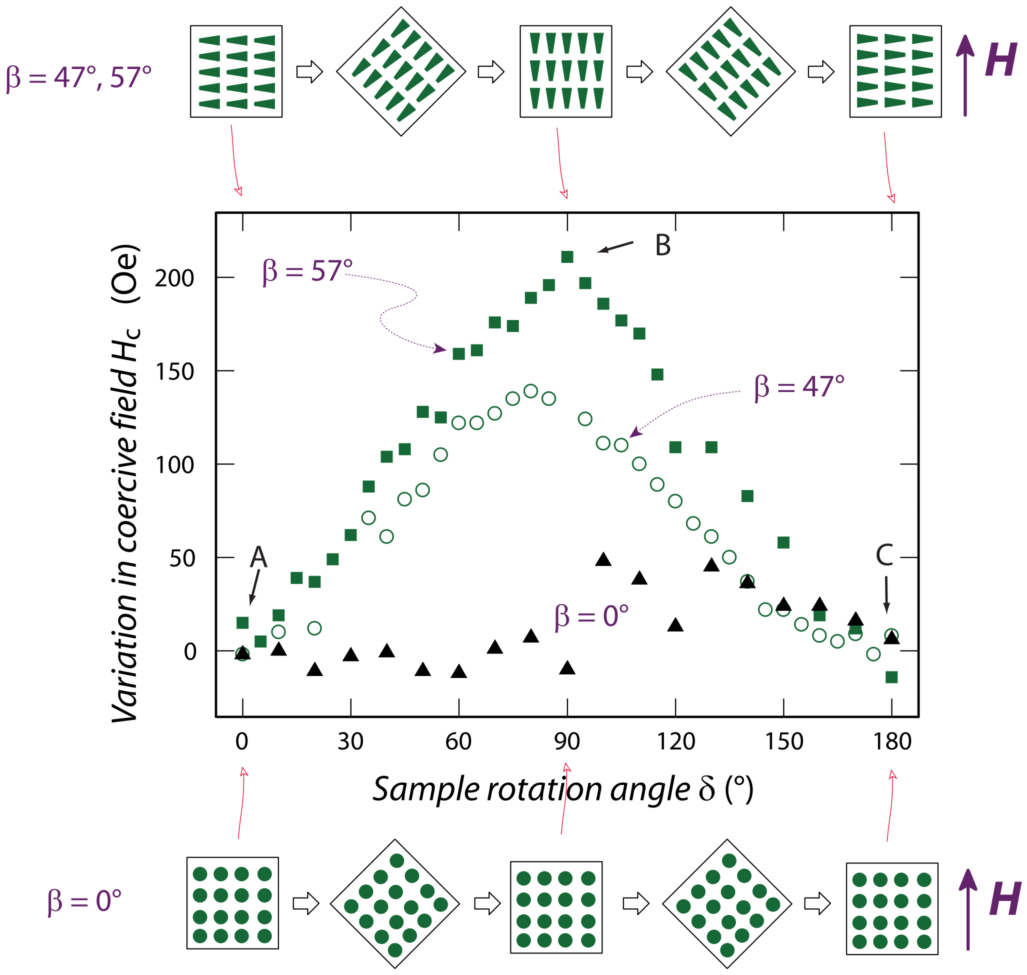

Figure 6.7: Angular dependence of the coercivity (with respect to the start value at $\delta = 0°$) for three samples with differently inclined columns $\beta = (0 \pm 2)°, \beta = (47 \pm 2)°, \beta = (57 \pm 2)°$ for a $(\vec{H} \| \vec{y} \to \vec{x} \to -\vec{y})$ rotation. The samples are rotated counterclockwise $\delta = 0° \to \delta = 180°$ with the applied magnetic field remaining in the substrate plane. This field is at $\delta = 0°$ and 180° perpendicular to the projection of the columns on the substrate and at 90° parallel to the projection.

6.2.2 In-plane → out-of-plane → in-plane rotation

For a detailed investigation of the angular dependence further measurements between two prominent configuration were performed. The rotation axis γ describes the transition between the configuration of the columnar structures parallel and perpendicular to the applied magnetic field (defined in Fig. 6.4). This was performed on the the inclined sample ($\beta = (57 \pm 2)^\circ$). Due to the inclination of the sample, the measurement was performed over a range of 180°.

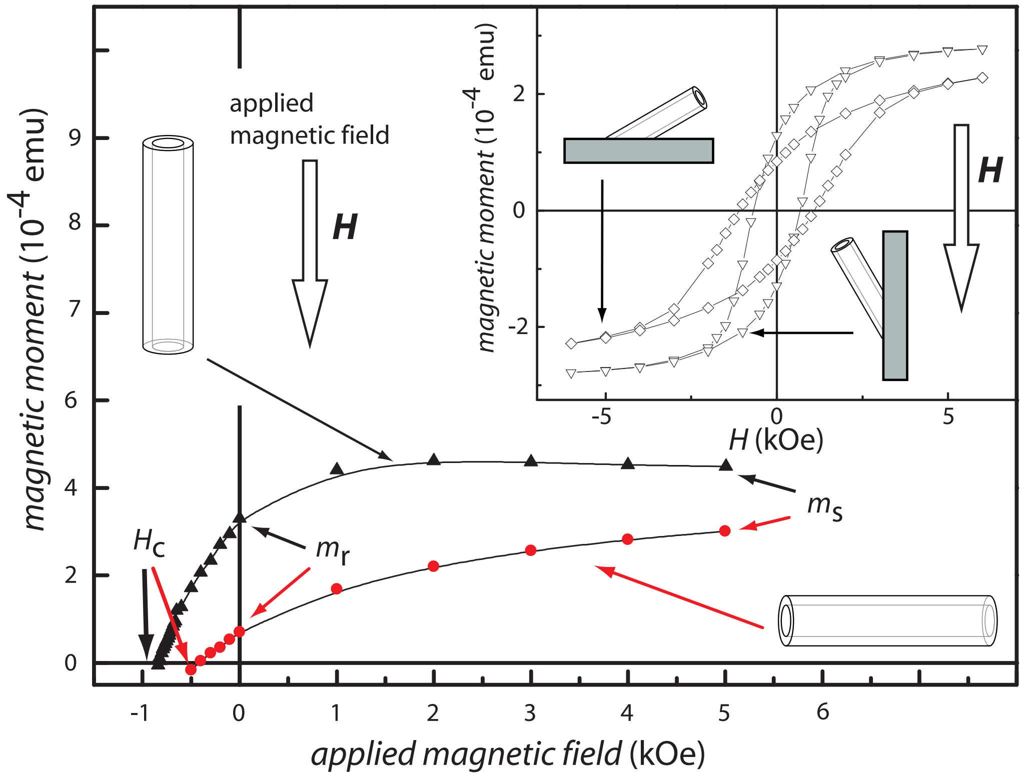

Figure 6.8: Magnified part of magnetization isotherms of two selected angles $\vec{H}\|\vec{z'}$ (▲) and $\vec{H}\perp\vec{z'}$ (●). From this recordings the angular dependent coercive H_c and squareness $SQ = m_\mathrm{r}/m_\mathrm{s}$ were extracted. For a magnetic field applied parallel to the tube the isotherm reveals a squareness of approx. 73 %. The squareness in the case of a perpendicular applied field reaches a value of 22 %. Inset: Two magnetization isotherms for a applied magnetic field a parallel (▽) or perpendicular (◇) to the substrate plane.

The resulting angle-dependent coercive field is displayed in Fig. 6.9. Starting from point A ($\gamma = 0°$), coercivity slowly rises between $\gamma = 45°$ and $\gamma = 85°$ (Point B), followed by a sharp decrease with a prominent minimum at the angle $\gamma = 125°$ (Point C). At this point, the tubes are perpendicular to the applied magnetic field $\vec{H}$, i.e. the hard axis is aligned with $\vec{H}$. By further increasing the angle γ the coercivity rises again until $\gamma = 153°$ (Point D) and decreases again. It should be noted that at points B and D substrate is oriented in different angles with respect to the applied field. The non-monotonic behavior between A and C or C and D, respectively, cannot originate from a movement of a single domain wall type as will be shown shortly.

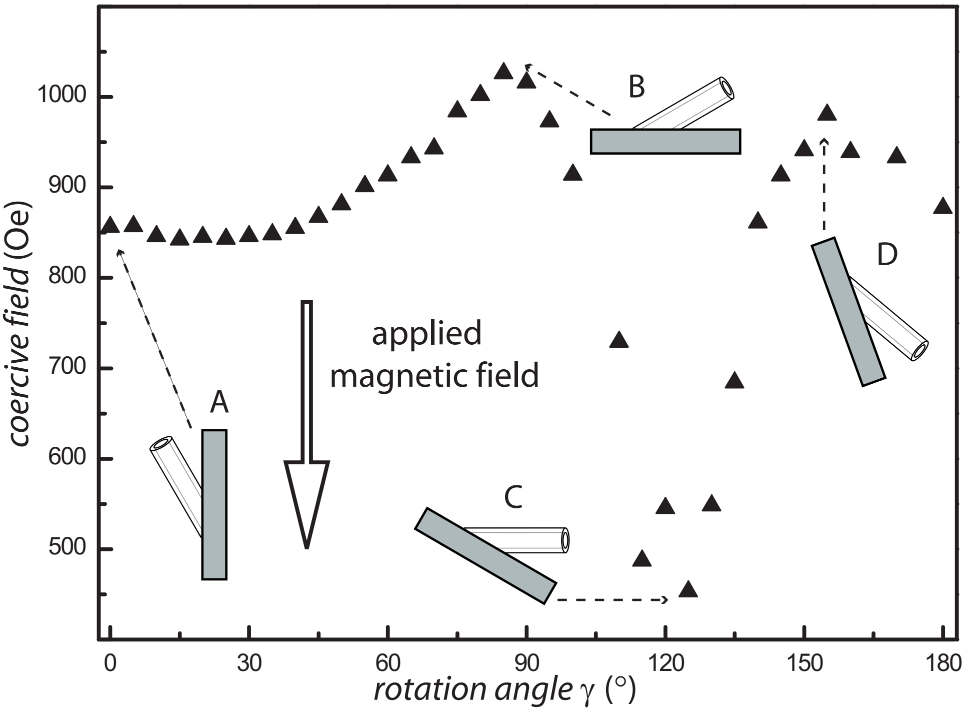

Figure 6.9: Angular dependence of the coercive field of inclined columns ($\beta = 57° \pm 2°$) for a ($\vec{H} \| \vec{x} \rightarrow \vec{z} \rightarrow -\vec{x}$) rotation by the angle γ. Point A defines the starting angle of the measurement ($\gamma = 0°$). At Point B the applied field is perpendicular to the substrate plane. At the minimum of the coercive field at $\gamma \approx 125°$ (Point C) the columns are perpendicular to the applied field.

6.3 Models of magnetization reversal in nanotubes

In magnetic nanotubes the magnetization reversal occurs mainly by the creation and motion of domain walls. As described in Sec. 2.3.1, two possible reversal mechanisms are the reversal via the propagation of a vortex or a transverse domain wall. The origin for the non-monotonic behavior of the coercivity in the range between $\vec{H}\|\vec{z'}$ and $\vec{H}\perp\vec{z'}$ observed in the investigated system can be possibly explained by a transition between different modes of magnetization reversal. Following the work of Allende et al. [105], we adapt the analytical calculations to the investigated system and also include anisotropy contributions. A third reversal mode, the coherent reversal mode which takes place without domain walls, is only favorable for short magnetic tubes where the length of the tube is in the same range as the wall width [30, 31], resulting in a negligible influence of the shape anisotropy. For this reason this mode was not taken into account in the current case of high aspect ratios. The analytical calculations allow for a determination of the nucleation field, which describes the point where the magnetization configuration starts to change in an applied reversal field, for each reversal mode (transverse and vortex). By equating the nucleation field with the coercive field, it is possible to calculate the coercivity. From the experimental point of view, it is easier to extract the coercive field from the recorded measurements and compare it to the theoretically predicted values.

6.3.1 Magnetic reversal in transverse mode

The angular dependence of a coherent magnetization reversal was considered by Stoner and Wohlfarth [34]. As described by Escrig et al. [31, 113], this model can be adapted to describe the angular dependence of a transverse magnetization reversal by replacing the length of the structure in which the coherent rotation takes place with the reduced length of the involved domain wall width w_T. This ansatz leads to the following equation for the angular dependent nucleation field:

$$H_n^T(\theta) = -\frac{1 - 3N_z(w_T) - \frac{4K_a}{\mu_0 M_0}}{2}\frac{\sqrt{1-t^2+t^4}}{1+t^2}M_0, \tag{6.1}$$

where $t = \tan^{\frac{1}{3}}(\theta)$. The angle θ describes the angle between the long axis of the tube and the applied field. $N_z(w_T)$ is demagnetizing factor within the transverse domain wall of width w_T of a tube along the $\vec{z'}$ axis taken from the work of Landeros et al. [30]. Stoner has shown [34] that the coercivity expression can be written as a function of the nucleation field as:

$$|H_c^T(\theta)| = \begin{cases} |H_n^T(\theta)| & 0 \leq \theta \leq \frac{\pi}{4} \\ 2|H_n^T\left(\frac{\pi}{4}\right)| - |H_n^T(\theta)| & \frac{\pi}{4} \leq \theta \leq \frac{\pi}{2} \end{cases}. \tag{6.2}$$

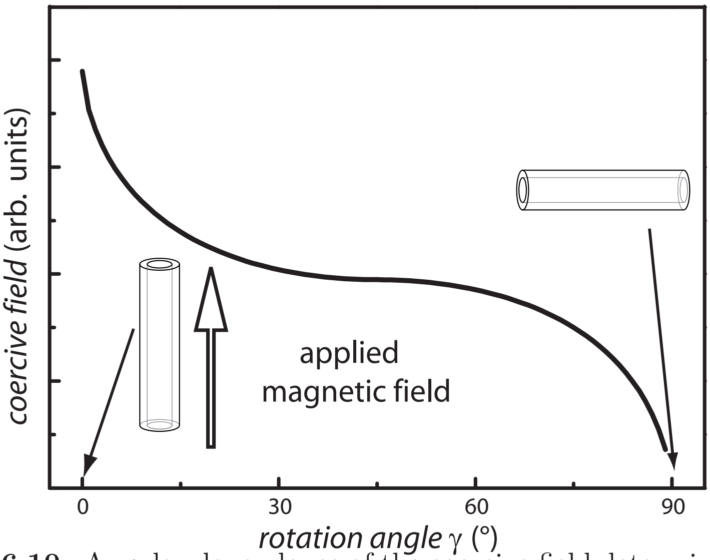

Figure 6.10: Angular dependence of the coercive field determined by analytical calculations for the transverse reversal mode between two prominent configurations. The applied field is parallel to the long axis of the tube at $\gamma = 0°$ and perpendicular to the long axis of the tube at $\gamma = 90°$. The obtained curve shows a monotonic decrease of the coercive field.

Figure 6.10 displays the angular dependence of the coercive field, described by Eq. 6.2 for a transverse reversal mode. The parameters used for the analytical calculation are similar to the parameters of the investigated structures. The obtained curve shows a monotonic decrease of the coercive field with an increasing angle.

6.3.2 Magnetic reversal in vortex mode

The angular dependence of the vortex nucleation field in a finite prolate spheroid, including the magnetocrystalline anisotropy with the constant K_α, was obtained by Aharoni [114]. Escrig et al. [113] extended the expression for the switching field to take into account the internal radii of tubes without anisotropy. Combining the ansatz of Aharoni and of Escrig leads to the following expression for the vortex nucleations field:

$$H_n^V(\theta) = \frac{(N_z - c + d)(N_x - c - d)}{\sqrt{(N_z - c + d)\sin^2\theta + (N_x - c - d)\cos^2\theta}} M_0, \tag{6.3}$$

$$\text{where } c = \frac{q^2 L_{ex}^2}{R^2}, d = \frac{2K_a}{\mu_0 M_0} \text{ and} \tag{6.4}$$

q satisfies [115]

$$\frac{qJ_0(q) - J_1(q)}{qY_0(q) - Y_1(q)} - \frac{\beta q J_0(\beta q) - J_1(\beta q)}{\beta q Y_0(\beta q) - Y_1(\beta q)} = 0. \tag{6.5}$$

Here $J_p(z)$ and $Y_p(z)$ are Bessel functions of the first and second order, respectively. L_{ex} is the exchange length of the Fe_3O_4 and R is the outer radius of the tube. Equation 6.5 has an infinite number of solutions, of which only the one with the smallest nucleation field has to be considered [6]. As pointed out by Aharoni [114], for a prolate spheroid with $\theta = 0$, a jump of the magnetization at or near the vortex nucleation field occurs. Therefore, the coercivity is quite close to the absolute value of the nucleation field. Therefore we assumed here, as in other studies [101, 114, 116] that $-H_{\text{n}}^V$ is a good approximation to the coercivity, H_{c}^V, when the reversal occurs in the V mode. This assumption is supported by the high squareness value (73 %) of the magnetization isotherm obtained for $\vec{H} \| \vec{z}$ (vortex regime), shown in Fig. 6.8.

The angular dependence of the coercive field in the vortex regime was calculated with the same parameters. As shown in Fig. 6.11, it exhibits a monotonic increase of the coercive field unlike in the transverse case. The sole consideration of each regime cannot explain the non monotonic behavior of the experimentally obtained dependence of the coercive field.

6.4 Transverse to vortex reversal transition

For the route of calculations described before, we consider a single nanotube of Fe_3O_4 with a length of 1400 nm and an inner radius r of 50 nm with a 10

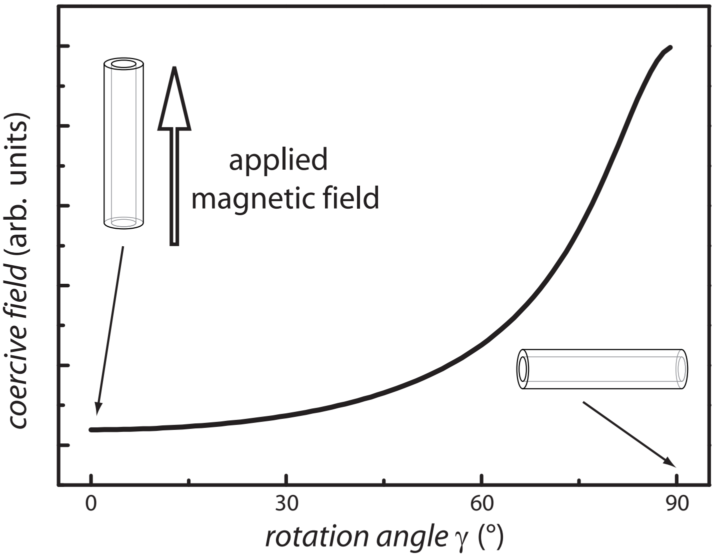

Figure 6.11: Angular dependence of the coercive field determined by analytical calculations for the vortex reversal mode between two prominent configurations. The applied field is parallel to the long axis of the tube at $\gamma = 0°$ and perpendicular to the long axis of the tube at $\gamma = 90°$. The obtained curve shows a monotonic increase of the coercive field.

nm thick layer of Fe_3O_4 at an ambient temperature with a saturation magnetization $M_0 = 4.8 \times 10^5$ Am^{-1}, an anisotropy constant $K_\mathrm{a} = -11 \times 10^3$ Jm^{-3}, and the exchange constant $A = 1 \times 10^{-11}$Jm^{-1} taken from Ref. [117].

For a direct comparison with the obtained theoretical results the experimental curve is shifted by the inclination angle $90° - \beta = 33°$. As displayed in Fig. 6.12 (a), the analytical calculations are in reasonable agreement with the experimental data. The calculation reveals a transition angle in the same range, which allows one to identify the maximum of the coercive field with a transition from a vortex to a transverse mode of magnetization reversal [31]. As shown in Fig. 6.12 (b), the transition angle between both reversal modes dependents on the tube diameter. For the investigated tubes (diameter of $\approx$ 100 nm), the slope of the curve decreases in this size regime and the transition becomes almost diameter independent.

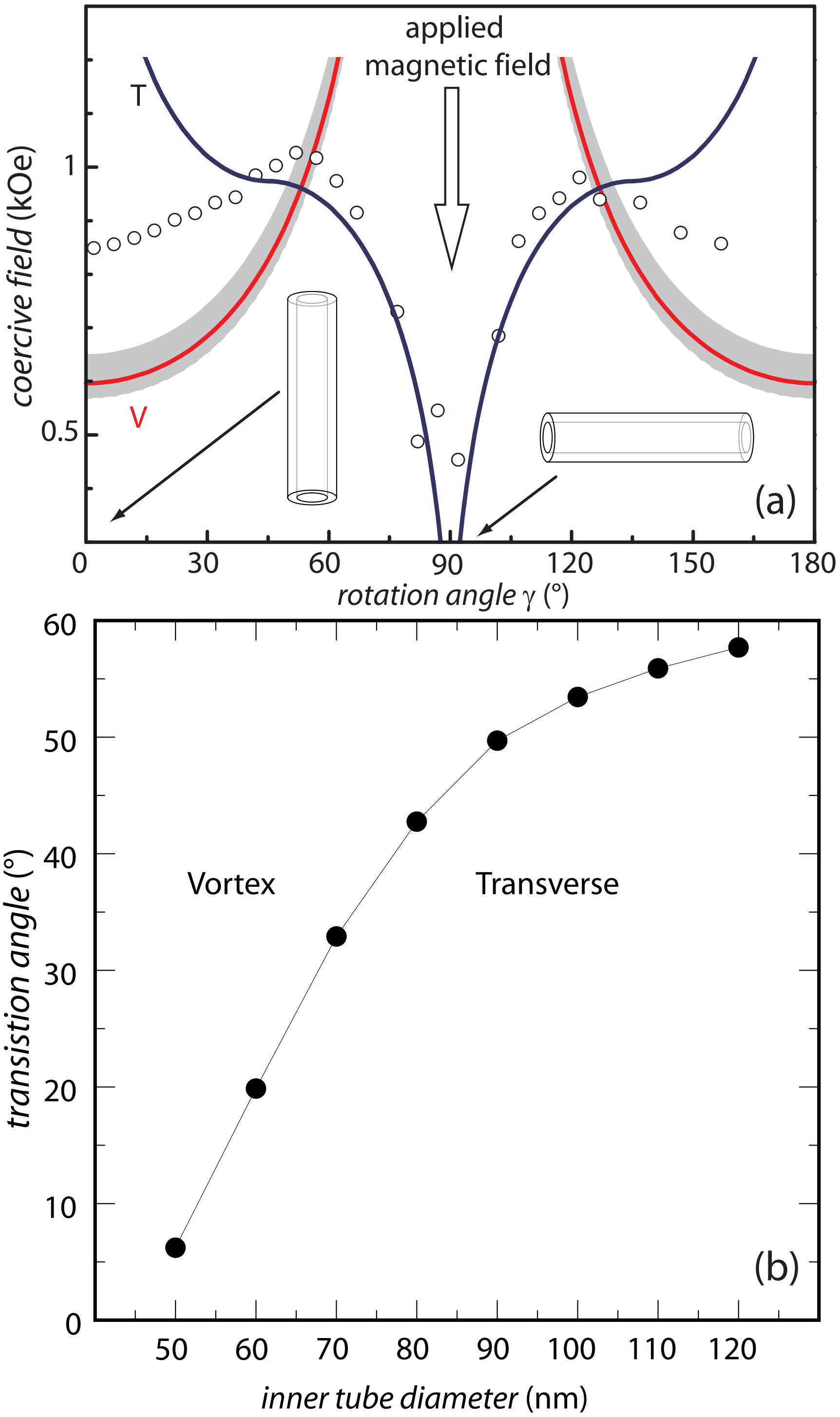

Figure 6.12: (a) Direct comparison between the experimentally determined (open circles) and the theoretically predicted (lines) angular dependence of the coercive field for Fe_3O_4 nanotubes. The experimental derived curve is shifted by the inclination angle $90° - \beta = 33°$. At $\gamma = 0°$ the tube axis $\vec{z}$ is parallel to the applied field and at $\gamma = 90°$ perpendicular. (b) Phase diagram of the diameter dependent transition angle between the vortex and transverse reversal mode, calculated for a single magnetic nanotube.

Compared to the experimentally determined coercive fields, the theoretically predicted ones are shifted to lower values. The shift is explainable by the intermixing of both states. The analytical calculations consider only pure vortex or transverse modes, in our case a fraction of the tubes may start to reverse at a low angle with the transverse mode. This intermixing increases the coercive field to higher values. As described by Allende [105], Monte-Carlo simulations take this intermixing into account, by this approach an increased value ($\approx 50\%$) of the coercive field in the vortex regime was obtained. Our measurements reveal an increased value of $\approx 25\%$ in the vortex regime. Additionally, it can possibly be explained by the diameter variations of the Si columns: In the vortex regime, the coercive field has a stronger dependence on the tube diameter. The orientation of the substrate with respect the applied field has no direct influence on the position of the transition point. As displayed in Fig. 6.9, the evolution of the curve is symmetric to point C. The slight shift of the coercive field to lower values between point B and D can be attributed to the orientation of the substrate with respect to the applied field. Performed magnetization isotherms for a 10 nm Fe_3O_4 film reveal an increased coercive field of $\approx$ 100 Oe for an applied magnetic field perpendicular to the film compared to in-plane configuration (Fig. C.1). Additionally, an angular dependent control experiment (Fig. C.2) (θ-rotation) of the inclined sample ($\beta = 57°$) reveals a monotonic increase of the coercive field up to the out-of-plane ($\theta = 90°$) configuration and a monotonic decrease down to the in-plane ($\theta = 180°$) configuration. This behavior can easily be explained by an increase and decrease of the parallel component of the long-axis of the tubes with respect to the applied magnetic field.

Shamaila et al. [118] also observed a non monotonic angular-dependent coercive field for magnetic nanotubes, but in contrast to our results, this is explained by a transition between the vortex and the *coherent* reversal mode. In their system, the observed easy axis perpendicular to the tube axis favors this transition due to the thick magnetic layer of $\approx$ 50 nm.

A complementary route for the fabrication of highly anisotropic magnetic nanostructures was established that does not rely on a porous template. The framework for these structures was built by glancing angle deposition. Subsequent atomic layer deposition yielded a conformal coverage of the columns with magnetic material. As this example shows, the combination of GLAD and ALD offers the possibility to deposit tube-like magnetic nanostructures, and their magnetic behavior can be tailored to a large extent. By angular-dependent magnetization measurements on these tubular structures we find experimental evidence for an angular dependent transition of magnetization reversal modes theoretically predicted for magnetic nanotubes. Analytical calculations allow us to identify a cusp in the experimental curve as a transition between the vortex and transverse reversal mode.

With this proof of concept for the new synthesis route we can move forward and investigate more complex structures such as the zigzag columns displayed in Fig. 6.13 (a). These columns are covered with 10 nm Fe_3O_4 using ALD as described before for the inclined samples.

We investigated the angular dependence of the coercive field for a rotation around the γ-axis. The obtained dependence is displayed in Fig. 6.13 (b). The behavior of this sample is not yet understood but it could possibly be explained by a simultaneous appearance of parallel and perpendicular contributions of the segments with respect to the applied field.

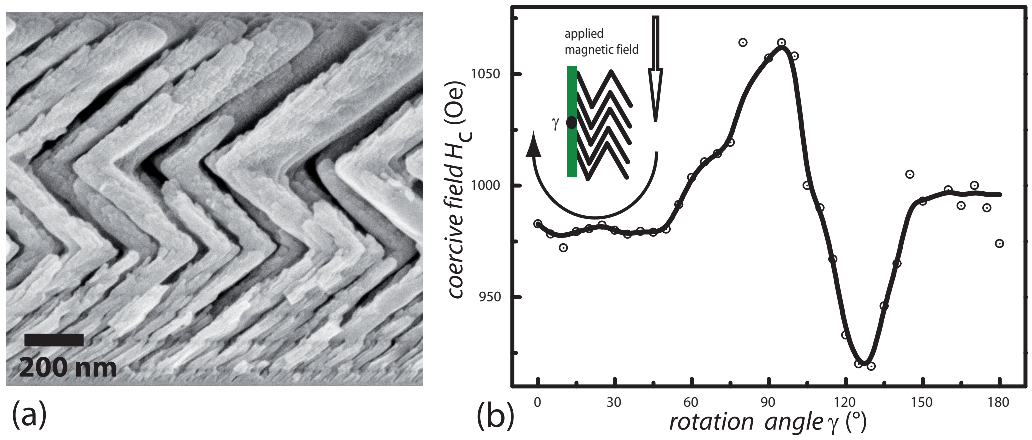

Figure 6.13: (a) SEM micrograph of a zig-zag GLAD structure made out of Si. (b) Angle-dependent coercive field for a certain rotation axis of zig-zag magnetic tubes.

Chapter 7

Summary

Various types of micro- and nanostructures with different shapes and synthesis concepts were investigated in this thesis. The magnetic properties of the samples were mainly characterized by ensemble measurements using SQUID or MOKE magnetometry.

For each NiPt, batch the static and dynamic magnetic properties of these superparamagnetic particles were determined, such as the characteristic blocking temperature, the coercive field, a mean barrier energy and a generalized anisotropy constant. However, it was not possible to determine the direct influence of shape, size and composition on the magnetic properties of the NiPt nanoparticles. The main disadvantage of the utilized synthesis approach is, that it was not possible to tune the particle parameters, such as

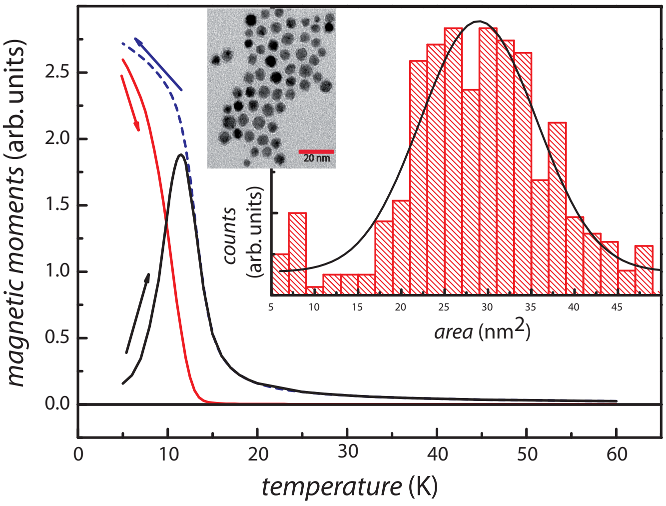

the diameter, shape and chemical composition independently. This would be a goal for further investigations. An improved synthesis method would allow for a more systematic investigation on this material system.

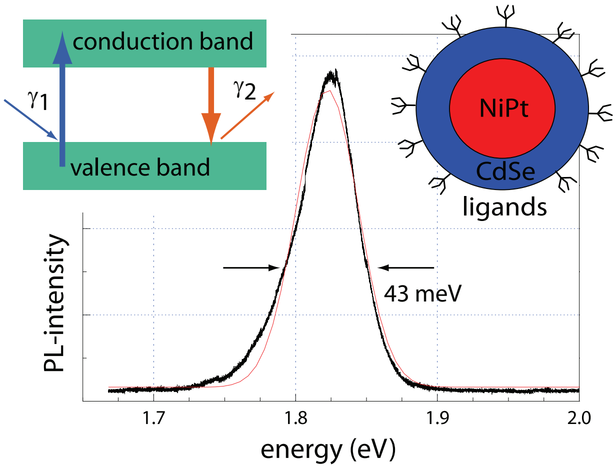

The superparamagnetic NiPt nanoparticles were covered by an additional synthesis step with a semiconducting CdSe shell. By photoluminescence spectroscopy an optical activity of the particles was revealed. Hybrid particles with two independent properties were achieved. Measurements exhibit a possible influence of the magnetic layer on the optical properties and vice versa. This material system can be used as a model system for the investigation of hybrid particles in biomedical applications.

Two possible methods for the patterning of magnetic films were then presented. By a geometrical restriction of the structures new magnetic effects appear, namely new magnetic reversal modes: the onion, vortex and vortex-core in submicron rings and local vortices in the magnetic dots structure. The effects arise as a result of the confinement of the structures in two dimensions.

Unlike to earlier investigations, the field-dependent magnetic configurations of the submicron rings were determined utilizing SQUID magnetometry at room temperature and not only at liquid He temperatures. This was achieved by additional efforts during the preparation steps. Our ensemble measurements reveal the same magnetic configurations as predicted by micromagnetic simulations and measured by single object measurements.

In contrast to the investigation on the ferromagnetic submicron rings, the magnetic properties of the ”honeycomb-arranged” magnetic dots are mainly

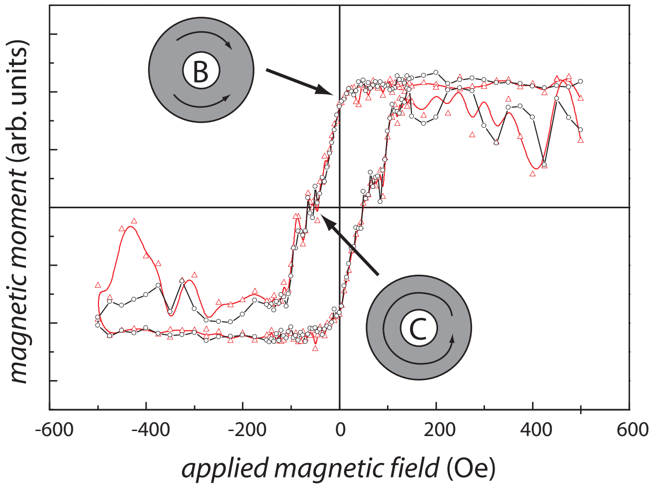

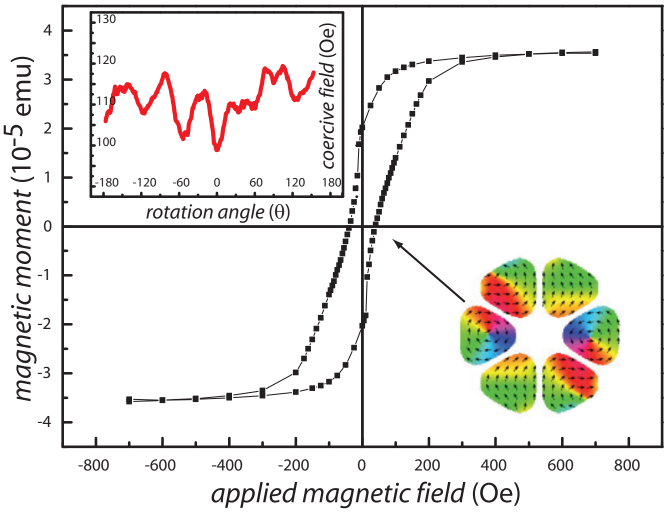

dominated by the interaction of the magnetic elements and the configuration anisotropy. Micromagnetic simulations revealed the origin of the magnetic behavior obtained. By angle-dependent MOKE measurements, the influence of the hexagonal arrangement of the dots on the magnetic properties is confirmed.

A theoretically predicted angle dependent transition between the transverse and vortex reversal for magnetic nanotubes was experimentally determined for the first time. The cusp found in the non-monotonic behavior of the angle dependent coercive field was attributed to this transition, which was confirmed by analytical calculations. The magnetic properties of all in-

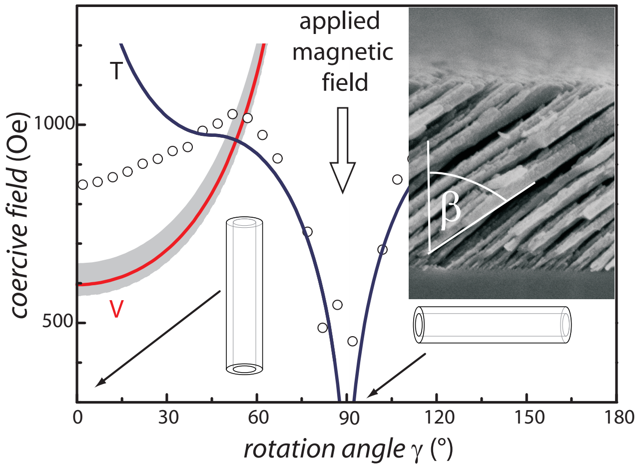

vestigated structures are dominated by the confinements and evoke effects different from the bulk, such as the appearance of superparamagnetism, specific domain wall configurations and new kinds of reversal modes between the equilibrium configurations.

Bibliography

[1] S. Sun, C. B Murray, D. Weller, L. Folks, and A. Moser. Monodisperse FePt nanoparticles and ferromagnetic FePt nanocrystal superlattices. *Science*, 287:1989, 2000.

[2] F. Wiekhorst, E. Shevchenko, H. Weller, and J. Kötzler. Anisotropic superparamagnetism of monodispersive cobalt-platinum nanocrystals. *Phys. Rev. B*, 67:224416, 2003.

[3] F. Wiekhorst, E. Shevchenko, H. Weller, and J. Kötzler. Temperature-dependent anisotropy effects on FMR and magnetization of $\mathrm{FePt_2}$ and $\mathrm{CoPt_3}$ nanocrystals. *J. Magn. Magn. Mater.*, 272:1559, 2004.

[4] M. Mandal, S. Kundu, T. K. Sau, S. M. Yusuf, and T. Pal. Synthesis and characterization of superparamagnetic Ni-Pt nanoalloy. *Chem. Mater*, 15:3710, 2003.

[5] K. Ahrenstorf, O. Albrecht, H. Heller, A. Kornowski, D. Görlitz, and H. Weller. Colloidial synthesis of $\mathrm{Ni_xPt_{1-x}}$ nanoparticles with tuneable composition. *Small*, 3:271, 2007.

[6] A. Aharoni. *Introduction to the Theory of Ferromagnetism.* Oxford University Press, 2000.

[7] N. Ashcroft and N. Mermin. *Festkörperphysik.* Oldenbourg, 2001.

[8] G. Czycholl. *Theoretische Festkörperphysik.* Springer, 2004.

[9] N. Spaldin. *Magnetic Materials: Fundamentals and Device Applications.* Cambridge University Press, 2003.

[10] C. Kittel. Physical theory of ferromagnetic domains. *Rev. Mod. Phys.*, 21:541, 1949.

[11] C. A. F. Vaz, J. A. C. Bland, and G. Lauhoff. Magnetism in ultrathin film structures. *Rep. Prog. Phys.*, 71:056501, 2008.

[12] R. P. Cowburn, D. K. Koltsov, A. O. Adeyeye, M. E. Welland, and D. M. Tricker. Single-domain circular nanomagnets. *Phys. Rev. Lett.*, 83:1042, 1999.

[13] J. Podbielski. private communication.

[14] E. Mengotti, L. J. Heyderman, F. Nolting, B. R. Craig, J. N. Chapman, L. Lopez-Diaz, R. J. Matelon, U. G. Volkmann, M. Kläui, U. Rüdiger, C. A. F. Vaz, and J. A. C. Bland. Easy axis magnetization reversal in cobalt antidot arrays. *J. Appl. Phys.*, 103:07D509, 2008.

[15] S. Martens, O. Albrecht, K. Nielsch, and D. Görlitz. Local modes and two magnon scattering in ordered permalloy antidot arrays. *J. Appl. Phys.*, 105:07C113, 2009.

[16] C. C. Wang, A. O. Adeyeye, and N. Singh. Magnetic antidot nanostructures: effect of lattice geometry. *Nanotechnology*, 17:1629, 2006.

[17] A. O. Adeyeye and N. Singh. Large area patterned magnetic nanostructures. *J. Phys. D-Appl. Phys.*, 41:153001, 2008.

[18] C. T. Yu, H. Jiang, L. Shen, P. J. Flanders, and G. J. Mankey. The magnetic anisotropy and domain structure of permalloy antidot arrays. *J. Appl. Phys.*, 87:6322, 2000.

[19] Z. L. Xiao, C. Y. Han, U. Welp, H. H. Wang, V. K. Vlasko-Vlasov, W. K. Kwok, D. J. Miller, J. M. Hiller, R. E. Cook, G. A. Willing, and G. W. Crabtree. Nickel antidot arrays on anodic alumina substrates. *Appl. Phys. Lett.*, 81:2869, 2002.

[20] F. J. Castaño, K. Nielsch, C. A. Ross, J. W. A. Robinson, and R. Krishnan. Anisotropy and magnetotransport in ordered magnetic antidot arrays. *Appl. Phys. Lett.*, 85:2872, 2004.

[21] C. A. F. Vaz, T. J. Hayward, J. Llandro, F. Schackert, D. Morecroft, J. A. C. Bland, M. Kläui, M. Laufenberg, D. Backes, U. Rudiger, F. J. Castano, C. A. Ross, L. J. Heyderman, F. Nolting, A. Locatelli, G. Faini, S. Cherifi, and W. Wernsdorfer. Ferromagnetic nanorings. *J. Phys.-Condes. Matter*, 19:255207, 2007.

[22] F. Giesen. *Magnetization Dynamics of Nanostructured Ferromagnetic Rings and Rectangular Elements.* PhD thesis, University of Hamburg, 2005.

[23] J. Podbielski. Ferromagnetische Resonanz nanostrukturierter Ringe. Master's thesis, University of Hamburg, 2004.

[24] M. H. Park, Y. K. Hong, Y. K. Choi, M. J. Donahue, H. Han, and S. H. Gee. Vortex head-to-head domain walls and their formation in onion-state ring elements. *Phys. Rev. B*, 73:094424, 2006.

[25] F. J. Castaño, C. A. Ross, C. Frandsen, A. Eilez, D. Gil, Henry I. Smith, M. Redjdal, and F. B. Humphrey. Metastable states in magnetic nanorings. *Phys. Rev. B*, 67:184425, 2003.

[26] M. Kläui. Head-to-head domain walls in magnetic nanostructures. *J. Phys.-Condes. Matter*, 20:313001, 2008.

[27] M. Kläui, C. A. F. Vaz, J. A. C. Bland, L. J. Heyderman, F. Nolting, A. Pavlovska, E. Bauer, S. Cherifi, S. Heun, and A. Locatelli. Head-to-head domain-wall phase diagram in mesoscopic ring magnets. *Appl. Phys. Lett.*, 85:5637, 2004.

[28] R.D. McMichael and M.J. Donahue. Head to head domain wall structures in thin magnetic strips. *IEEE Trans. Magn.*, 33:4167, 1997.

[29] M. Laufenberg, D. Backes, W. Bührer, D. Bedau, M. Kläui, U. Rüdiger, C. A. F. Vaz, J. A. C. Bland, L. J. Heyderman, F. Nolting, S. Cherifi, A. Locatelli, R. Belkhou, S. Heun, and E. Bauer. Observation of thermally activated domain wall transformations. *Appl. Phys. Lett.*, 88:052507, 2006.

[30] P. Landeros, S. Allende, J. Escrig, E. Salcedo, D. Altbir, and E. E. Vogel. Reversal modes in magnetic nanotubes. *Appl. Phys. Lett.*, 90:102501, 2007.

[31] J. Escrig, J. Bachmann, J. Jing, M. Daub, D. Altbir, and K. Nielsch. Crossover between two different magnetization reversal modes in arrays of iron oxide nanotubes. *Phys. Rev. B*, 77:214421, 2008.

[32] O. Albrecht, R. Zierold, S. Allende, C. Patzig, B. Rauschenbach, K. Nielsch, and D. Görlitz. Experimental evidence for an angular dependent transition of magnetization reversal modes in magnetic nanotubes. submitted, 2009.

[33] J. Escrig, S. Allende, D. Altbir, and M. Bahiana. Magnetostatic interactions between magnetic nanotubes. *Appl. Phys. Lett.*, 93:023101, 2008.

[34] E. C. Stoner and E. P. Wohlfarth. A mechanism of magnetic hysteresis in heterogeneous alloys. *Phil. Trans. R. Soc. A*, 240:599, 1948.

[35] O. Albrecht. SQUID und AC-Suszeptometrie an Nanomagneten. Master's thesis, Institute of Applied Physics, University of Hamburg, 2006.

[36] Quantum Design. *Manual MPMS/MPMS2*, 1986/1990.

[37] Quantum Design. *MPMS Application Note: Palladium Reference Sample*, 2005.

[38] D. Martien. *Introduction to AC Susceptibility.* Quantum Design.

[39] D. Jiles. *Introduction to Magnetism and Magnetic Materials.* Chapman & Hall, 1991.

[40] Durham Magnetooptics LTD. Nanomoke 2 specifications.

[41] C. P. Bean and I. S. Jacobs. Magnetic granulometry and superparamagnetism. *J. Appl. Phys.*, 27:1448, 1956.

[42] C.P. Bean and J.D. Livingston. Superparamagnetism. *J. Appl. Phys.*, 30:S120, 1959.

[43] J. Kötzler, D. Görlitz, and F. Wiekhorst. Strong spin-orbit-induced gilbert damping and g-shift in iron-platinum nanoparticles. *Phys. Rev. B*, 76:104404, 2007.

[44] E. Shevchenko, D. Talapin, A. Kornowski, F. Wiekhorst, J. Kötzler, M. Haase, A. Rogach, and H. Weller. Colloidal crystals of monodisperse FePt nanoparticles grown by a three-layer technique of controlled oversaturation. *Adv. Mat.*, 14:287, 2002.

[45] M. Grzelczak, J. Perez-Juste, B. Rodriguez-Gonzalez, M. Spasova, I. Barsukov, M. Farle, and L. M. Liz-Marzan. Pt-catalyzed growth of Ni nanoparticles in aqueous CTAB solution. *Chem. Mat.*, 20:5399, 2008.

[46] K. Ahrenstorf. *Nukleations- und Wachstumsmechanismus von* $\mathrm{Ni_xPt_{1-x}}$*-Nanopartikeln und ihre charakteristischen Eigenschaften.* PhD thesis, Institute of Physical Chemistry, University of Hamburg, 2007.

[47] C. E. Dahmani, M. C. Cadeville, J. M. Sanchez, and J. L. Morán-López. Ni-Pt phase diagram: Experiment and theory. *Phys. Rev. Lett.*, 55:1208, 1985.

[48] M. J. Besnus and A. Herr. Transition from ferromagnetism to paramagnetism in NiPt alloys. *Phys. Lett. A*, 39:83, 1972.

[49] R. E. Parra and J. W. Cable. Neutron study of magnetic-moment distribution in Ni-Pt alloys. *Phys. Rev. B*, 21:5494, 1980.

[50] M. Angelakeris, P. Poulopoulos, N. Vouroutzis, M. Nyvlt, V. Prosser, S. Visnovsky, R. Krishnan, and N. K. Flevaris. Structural and spectroscopic magneto-optic studies of Pt-Ni multilayers. *J. Appl. Phys.*, 82:5640, 1997.

[51] Sung-Chul Shin Young-Seok Kim. Role of magnetoelastic anisotropy in Ni/Pt multilayer films. *Magnetics, IEEE Transactions*, 34:858, 1998.

[52] W.S. Rasband. ImageJ: image processing program. U. S. National Institutes of Health, Bethesda, Maryland, USA,.

[53] S. H. Masunaga, R. F. Jardim, P. F. P. Fichtner, and J. Rivas. Role of dipolar interactions in a system of Ni nanoparticles studied by magnetic susceptibility measurements. *Phys. Rev. B*, 80:184428, 2009.

[54] H. Kadomatsu, T. Tokunaga, and H. Fujiwara. Magnetocrystalline anisotropy of Ni-Pt alloys. *J. Phys. Soc. Jpn.*, 50:3, 1981.

[55] S. Morup, H. Topsoe, and B.S. Clausen. Magnetic properties of microcrystals studied by mössbauer spectroscopy. *Phys. Scr.*, 25:713, 1982.

[56] V. Skumryev, S. Stoyanov, Y. Zhang, G. Hadjipanayis, D. Givord, and J. Nogues. Beating the superparamagnetic limit with exchange bias. *Nature*, 423:850, 2003.

[57] F. Woodbridge Constant. The magnetic properties of certain Pt-Co and Pd-Co alloys. *Phys. Rev.*, 36:1654, 1930.

[58] Q. A. Pankhurst, J. Connolly, S. K. Jones, and J. Dobson. Applications of magnetic nanoparticles in biomedicine. *J. Phys. D-Appl. Phys.*, 36:R167, 2003.

[59] P. Tartaj, M. del Puerto Morales, S. Veintemillas-Verdaguer, T. Gonzalez-Carreno, and C. J Serna. The preparation of magnetic nanoparticles for applications in biomedicine. *J. Phys. D-Appl. Phys.*, 36:R182, 2003.

[60] A. Quarta, R. Di Corato, L. Manna, A. Ragusa, and T. Pellegrino. Fluorescent-magnetic hybrid nanostructures: Preparation, properties, and applications in biology. *IEEE Trans. Nanobiosci.*, 6:298, 2007.

[61] T. Menke. Photolumnineszenz-Spektroskopie an chemisch synthesierten Nanopartikeln. Master's thesis, Institute of Applied Physics, University of Hamburg, 2007.

[62] D. Valerini, A. Cretí, M. Lomascolo, L. Manna, R. Cingolani, and M. Anni. Temperature dependence of the photoluminescence properties of colloidal CdSe/ZnS core/shell quantum dots embedded in a polystyrene matrix. *Phys. Rev. B*, 71:235409, 2005.

[63] G. W. Walker, V. C. Sundar, C. M. Rudzinski, A. W. Wun, M. G. Bawendi, and D. G. Nocera. Quantum-dot optical temperature probes. *Appl. Phys. Lett.*, 83:3555, 2003.

[64] J. Moritz, B. Dieny, J. P. Nozières, S. Landis, A. Lebib, and Y. Chen. Domain structure in magnetic dots prepared by nanoimprint and e-beam lithography. *J. Appl. Phys.*, 91:7314, 2002.

[65] P. M. Leufke, S. Riedel, M. Lee, J. Li, H. Rohrmann, T. Eimüller, P. Leiderer, J. Boneberg, G. Schatz, and M. Albrecht. Two different coercivity lattices in Co/Pd multilayers generated by single-pulse direct laser interference lithography. *J. Appl. Phys.*, 105:113915, 2009.

[66] J. Moritz, S. Landis, J. C. Toussaint, R. Bayle-Guillemaud, B. Rodmacq, G. Casali, A. Lebib, Y. Chen, J. P. Nozires, and B. Dieny. Patterned media made from pre-etched wafers: a promising route toward ultrahigh-density magnetic recording. *IEEE Trans. Mag.*, 38:1731, 2002.

[67] S. Landis, B. Rodmacq, B. Dieny, B. Dal'Zotto, S. Tedesco, and M. Heitzmann. Domain structure of magnetic layers deposited on patterned silicon. *Appl. Phys. Lett.*, 75:2473, 1999.

[68] J. I. Martín, J. Nogués, Kai Liu, J. L. Vicent, and Ivan K. Schuller. Ordered magnetic nanostructures: fabrication and properties. *J. Magn. Magn. Mater.*, 256:449, 2003.

[69] B. R. Pujada, B. C. Choi, M. H. Park, Y. K. Hong, S. H. Gee, H. Han, and G. W. Donohoe. Micromagnetic configurations and switching mechanism in pac-man-shaped submicron $Ni_{80}Fe_{20}$ magnets. *J. Appl. Phys.*, 97, 2005.

[70] K. Dong-Hyun, J. Jong-Ryul, C. Yoon-Chul, and S. Sung-Chul. Micromagnetic simulation of magnetization reversal behavior of Co/Pt multilayer nanodot array prepared by colloidal lithography. *J. Magn. Magn. Mater.*, 286:23, 2005.

[71] S. C. Hernandez, J. Dou, C. Yu, M. J. Pechan, L. Folks, J. A. Katine, and M. J. Carey. Exchange-coupled suppression of vortex formation in permalloy nanodot chain arrays. *J. Appl. Phys.*, 105:07C125, 2009.

[72] M. Coisson, F. Celegato, E. S. Olivetti, P. Tiberto, and F. Vinai. Analysis of magnetic domain patterns and vector hysteresis loops in dot/antidot structures. *IEEE Trans. Magn.*, 45:3511, 2009.

[73] L. J. Heyderman, C. David, M. Kläui, C. A. F. Vaz, and J. A. C. Bland. Nanoscale ferromagnetic rings fabricated by electron-beam lithography. *J. Appl. Phys.*, 93:10011, 2003.

[74] M. S. Cohen. Anisotropy in permalloy films evaporated at grazing incidence. *J. Appl. Phys.*, 32:S87, 1961.

[75] OOMMF: micromagnetic simulation package. National Institute of Standards and Technology.

[76] M. Martens. private communication.

[77] TA. Moore, TJ. Hayward, DHY. Tse, JAC. Bland, FJ. Castano, and CA. Ross. Stochastic switching in individual micrometre-sized Permalloy rings. *Physica B*, 372(1):164, 2006.

[78] TA. Moore, TJ. Hayward, DHY. Tse, JAC. Bland, FJ. Castano, and CA. Ross. Magnetization reversal in individual micrometer-sized polycrystalline Permalloy rings. *J. Appl. Phys.*, 97(6), 2005.

[79] W Jung, FJ Castano, CA Ross, R Menon, A Patel, EE Moon, and HI Smith. Elliptical-ring magnetic arrays fabricated using zone-plate-array lithography. *J. Vac. Sci. Technol. B*, 22(6):3335, 2004. 48th International Conference on Electron, Ion and Photon Beam Technology and Nanofabrication, San Diego, CA, JUN 01-04, 2004.

[80] R. Ji, W. Lee, R. Scholz, U. Goesele, and K. Nielsch. Templated fabrication of nanowire and nanoring arrays based on interference lithography and electrochemical deposition. *Adv. Mater.*, 18:2593, 2006.

[81] B. Fuhrmann, H. S. Leipner, H-R. Höche, L. Schubert, P. Werner, and U. Gösele. Ordered arrays of silicon nanowires produced by nanosphere lithography and molecular beam epitaxy. *Nano Lett.*, 5:2524, 2005.

[82] K. Robbie, M. J. Brett, and A. Lakhtakia. Chiral sculptured thin films. *Nature*, 384:616, 1996.

[83] K. Robbie, M. J. Brett, and A. Lakhtakia. First thin-film realization of a helicoidal bianisotropic medium. *J. Vac. Sci. Technol. A*, 13:2991, 1995.

[84] A. Lakhtakia and R. Messier. *Sculpured thin films: nanoengineered morphology and optics.* SPIE, Bellingham, 2005.

[85] C. Patzig, B. Rauschenbach, B. Fuhrmann, and H. S. Leipner. Growth of Si nanorods in honeycomb and hexagonal-closed-packed arrays using glancing angle deposition. *J. Appl. Phys.*, 103:024313, 2008.

[86] K. Nielsch, R. B. Wehrspohn, J. Barthel, J. Kirschner, U. Gösele, S. F. Fischer, and H. Kronmüller. Hexagonally ordered 100 nm period nickel nanowire arrays. *Appl. Phys. Lett.*, 79:1360, 2001.

[87] B. Alaca, H. Sehitoglu, and T. Saif. Guided self-assembly of metallic nanowires and channels. *Appl. Phys. Lett.*, 84:4669, 2004.

[88] K. Nielsch, R. Hertel, R. B. Wehrspohn, J. Barthel, J. Kirschner, U. Gösele, S.F. Fischer, and H. Kronmüller. Switching behavior of single nanowires inside dense nickel nanowire arrays. *IEEE Trans. Magn.*, 38:2571, 2002.

[89] S. Pignard, G. Goglio, A. Radulescu, L. Piraux, S. Dubois, A. Declemy, and J. L. Duvail. Study of the magnetization reversal in individual nickel nanowires. *J. Appl. Phys.*, 87:824, 2000.

[90] R. Hertel and J. Kirschner. Magnetization reversal dynamics in nickel nanowires. *Physica B*, 343:206, 2004.

[91] R. Ferré, K. Ounadjela, J. M. George, L. Piraux, and S. Dubois. Magnetization processes in nickel and cobalt electrodeposited nanowires. *Phys. Rev. B*, 56:14066, 1997.

[92] R. Hertel. Micromagnetic simulations of magnetostatically coupled nickel nanowires. *J. Appl. Phys.*, 90:5752, 2001.

[93] M. Vázquez, K. Pirota, M. Hernández-Vélez, V. M. Prida, D. Navas, R. Sanz, F. Batallán, and J. Velázquez. Magnetic properties of densely packed arrays of Ni nanowires as a function of their diameter and lattice parameter. *J. Appl. Phys.*, 95:6642, 2004.

[94] W. Wernsdorfer, B. Doudin, D. Mailly, K. Hasselbach, A. Benoit, J. Meier, J. Ph. Ansermet, and B. Barbara. Nucleation of magnetization reversal in individual nanosized nickel wires. *Phys. Rev. Lett.*, 77:1873, 1996.

[95] H. Masuda and K. Fukuda. Ordered metal nanohole arrays made by a two-step replication of honeycomb structures of anodic alumina. *Science*, 268:1466, 1995.

[96] W. Lee, R. Ji, K. Nielsch, and U. Gösele. Fast fabrication of long-range ordered porous alumina membranes by hard anodization. *Nat. Mater.*, 5:741, 2006.

[97] R. L. Puurunen. Surface chemistry of atomic layer deposition: A case study for the trimethylaluminum/water process. *J. Appl. Phys.*, 97:121301, 2005.

[98] M. Knez, K. Nielsch, and L. Niinistö. Synthesis and surface engineering of complex nanostructures by atomic layer deposition. *Adv. Mat.*, 19:3425, 2007.

[99] D. Li, R. S. Thompson, G. Bergmann, and J. G. Lu. Template-based synthesis and magnetic properties of cobalt nanotube arrays. *Adv. Mat.*, 20:4575, 2008.

[100] R. Sharif, S. Shamaila, M. Ma, L. D. Yao, R. C. Yu, X. F. Han, and M. Khaleeq-ur-Rahman. Magnetic switching of ferromagnetic nanotubes. *Appl. Phys. Lett.*, 92:032505, 2008.

[101] J. Bachmann, J. Jing, M. Knez, S. Barth, H. Shen, S. Mathur, U. Gösele, and K. Nielsch. Ordered iron oxide nanotube arrays of controlled geometry and tunable magnetism by atomic layer deposition. *J. Am. Chem. Soc.*, 129:9554, 2007.

[102] M. Daub, M. Knez, U. Gösele, and K. Nielsch. Ferromagnetic nanotubes by atomic layer deposition in anodic alumina membranes. *J. Appl. Phys.*, 101:09J111, 2007.

[103] K. Nielsch, F. J. Castano, C. A. Ross, and R. Krishnan. Magnetic properties of template-synthesized cobalt/polymer composite nanotubes. *J. Appl. Phys.*, 98:034318, 2005.

[104] J. Bachmann, J. Escrig, K. Pitzschel, J. M. Montero Moreno, J. Jing, D. Görlitz, D. Altbir, and K. Nielsch. Size effects in ordered arrays of magnetic nanotubes: Pick your reversal mode. *J. Appl. Phys.*, 105:07B521, 2009.

[105] S. Allende, J. Escrig, D. Altbir, E. Salcedo, and M. Bahiana. Angular dependence of the transverse and vortex modes in magnetic nanotubes. *Eur. Phys. J. B*, 66:37, 2008.

[106] E. Schubert, T. Höche, F. Frost, and B. Rauschenbach. Nanostructure fabrication by glancing angle ion beam assisted deposition of silicon. *Appl. Phys. A-Mater. Sci. Process.*, 81:481, 2005.

[107] C. Patzig, B. Rauschenbach, W. Erfurth, and A. Milenin. Ordered silicon nanostructures by ion beam induced glancing angle deposition. *J. Vac. Sci. Technol. B*, 25:1071, 2007.

[108] D. X. Ye, T. Karabacak, R. C. Picu, G. C. Wang, and T. M. Lu. Uniform Si nanostructures grown by oblique angle deposition with substrate swing rotation. *Nanotechnology*, 16:1717, 2005.

[109] C. Patzig, A. Miessler, T. Karabacak, and B. Rauschenbach. unpublished.

[110] C. Patzig, J. Zajadacz, R. Fechner, B. Fuhrmann, and B. Rauschenbach. unpublished.

[111] O. Albrecht, R. Zierold, C. Patzig, J. Bachmann, D. Görlitz, B. Rauschenbach, and K. Nielsch. Magnetic tubular nanostructures based on glancing angle deposited templates and atomic layer deposition. submitted, 2009.

[112] J. Bachmann, R. Zierold, Y. T. Chong, R. Hauert, C. Sturm, R. Schmidt-Grund, B. Rheinländer, M. Grundmann, U. Gösele, and K. Nielsch. A practical, self-catalytic, atomic layer deposition of silicon dioxid. *Angew. Chem.-Int. Edit.*, 47:6177, 2008.

[113] J. Escrig, D. Altbir, and K. Nielsch. Magnetic properties of bi-phase micro- and nanotubes. *Nanotechnology*, 18:225704, 2007.

[114] A. Aharoni. Angular dependence of nucleation by curling in a prolate spheroid. *J. Appl. Phys.*, 82:1281, 1997.

[115] C. Chang, C. M. Lee, and J. Yang. Magnetization curling reversal for an infinite hollow cylinder. *Phys. Rev. B*, 50:6461, 1994.

[116] Y. Ishii. Magnetization curling in an infinite cylinder with an uniaxial magnetocrystalline anisotropy. *J. Appl. Phys.*, 70:3765, 1991.

[117] R. C. O'Handley. *Modern magnetic Materials.* Wiley, 2000.

[118] S. Shamaila, D. P. Liu, R. Sharif, J. Y. Chen, H. R. Liu, and X. F. Han. Electrochemical fabrication and magnetization properties of CoCrPt nanowires and nanotubes. *Appl. Phys. Lett.*, 94:203101, 2009.

Appendix A

$\mathrm{Ni_xPt_{1-x}}$

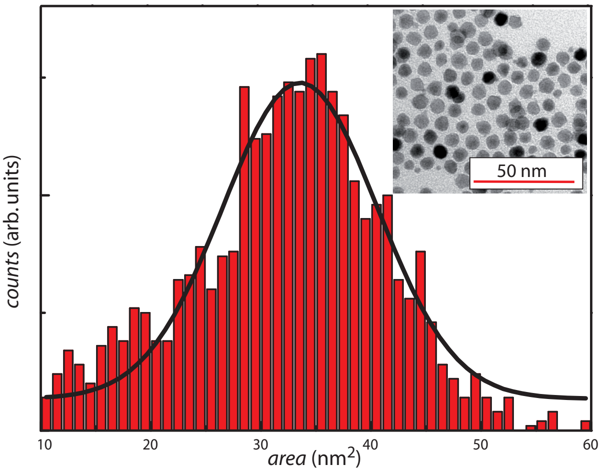

Figure A.1: Size distribution of the sample $\mathrm{Ni_{0.45}Pt_{0.55}}$ determined by image processing. Inset display exemplary TEM image.

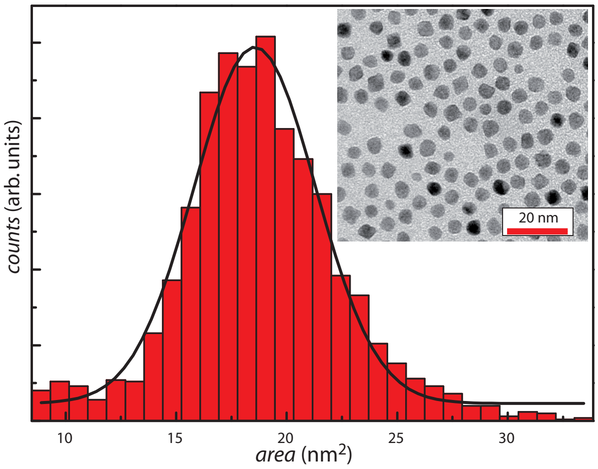

Figure A.2: Size distribution of the sample $Ni_{0.50}Pt_{0.50}$ determined by image processing. Inset display exemplary TEM image.

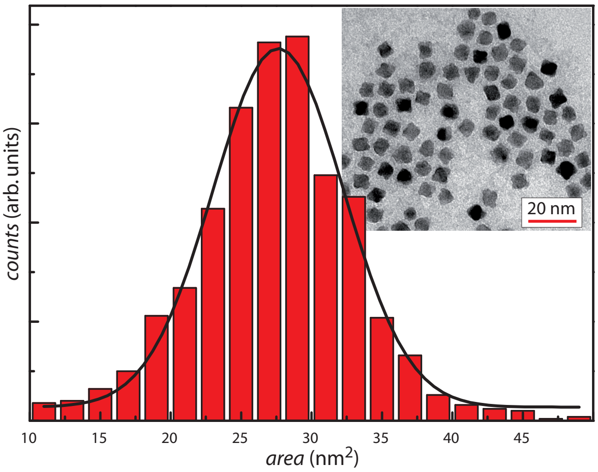

Figure A.3: Size distribution of the sample $Ni_{0.65}Pt_{0.35}$ determined by image processing. Inset display exemplary TEM image.

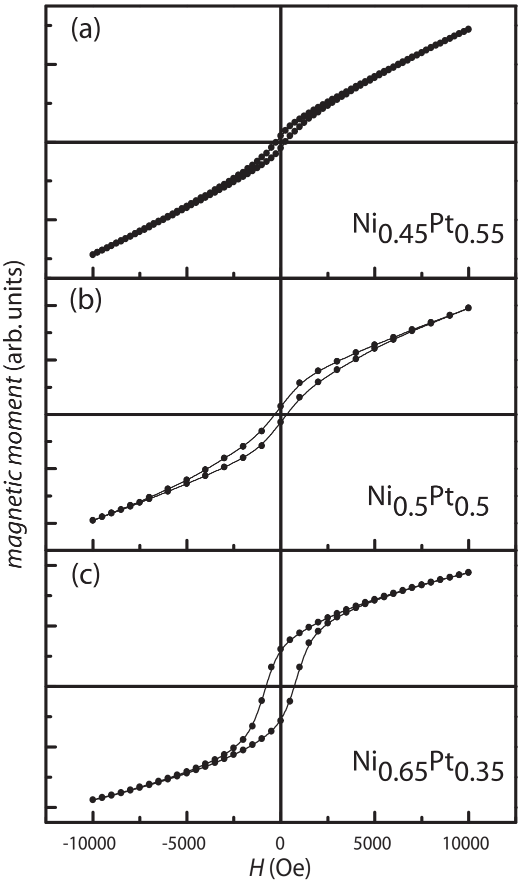

Figure A.4: Magnetization isotherms at 5 K of samples with varying NiPt ratio.

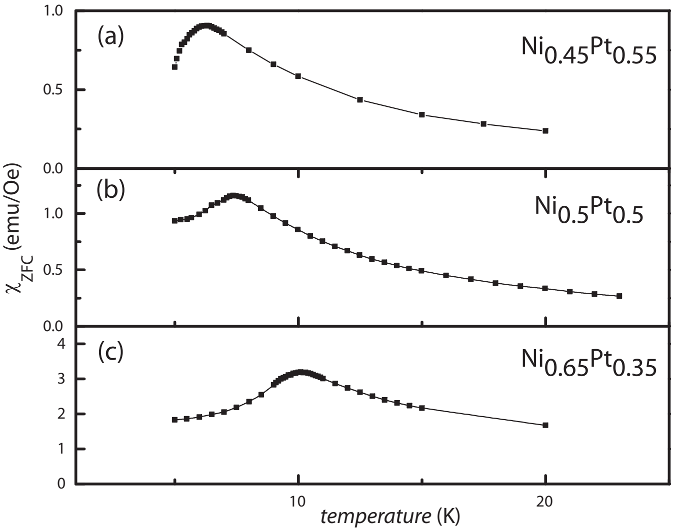

Figure A.5: Temperature dependent magnetization measurements in ZFC mode reveal the nickel ratio dependent blocking temperature T_b.

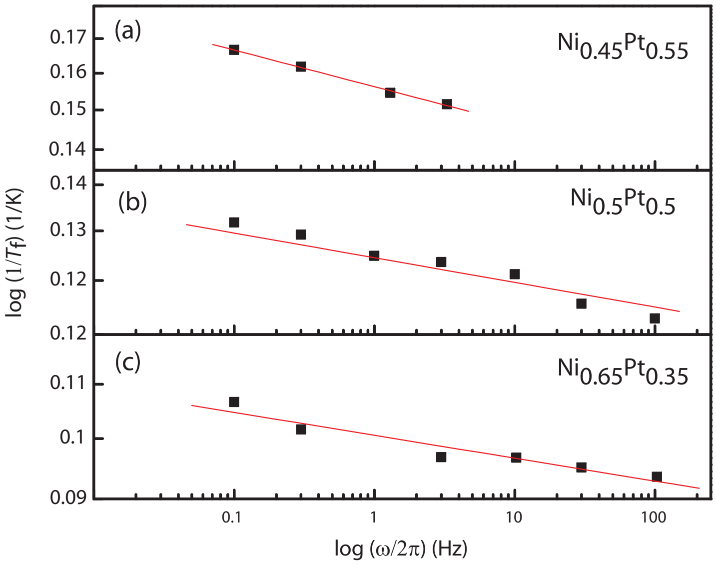

Figure A.6: Arrhenius plot: 1/T$_\mathrm{f}$f vs. frequency, the slope of the linear fit determines a mean energy-barrier.

Appendix B

Simulation OOMMF

OOMMF parameters	
Exchange stiffness A	13 pJ/m
Uniaxial anisotropy K_1	100 J/m^3
Cell size	5/5/15 nm
Damping factor α	0.5

Table B.1: Parameters for the micromagnetic simulation

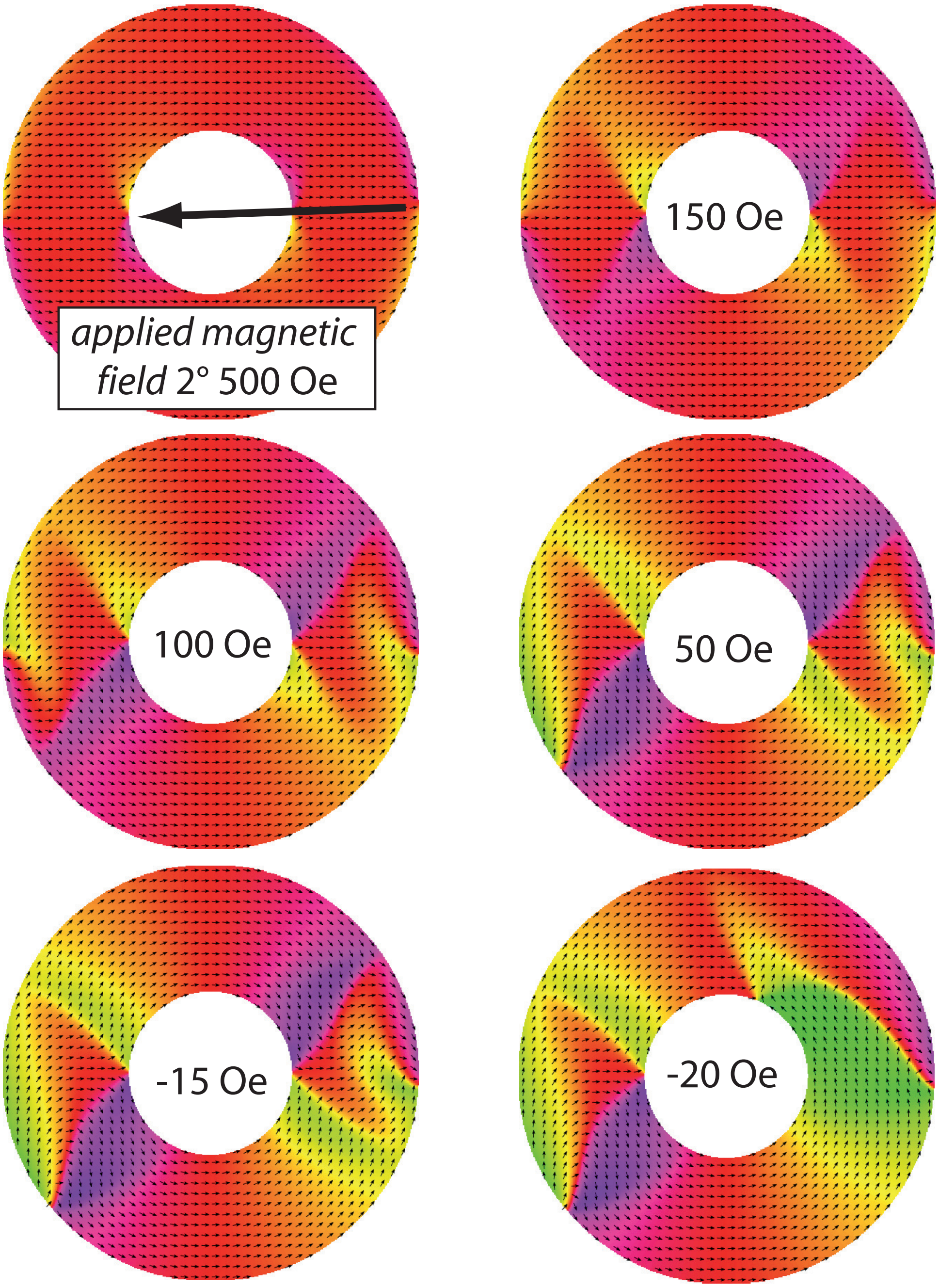

Figure B.1: Snapshots of the simulated spin configuration between +500 Oe and −20 Oe.

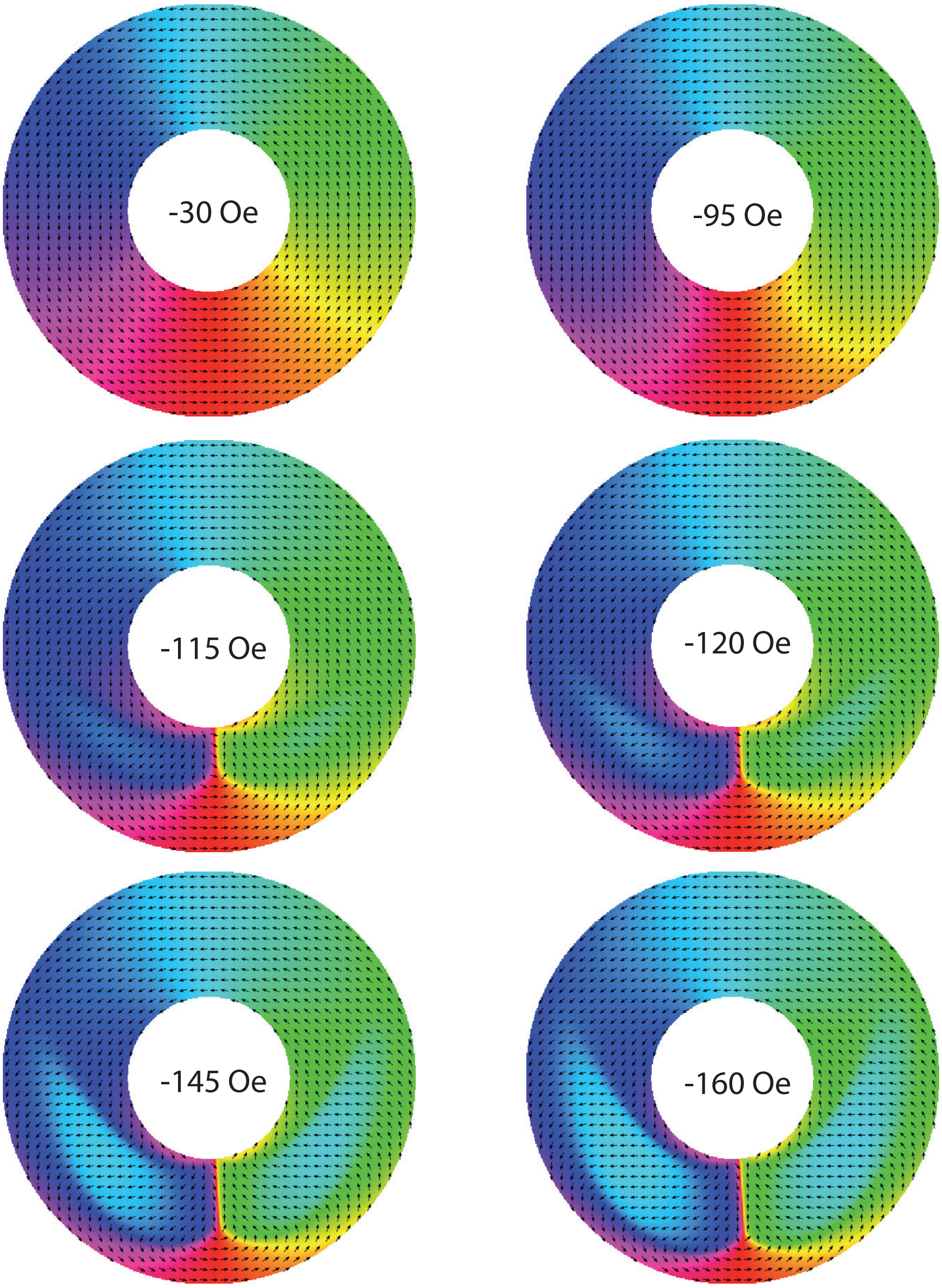

Figure B.2: Snapshots of the simulated spin configuration between −30 Oe and −160 Oe.

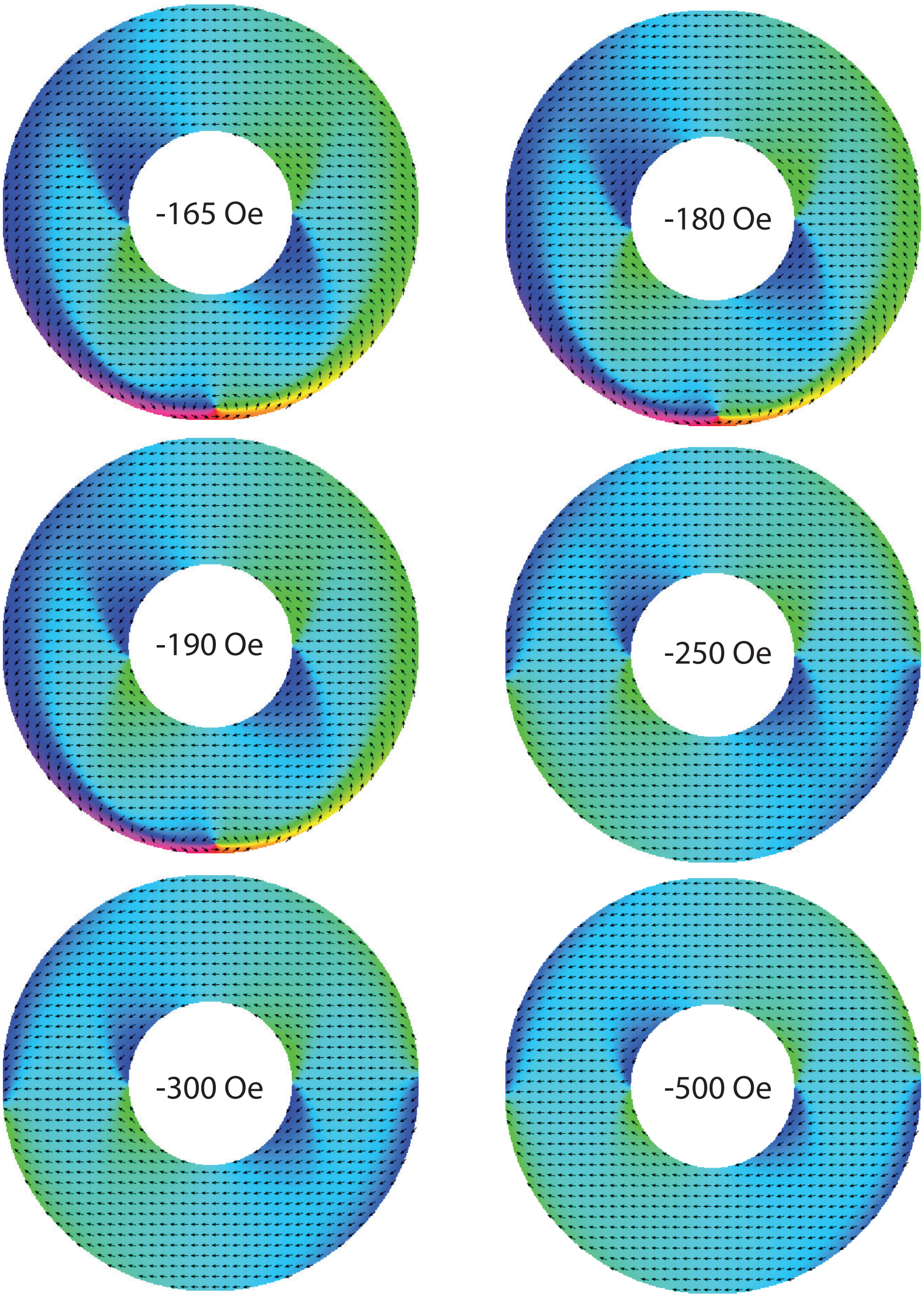

Figure B.3: Snapshots of the simulated spin configuration between −165 Oe and −500 Oe.

Appendix C

Magnetic nanotubes

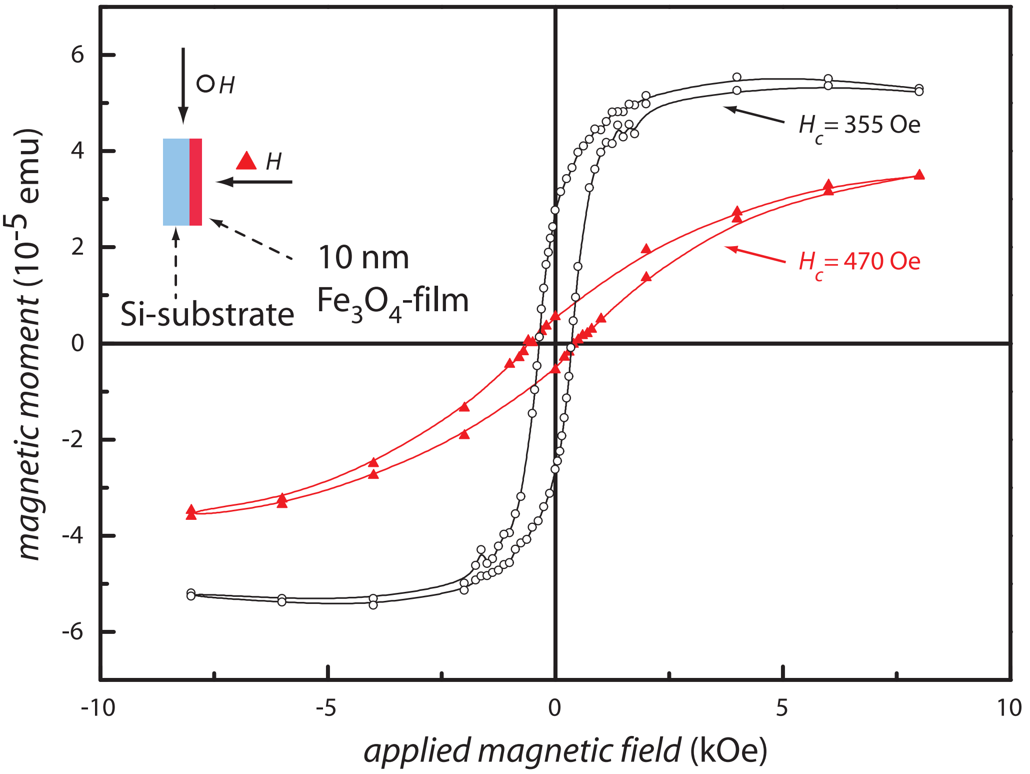

Figure C.1: Magnetization isotherms at room temperature for a 10 nm thick Fe_3O_4 film deposited on a Si substrate. The magnetic field was applied parallel or perpendicular to the substrate plane.

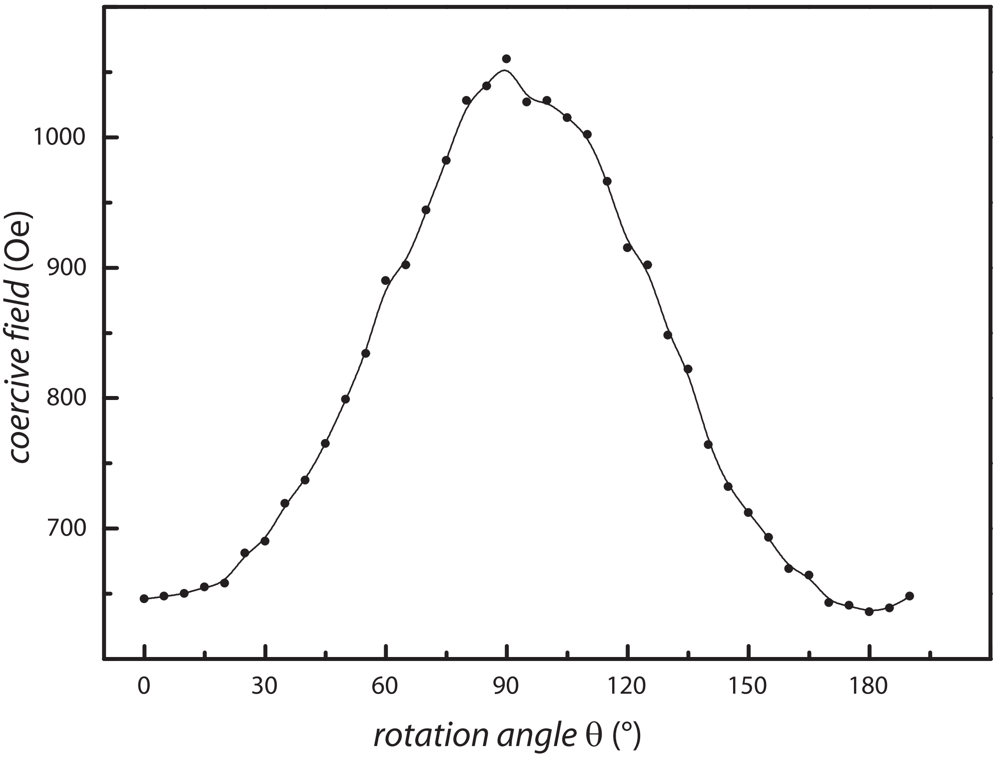

Figure C.2: Angular dependence of the coercive field of inclined columns ($\beta = 47° \pm 2°$) for a ($\vec{H} \| \vec{y} \rightarrow \vec{z} \rightarrow -\vec{y}$) rotation by the angle θ.

Appendix D

Process parameters

Double stack resist 50/950 K	
spinning-speed	6000 rpm
acceleration	255 (arb. units)
time	60 s
Oven-temp./time	160°, 1 h
Developer time	90 s
Stopper time	45 s

Table D.1: Process parameters for the double-stack e-beam resist.

SEM Leo Supra 55	
Acceleration voltage	10 kV
Extractor voltage	4.55 kV
Working distance	49.2 mm
Write field size	200 x 200 mm^2
Area dose	110 $\frac{\mu\mathrm{C}}{cm^2}$
Aperture size	20 μm
Beam current	90 pA

Table D.2: Process parameters for the e-beam lithography

Vacuum depositions chamber	
Thermal evaporation	$Ni_{80}Fe_{20}$
Base pressure Growth rate	$2 * 10^{-7}$ mbar 0.05 Å/s
E-beam evaporation	Au
Base pressure Growth rate	$2 * 10^{-7}$ mbar 0.1 Å/s

Table D.3: Process parameters for the thermal and e-beam evaporation

SiO_2-process				
Precursor	Temperature	Pulse time	Exposure time	Pumping time
3-aminopropyl-triethoxysilane	100 °C	2 s	20 s	20 s
water	50 °C	0.5 s	20 s	25 s
ozone-oxygen mixture	room temp.	0.2 s	20 s	20 s
Chamber temp. Flush gas			150 °C nitrogen 40 sccm	
Deposition rate			0.6 Å $cycle^{-1}$	

Table D.4: Parameter for the deposition of silicon dioxide.

Fe_2O_3-process				
Precursor	Temperature	Pulse time	Exposure time	Pumping time
ferrocene	100 °C	2 s	20 s	20 s
ozone-oxygen mixture	room temp.	0.2 s	20 s	20 s
Chamber temp. Flush gas			200 °C nitrogen 40 sccm	
Depositions rate			0.2 Å $cycle^{-1}$	

Table D.5: Parameter for the deposition of iron(III) oxide

Appendix E

Publications

[1] Colloidal synthesis of $\mathrm{Ni_xPt_{1-x}}$ nanoparticles with tuneable composition and size
K. Ahrenstorf, O. Albrecht, H. Heller, A. Kornowski , D. Görlitz, H. Weller
Small **2007**, *3*, 271.

[2] Microstructure and temperature-dependent magnetic properties of Co/Pt multilayered nanowires
LF. Liu, WY. Zhou, SS. Xie, O. Albrecht, K. Nielsch
Chem. Phys. Lett. **2008**, *466*, 165.

[3] Local modes and two magnon scattering in ordered permalloy antidot arrays
S. Martens, O. Albrecht,K. Nielsch, D. Görlitz
J. Appl. Phys. **2009**, *105*, 07C113-1.

[4] Influence of growth temperature on phase and intermixing in Ni2MnIn Heusler films on InAs(001)
A. Zolotaryov, A. Volland, C. Heyn, D. Novikov, G. Stryganyuk, A. Kornowski, T. Vossmeyer, O. Albrecht, E. Coric, W. Hansen
J. Cryst. Growth **2009**, *311*, 2397.

[5] Controlled introduction of diameter modulations in arrayed magnetic iron oxide nanotubes
K. Pitzschel, J. Montero Moreno, J. Escrig, O. Albrecht, K. Nielsch, J. Bachmann
ACS Nano **2009**, *3*, 3463.

[6] Stacked Nickelocenes: Synthesis, Structural Characterization and Magnetic Properties
S. Trtica, M. Prosenc, O. Albrecht, D. Görlitz, M. Schmidt, S. Puhl, E. Rentschler, F. Reuter, J. Heck
Inorg. Chem. **2010**, *49*, 1667.

[7] Magnetic Tubular Nanostructures Based on Glancing Angle Deposited Templates and Atomic Layer Deposition
O.Albrecht, R. Zierold, C. Patzig, J. Bachmann, C. Sturm, B. Rheinländer, M. Grundmann, D. Görlitz, B. Rauschenbach, K. Nielsch
Phys. Status Solidi B **2010**, *DOI 10.1002/pssb.200945560*

[8] A novel synthesis of ultrathin CoPt3 nanowires by dealloying larger diameter Co99Pt1 nanowires and subsequent stress-induced crack propagation
LF. Liu, O. Albrecht, E. Pippel, K. Nielsch, U. Gösele
Electrochem. Commun. **2010**, *accepted*

[9] Structural, Magnetic, and Transport Properties of Permalloy for Spintronic Experiments
G. Nahrwold, J. M. Scholtyssek, S. Motl-Ziegler, O. Albrecht, U. Merkt, G. Meier
J. Appl. Phys. **2010**, *accepted*

[10] Experimental Evidence for an Angular Dependent Transition of Magnetization Reversal Modes in Magnetic Nanotubes
O. Albrecht, R. Zierold, C. Patzig, S. Allende, D. Görlitz, B. Rauschenbach, K. Nielsch
submitted

Danksagung

An dieser Stelle möchte ich mich bei allen bedanken, die mich während meiner Doktorarbeit unterstützt haben. Mein Dank gilt:

- Prof. Dr. Kornelius Nielsch für die Aufnahme in die Arbeitsgruppe und die Übernahme beider Erstgutachten.
- Dr. Detlef Görlitz für die hervorragende Betreuung meiner Arbeit.
- Prof. Dr. Detlef Heitmann für die Übernahme des Zweitgutachtens der Dissertation und Priv. Doz. Dr. habil. Guido Meier für die Übernahme des Zweitgutachtens der Disputation.
- Robert Zierold, Dr. Julien Bachmann, Dr. Christian Patzig, Dr. Detlef Görlitz und Dr. Sebastian Allende für die erfolgreiche Zusammenarbeit an den Nanoröhrchen sowie Torben Menke, Dr. Kirsten Ahrenstorf und Jan Niehaus für die Synthese bzw. der optischen Spektroskopie der NiPt NiPt/CdSe Nanopartikel.
- Gesche Nahrwold, Dr. Andreas Volland, Dr. Lifeng Liu und Dr. Andriy Zolotaryov, Sabrina Trtica und Stephan Martens für die erfolgreiche Zusammenarbeit an Themen abseits meiner Dissertation.
- Dr. Jan Podbielski und Dr. René Eiselt für die Einführung in die Elektronenstrahl-Lithographie.
- Reinhold Meissner für kreative und schnelle Lösung von technischen Problemen.
- Stephan Martens für die mikromagnetischen Simulationen.
- Herrn Biedermann, stellvertretend für die E-Werkstatt und Herrn Hatje, stellvertretend für das Heliumverflüssigerteam.

- Meinen langjährigen Bürokollegen Stephan und Robert für die gute Zeit im Büro.
- René für den Kaffee am Nachmittag und für die vielen nicht-universitären Erkenntnisse.
- Tim, William, Sonja, Michael, Martin, Christian, Kristina, Josep, Robert und Stephan für die gute Zeit auch außerhalb des Büros.
- Den Arbeitsgruppen H, W, N und C für die gute Atmosphäre und Zusammenarbeit im Institut.

Ein großer Dank geht an alle Freunde, die mich während der vergangen Jahren begleitet haben und inbesondere für die spontanen ”Essen ist in 30 min. auf dem Tisch!” Mitteilungen sowie der Erkenntnis, dass sich Beharrlichkeit auszahlt.

Meiner Familie möchte ich dafür danken, dass sie mit Ihrer Unterstützung und Ihrem Vertrauen dies alles ermöglicht haben.